PHASE BEHAVIOR OF DIBLOCK COPOLYMER/HOMOPOLYMER BLENDS

Phase Behavior of Diblock Copolymer/Homopolymer Blends

By

Jiajia Zhou, M.Sc.

A Thesis

Submitted to the School of Graduate Studies

in Partial Fulfilment of the Requirements

for the Degree

Doctor of Philosophy

McMaster University

Doctor of Philosophy (2010)   McMaster University

(Department of Physics & Astronomy)   Hamilton, Ontario, Canada

TITLE: Phase Behavior of Diblock Copolymer/Homopolymer Blends

AUTHOR: Jiajia Zhou, M.Sc.

SUPERVISOR: Dr. An-Chang Shi

NUMBER OF PAGES: xiv, 120

Abstract

Self-consistent field theory (SCFT) is a well established theoretical framework for describing the thermodynamics of block copolymer melts and blends. Combined with numerical methods, the SCFT can give useful and accurate predictions regarding the phase behavior of polymer blends.

We have applied SCFT to study the phase behavior of blends composed of diblock copolymers (AB) and homopolymers (C). Two cases are studied in detail. In the first case the homopolymers have a repulsive interaction to the diblock copolymers. We found an interesting feature in the phase diagram that there exists a bump of the phase boundary line when A is the majority-component. In the second case, the homopolymers have an attractive interaction to one of the blocks of the diblock copolymers. A closed-loop of microphase separation region forms for strong interactions. For both cases, we have investigated the effects of homopolymer concentration, homopolymer chain length, and monomer-monomer interactions, on the phase behavior of the system.

We also investigated micelle formation in polymer blends. Diblock copolymers (AB) blended with homopolymers (A) can self-assemble into lamellar, cylindrical and spherical micelles. The critical micelle concentrations for different geometries are determined using self-consistent field theory. The effect of varying copolymer block asymmetry, homopolymer molecular weight and monomer-monomer interactions on micelle morphology are examined. When the blends are confined between two flat surfaces, the shape of the micelles may differ from that of the bulk micelles. We study the shape variation of a spherical micelle under confinement and its dependence on the film thickness and surface selectivity.

Acknowledgements

Like life, basketball is messy and unpredictable. It has its way with you, no matter how hard you try to control it. The trick is to experience each moment with a clear mind and open heart. When you do that, the game –and life– will take care of itself.

–Phil Jackson

It is hard to argue with someone as decorated as Phil Jackson, especially considering that he has to use the toe to wear all his NBA champion rings. I like this quote because not only it is quite wise, but also it can still make sense if you replace the basketball with diblock copolymer.

I have had the fortune/misfortune of taking a meandering path in my graduate study, depending on the point of view. Someone may think that it is quite a waste of time to spend eight years in graduate school. However, as any long-distant runners can testify, the finish time is hardly the most important criterion to evaluate a race; it is the journey, the experience that really matter. For me, I have really enjoyed the scenic route.

I wouldn't pass the final line (almost) without some amazing people who have helped and cheered for me on this long journey. I want to take this opportunity to thank them. Inevitably, I will miss some names, and for those people I apologize in advance.

I would like to thank my supervisor, Dr An-Chang Shi. You pointed me in the right direction when I was almost lost. Thanks for giving me the opportunity to explore the wonderful world of polymer physics (to be honest, I thought before only quantum mechanics is the *real* physics). Your patience, understanding and knowledge are greatly admired and appreciated. From you, I have learned (hopefully) how to do research and find interesting questions. The advices you gave me, both professional and personal, have helped me a lot. You've taught me so, *so* much –thank you.

Table of Contents

List of Figures

Chapter 1

Introduction

Polymers are chain-like macromolecules in which many small molecular units, called monomers, are linked together by covalent bonds. A macromolecule is called a homopolymer if all of its monomers are chemically identical. Examples of homopolymers are synthetic polymers like polystyrene, made of long chain of styrene. Copolymers, on the other hand, contain two or more chemically distinct monomers. Most biopolymers are copolymers: deoxyribonucleic acids (DNA) consist of long chain of four types of nucleotides, and proteins are made up of about twenty different amino-acids.

1.1 Diblock copolymers

Diblock copolymers are one special type of copolymers, in which the polymer chains are composed of two blocks of different monomers [1, 2]. Physicists and chemists are fascinated about diblock copolymers because, despite their simple chemical structure, they can self-assemble into a variety of ordered structures with the domain size in the order of nanometers. Different morphologies can be formed as a result of a competition between the interaction energy and the chain stretching. First of all, different blocks do not like mixing and tend to separate out into distinct parts. One the other hand, the chemical bonds linking different blocks prevent the separation at a macroscopic length. Therefore, diblock copolymers have to make some comprise between the separating and mixing, resulting in the formation of var-

ious ordered structures. For diblock copolymers, the simplest and most common morphologies are the so called classical structures: lamellae consisting of alternating layers (LAM), cylinders packed on a hexagonal lattice (HEX), and spheres arranged in a body-centered cubic lattice (BCC). There are also some complex structures: gyroid which is a bicontinuous phase with $Ia\bar{3}d$ symmetry [3, 4], perforated-lamellar phase [5], and a very recently discovered $Fddd$ phase which is a noncubic network morphology [6, 7, 8]. Schematic pictures of these morphologies are shown in Fig. 1.1.
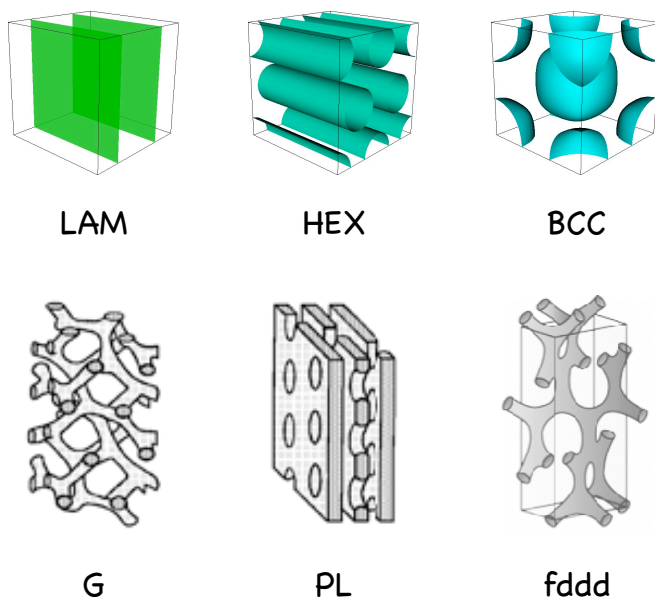
Figure 1.1: Ordered structure observed in diblock copolymer melts. Gyroid (G) and perforated-lamellar phase are adapted from ref. [9], and $Fddd$ phase is adapted from ref. [8].

Several properties of the diblock copolymer make it an ideal model system for the study of self-assembly. First of all, in the condensed melt, the polymer chains overlap each other and interact with many other chains. This ensures the validity of the mean-field approximation which can greatly simplify the model. Secondly, the high degree of polymerization allows one to model the polymers as flexible Gaussian

chains, whose energy is due to the stretching and has a simple form. Thirdly, the atomic details are suppressed by the macromolecular nature of the polymers, and the phase behavior of diblock copolymers is mainly controlled by two parameters: the block asymmetry f_A and the product of the total degree of polymerization N and the Flory-Huggins parameter χ. Various theoretical approaches have been developed to study the phase behavior of diblock copolymers. Among them, the self-consistent field theory proves to be one of the most successful. Fig. 1.2 compares the phase diagrams of diblock copolymers calculated from self-consistent field theory and from experiments [9]. Remarkably, the theory is able to predict all the stable morphologies and their relative positions in the phase diagram.

Edwards first introduced the idea of self-consistent field theory to polymer science. In his 1965 paper [10], he suggested that the probability distribution of a polymer chain may be approximated by that of a random walk in the external potential field, and the field can be determined *a posteriori* from the monomer density distribution. The theory was then applied to diblock copolymer melts by Helfand [11, 12]. Lately, several groups have made important contributions to the theory [13, 14, 15, 16]. Early attempts to calculate the phase diagram of diblock copolymers were restricted by limited computer resources, so approximation schemes were also developed to further simplify the theory. Among them, the most notable ones are Leibler's weak segregation theory [17] and Semenov's strong segregation theory [18]. Advances in the modern computers and numerical methods allow one to solve the self-consistent field theory without further approximation. The first complete phase diagram including all the known and proposed phases of diblock copolymers was calculated by Matsen and Schick [19] using a spectral method. Efficient algorithms to solve self-consistent field equations in real-space have also been developed [20, 21]. Combined with numerical methods, self-consistent field theory is capable of providing accurate predictions for
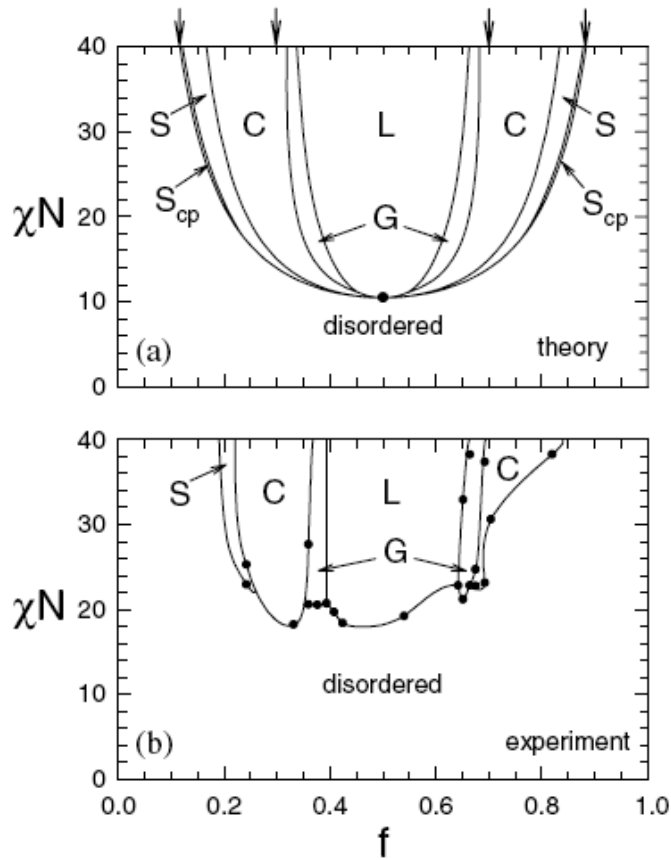
Figure 1.2: (a) Theoretical phase diagram calculated using the self-consistent field theory. (b) Experimental phase diagram measured using polystyrene-polyisoprene diblock copolymers. Adapted from ref. [9].

the phase behavior of polymeric systems. A number of monographs [1, 22] and review articles [9, 23, 24, 25] on self-consistent field theory are available in the literature. It can be concluded that self-consistent field theory provides a powerful theoretical framework to study block copolymers.

1.2 Diblock copolymer/homopolymer blends

Blending provides an effective and economical route to obtain new materials because the end products can have combinative and enhanced properties of their constituents. In general, different homopolymers do not mix due to the unfavorable thermodynamics. The entropy of mixing is often insignificant for long-chain homopolymers. Copolymers are ideal candidates to use as compatibilizers, which are utilized to increase the miscibility of polymers. From a theoretical point of view, the mix of homopolymers with diblock copolymers provides new behavior. Therefore a better understanding of the phase behavior of diblock copolymer/homopolymer blends is highly desirable.

There are two different angles we can take to approach this system. One is to treat the diblock copolymers as the majority component and we slowly add in homopolymers. The key question here is how the homopolymers distribute in the copolymer matrix. In general, the homopolymers can either separate from the diblock copolymers, or localize in domains of like blocks. In the former case, macrophase separation occurs, while in the latter situation, the blends may undergo order-order transitions.

Using the ordered structure formed by the diblock copolymer as a template, the homopolymers can be located in the regions where the copolymer chains are strongly stretched and thus relieve the packing frustration. In turn, new structures which are not found in diblock copolymer melts may be stabilized, among them are the double

diamond phase with a $Pn\bar{3}m$ symmetry [26] and the plumber's nightmare phase with an $Im3m$ symmetry [27].

From the other end of the spectrum, when a small amount of diblock copolymers are added into a homopolymer melt, local aggregates called micelles can be formed. Normally, one block of the copolymers is miscible to the homopolymers and the other one not. The local self-assembly is driven by this unbalance of miscibility. Specifically, the miscible blocks stay on the surface of the micelles, while the immiscible blocks are buried in the interior. The process of micelle formation is similar to the segregation of surfactants in water and the formation of bilayers from lipids. Depending on the copolymer configuration and interaction parameters, micelles with different shapes can be formed; they can be flat bilayer sheets, cylinders or spheres. A quantitative understanding of how the micelle shapes are determined by various factors is important from the fundamental polymer physics point of view.

Beside providing a paradigm to study self-assembly, block copolymer micelles can also be used for several applications. Various types of micelle shape can be used as templates for the fabrication of nano-structured materials. Also, diblock micelles are significantly more stable than the ones by surfactants of low-molecular weight. This offers opportunities to utilize spherical micelles for drug delivery.

Because of its success in diblock copolymer melts, self-consistent field theory is a natural choice to study the phase behavior of diblock copolymer/homopolymer blends.

1.3 Objective and outline

Using self-consistent field theory as the main tool, we address several problems related to the phase behavior of diblock copolymer/homopolymer blends in this thesis.

Chapter 2 reviews the theoretical framework of self-consistent field theory, using the AB/C blend as an example. The theory is developed in both canonical and grand canonical ensembles. Chapter 3 presents the numerical implementation of the theory. The central problem is how to solve a modified diffusion equation. Two methods, the spectral method and the finite difference method, are discussed in detail. The purpose of these two chapters is to lay the foundation for later applications.

In Chapter 4 and 5, we apply self-consistent field theory to study the phase behavior of AB/C blends. Chapter 4 considers blends of asymmetric copolymers. The addition of the homopolymer C provides further control of the phase diagram and enriches the phase behavior. We examine the effect of the homopolymer concentration, the homopolymer chain length, and the monomer-monomer interactions. In particular, an interesting feature of the phase diagram, a bump of the phase boundary line when A is the minority component, is discussed in term of competition between entropy and energy effects.

New phase behavior emerges when the interaction between the homopolymer C and one of the blocks becomes attractive. Inspired by recently experimental work of Chen *et al.* [28], we study the AB/C blends where all three binary pairs, A/B, B/C and C/A, are miscible. Despite the miscibility of the binary pairs, a closed-loop immiscible region exists when the A/C and B/C pair interactions are sufficiently different. Inside the closed-loop, the system undergoes microphase separation, exhibiting different ordered structures. In Chapter 5, we use both random phase approximation and self-consistent field theory to interrogate this interesting phenomenon.

We present the study of micellar structure of AB/A blends in Chapter 6 and 7. The subject of Chapter 6 is the micelle shape transition in bulk. Diblock copolymers added into homopolymer melts can self-assemble into lamellar, cylindrical and spherical micelles. The critical micelle concentrations for different geometries are de-

termined using self-consistent field theory. The effects of varying copolymer block asymmetry, homopolymer molecular weight and monomer-monomer interaction on micelle morphology are investigated.

In Chapter 7, we consider micelle formation under planar confinement. The shape of the micelles under confinement may differ from the bulk micelles due to the presence of two impenetrable surfaces. We use a real-space self-consistent field theory to examine the properties of an isolated micelle. We focus on the effect of film thickness and surface selectivity on the micelles. The results reveal that the spherical symmetry is broken by the film geometry, whereas the top-down symmetry is broken by the surface selectivity.

In Chapter 8 we summarize the key results of this thesis and give some perspective on future directions in this research area.

Chapter 2

Self-Consistent Field Theory

The system of interest consists of many polymer chains interacting with each other. In the framework of self-consistent field theory, this essentially many-body problem is replaced by the problem of an ideal Gaussian chain in an effective mean-field potential. This procedure is shown schematically in Fig. 2.1. If the mean-field potential can be specified, the thermodynamic properties of the system, such as the partition function and monomer densities, can be expressed in terms of the chain propagators, which are related to the mean field by the modified diffusion equations. From the monomer densities, a new mean-field potential can be constructed. The procedure results in a closed set of equations that can be solved self-consistently using numerical methods. Once the self-consistent solutions are reached, the free energy can be evaluated for various ordered structures. A phase diagram is constructed by finding the morphology with the lowest free energy.
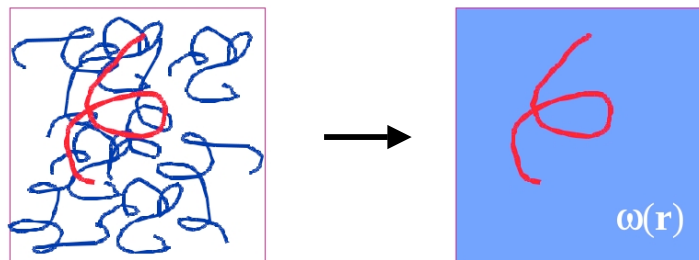
Figure 2.1: An illustration of the mean field approximation: an interacting many-chain system is approximated by a single chain in an averaged potential field $\omega_{\mathbf{r}}$.

In this chapter, we develop the self-consistent field theory for a binary blend of AB diblock copolymers and C homopolymers. We formulate the theory using a canonical ensemble approach first. Then the theory will be extended to the grand canonical ensemble.

2.1 Notations

In this section, we introduce the parameters and variables to describe the binary blends of diblock copolymer AB and homopolymer C. We will try to keep the notation consistent throughout this thesis.

The diblock copolymer AB and homopolymer C are labeled as polymer 1 and 2, respectively. In the canonical ensemble, the volume, the temperature and the numbers of polymer chains are the controlling thermodynamic parameters. We consider n_1 diblock copolymer and n_2 homopolymer chains in a volume V. Each polymer chain is composed of N_p monomers of species $\alpha = A, B$ for $p = 1$ or $\alpha = C$ for $p = 2$. The chain length of the diblock copolymer is $N_1 = \kappa_1 N$. We choose $N_1 = N$ to be the reference chain length, so $\kappa_1 = 1$. The homopolymer has a length of $N_2 = \kappa_2 N$. The ratio of the two polymer lengths is $\kappa = N_2/N_1 = \kappa_2$. For the diblock copolymer, the degrees of polymerization of the different blocks are $N_A = f_A N$ and $N_B = f_B N$ (where $f_A + f_B = 1$). For the homopolymer, we have $N_C = N_2 = \kappa N$.

Each type of monomer is associated with a statistical length $b_\alpha = \sigma_\alpha b$, where b is a reference length. The monomers are assumed to have the same monomer density ρ_0. The blend is incompressible, mimicking the hardcore monomer-monomer interaction, and the hardcore volume per monomer is ρ_0^{-1}. The volume fractions (or concentrations) for the copolymers and homopolymers are $1-\phi_H$ and ϕ_H, respectively. We will use the convention that all lengths are scaled by the radius of gyration for the

Diblock copolymer AB

$N_A = f_A N$ $N_B = f_B N$

$1 - \phi_H$

χ_{AB}

χ_{AC} χ_{BC}

Homopolymer C

ϕ_H

$N_C = \kappa N$

Parameter space: $(\kappa, f_A, \phi_H, \chi_{AB} N, \chi_{BC} N, \chi_{AC} N)$
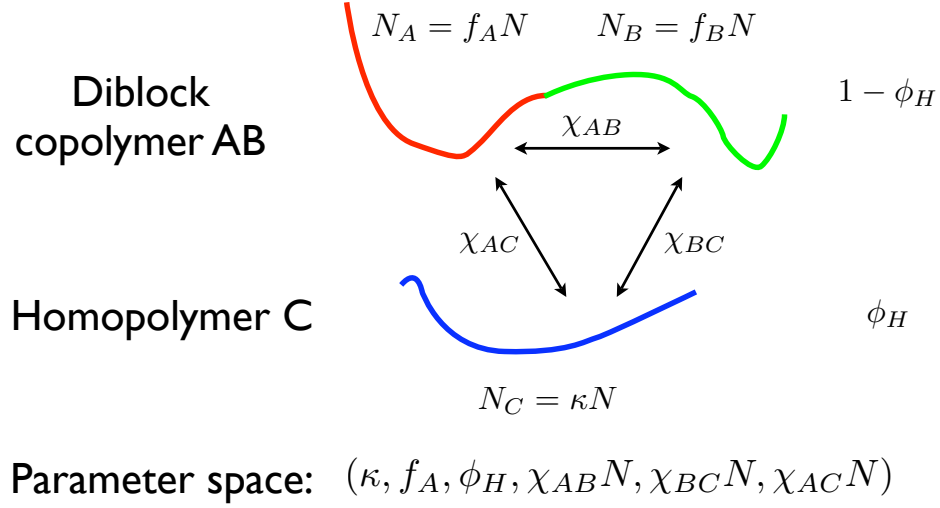
Figure 2.2: The parameters used to describe the diblock copolymer/homopolymer (AB/C) blends.

copolymer, $R_g = b\sqrt{N/6}$. The chain length is scaled by the copolymer chain length N. Finally, the interactions between each pair are characterized by the Flory-Huggins parameters: χ_{AB}, χ_{BC} and χ_{AC}. All relevant parameters are summarized in Fig. 2.2.

2.2 Partition function

Polymer chains with high degree of polymerization can be effectively treated as continuous, linearly elastic filaments without bending penalty. This is the so called continuous Gaussian chain model [29]. In this model, the conformation of an α-block of the i-th chain is denoted by a continuous-space curve $\mathbf{R}_i^\alpha(s)$, with s being the variable analog to the arc length, varying from 0 to N_α. For a given chain conformation $\{\mathbf{R}_i^\alpha(s)\}$, the local concentration of α-monomers at position $\mathbf{r}$ is,

$$\hat{\phi}_\alpha(\mathbf{r}) = \frac{1}{\rho_0} \sum_{i=1}^{n_p} \int_0^{N_\alpha} \mathrm{d}s \delta(\mathbf{r} - \mathbf{R}_i^\alpha(s)). \tag{2.1}$$

This is a set of delta functions located at the position of each chain segment. Evidently, this microscopic density function is a very singular function of the chain position. The hat on the variable $\hat{\phi}_\alpha$ emphasizes the dependence on the chain conformation.

The potential energy of a continuous Gaussian chain can be written as

$$U_0[\mathbf{R}_i^\alpha(s)] = \frac{3k_BT}{2b_\alpha^2} \int_0^{N_\alpha} \mathrm{d}s \left|\frac{\mathrm{d}\mathbf{R}_i^\alpha(s)}{\mathrm{d}s}\right|^2, \tag{2.2}$$

where $\mathrm{d}\mathbf{R}_i^\alpha(s)/\mathrm{d}s$ is the derivative of the curve $\mathbf{R}_i^\alpha(s)$ at contour position s. We use the square bracket notation $U_0[\mathbf{R}_i^\alpha(s)]$ to indicate that U_0 is a functional of $\mathbf{R}_i^\alpha(s)$. If we view the space curve as a flexible rubber band, $|\mathrm{d}\mathbf{R}_i^\alpha(s)/\mathrm{d}s|$ corresponds to the local stretching at the contour position s, then eqn (2.2) is a summation of a harmonic potential energy contribution from each segment $\mathrm{d}s$, with the spring constant being $3k_BT/2b_\alpha^2$. Potential energy of this form is commonly known as the *Edwards Hamiltonian*.

The probability distribution of observing $\mathbf{R}_i^\alpha(s)$ in the configuration space is the standard Boltzmann distribution

$$p_0[\mathbf{R}_i^\alpha(s)] = A \exp\left[-\frac{3}{2b_\alpha^2} \int_0^{N_\alpha} \mathrm{d}s \left(\frac{\mathrm{d}\mathbf{R}_i^\alpha(s)}{\mathrm{d}s}\right)^2\right], \tag{2.3}$$

where A is a normalization constant. The probability $P_0[\{\mathbf{R}_i(s)\}]$ for a given chain conformation $\{\mathbf{R}_i(s)\}$ is then given by

$$P_0[\{\mathbf{R}_i(s)\}] = \prod_{i=1}^{n_1} \left\{p_0(\mathbf{R}_i^A(s))p_0(\mathbf{R}_i^B(s))\delta[\mathbf{R}_i^A(N_A) - \mathbf{R}_i^B(N_B)]\right\} \prod_{i=1}^{n_2} \left\{p_0(\mathbf{R}_i^C(s))\right\}, \tag{2.4}$$

where the connection between the A- and B-block from the same chain is ensured by the delta functions.

The partition function of the blend can be written in terms of the functional integral over all the chain conformations,

$$Z = \frac{z_{01}^{n_1} z_{02}^{n_2}}{n_1! n_2!} \int \mathscr{D}\{\mathbf{R}_i(s)\} P_0[\{\mathbf{R}_i(s)\}] \prod_{\mathbf{r}} \delta(\sum_{\alpha} \hat{\phi}_{\alpha}(\mathbf{r}) - 1) e^{-W[\{\hat{\phi}(\mathbf{r})\}]}, \qquad (2.5)$$

where z_{0p} is the kinetic energy contribution to the partition functions, and $n_1! n_2!$ in the denominator counts for the fact that chains of the same type are indistinguishable. The delta-functions are introduced to enforce the incompressibility condition. The exponent term in the partition function is the Boltzmann factor associated with the monomer-monomer interaction potential $W[\{\hat{\phi}(\mathbf{r})\}]$, which is a functional of the microscopic densities $\{\hat{\phi}(\mathbf{r})\}$. We use the simple Flory-Huggins form of interaction energy

$$
\begin{aligned}
W[\{\hat{\phi}(\mathbf{r})\}] &= \rho_0 \int d\mathbf{r} \left[\chi_{AB}\hat{\phi}_A(\mathbf{r})\hat{\phi}_B(\mathbf{r}) + \chi_{BC}\hat{\phi}_B(\mathbf{r})\hat{\phi}_C(\mathbf{r}) + \chi_{AC}\hat{\phi}_A(\mathbf{r})\hat{\phi}_C(\mathbf{r}) \right] \\
&= \frac{1}{2} \sum_{\alpha \neq \beta} \rho_0 \chi_{\alpha\beta} \int d\mathbf{r} \hat{\phi}_{\alpha}(\mathbf{r})\hat{\phi}_{\beta}(\mathbf{r}).
\end{aligned}
\qquad (2.6)
$$

The partition function Z contains all the information about the thermodynamics of the AB/C system. However the evaluation of Z is not possible since the integrand depends on the chain conformation through the microscopic density functions $\{\hat{\phi}_{\alpha}\}$. A standard algebraic trick is to use the identity

$$1 = \int \mathscr{D}\{\phi_{\alpha}\} \prod_{\alpha} \prod_{\mathbf{r}} \delta(\phi_{\alpha}(\mathbf{r}) - \hat{\phi}_{\alpha}(\mathbf{r})), \qquad (2.7)$$

where $\phi_{\alpha}(\mathbf{r})$ is a dummy function for the functional integration and will later be identified as the average monomer density. Inserting this identity into expression (2.5), we have

$$
\begin{aligned}
Z &= \frac{z_{01}^{n_1} z_{02}^{n_2}}{n_1! n_2!} \int \mathscr{D}\{\phi_{\alpha}(\mathbf{r})\} \prod_{\mathbf{r}} \delta(\sum_{\alpha} \phi_{\alpha}(\mathbf{r}) - 1) e^{-W[\{\phi(\mathbf{r})\}]} \\
&\quad \times \int \mathscr{D}\{\mathbf{R}_i(s)\} P_0[\{\mathbf{R}_i(s)\}] \prod_{\alpha} \prod_{\mathbf{r}} \delta(\phi_{\alpha}(\mathbf{r}) - \hat{\phi}_{\alpha}(\mathbf{r})).
\end{aligned}
\qquad (2.8)
$$

Furthermore, auxiliary fields can be introduced by using the integral definition of the delta function:

$$1 = \int \mathscr{D}\{\phi_\alpha(\mathbf{r})\}\mathscr{D}\{\omega_\alpha(\mathbf{r})\} \exp\left[\sum_\alpha \rho_0 \int \mathrm{d}\mathbf{r}\omega_\alpha(\mathbf{r})(\phi_\alpha(\mathbf{r}) - \hat{\phi}_\alpha(\mathbf{r}))\right]. \qquad (2.9)$$

The range of the $\omega_\alpha(\mathbf{r})$ integral is along a line in the complex plane from $-i\infty$ to $i\infty$. The field $\omega_\alpha(\mathbf{r})$ can be viewed as a chemical potential field that is thermodynamically conjugate to the density field $\phi_\alpha(\mathbf{r})$ [30]. Substituting the identity (2.9) into the partition function expression (2.8), we have

$$
\begin{aligned}
Z &= \frac{z_{01}^{n_1} z_{02}^{n_2}}{n_1! n_2!} \int \mathscr{D}\{\phi_\alpha(\mathbf{r})\}\mathscr{D}\{\omega_\alpha(\mathbf{r})\} \prod_\mathbf{r} \delta(\sum_\alpha \phi_\alpha(\mathbf{r}) - 1) \\
&\quad \times \exp\left[\sum_\alpha \rho_0 \int \mathrm{d}\mathbf{r}\omega_\alpha(\mathbf{r})\phi_\alpha(\mathbf{r}) - W[\{\phi\}]\right] \\
&\quad \times \int \mathscr{D}\{\mathbf{R}_i(s)\}P_0[\{\mathbf{R}_i(s)\}] \exp\left[-\sum_\alpha \rho_0 \int \mathrm{d}\mathbf{r}\omega_\alpha(\mathbf{r})\hat{\phi}_\alpha(\mathbf{r})\right]. \qquad (2.10)
\end{aligned}
$$

The advantage of this form is that the integration over the chain conformation is done with the relatively simple integrand $\exp[-\sum_\alpha \rho_0 \int \mathrm{d}\mathbf{r}\omega_\alpha(\mathbf{r})\hat{\phi}_\alpha(\mathbf{r})]$. With the Gaussian probability distributions (2.3) and the definition of the microscopic density (2.1), the integral over the chain conformation can be written as,

$$
\begin{aligned}
&\int \mathscr{D}\{\mathbf{R}_i(s)\}P_0[\{\mathbf{R}_i(s)\}] \exp\left[-\sum_\alpha \rho_0 \int \mathrm{d}\mathbf{r}\omega_\alpha(\mathbf{r})\hat{\phi}_\alpha(\mathbf{r})\right] \\
&= \prod_{i=1}^{n_1}\left\{\int \mathscr{D}\{\mathbf{R}_i^A(s)\}\mathscr{D}\{\mathbf{R}_i^B(s)\}p_0[\mathbf{R}_i^A(s)]p_0[\mathbf{R}_i^B(s)]\right. \\
&\qquad \left.\times\delta[\mathbf{R}_i^A(N_A) - \mathbf{R}_i^B(N_B)] \exp\left[-\sum_{\alpha=A,B}\int_0^{N_\alpha}\mathrm{d}s\omega_\alpha(\mathbf{R}_i^\alpha(s))\right]\right\} \\
&\quad \times \prod_{i=1}^{n_2}\left\{\int \mathscr{D}\{\mathbf{R}_i^C(s)\}p_0[\mathbf{R}_i^C(s)] \exp\left[-\int_0^{N_C}\mathrm{d}s\omega_C(\mathbf{R}_i^\alpha(s))\right]\right\} \\
&= (Q_1 V)^{n_1}(Q_2 V)^{n_2}, \qquad (2.11)
\end{aligned}
$$

where Q_p is the partition function of a polymer chain of type p in the external field ω_α ($\alpha = A, B$ for $p = 1$ and $\alpha = C$ for $p = 2$). These single-chain partition functions are defined by

$$
\begin{aligned}
Q_1 &= \frac{1}{V} \int \mathscr{D}\{\mathbf{R}_i^A(s)\} \mathscr{D}\{\mathbf{R}_i^B(s)\} p_0[\mathbf{R}_i^A(s)] p_0[\mathbf{R}_i^B(s)] \\
&\times \delta[\mathbf{R}_i^A(N_A) - \mathbf{R}_i^B(N_B)] \exp\left[-\sum_{\alpha=A,B} \int_0^{N_\alpha} ds \omega_\alpha(\mathbf{R}_i^\alpha(s))\right] \quad (2.12) \\
Q_2 &= \frac{1}{V} \int \mathscr{D}\{\mathbf{R}_i^C(s)\} p_0[\mathbf{R}_i^C(s)] \exp\left[-\int_0^{N_C} ds \omega_C(\mathbf{R}_i^C(s))\right]. \quad (2.13)
\end{aligned}
$$

Furthermore, the incompressibility condition can be enforced using a Lagrange multiplier field $\eta(\mathbf{r})$,

$$
\delta(\sum_\alpha \phi_\alpha(\mathbf{r}) - 1) = \exp\left[-\rho_0 \int d\mathbf{r} \eta(\mathbf{r})(\sum_\alpha \phi_\alpha(\mathbf{r}) - 1)\right]. \quad (2.14)
$$

With the definition of the single-chain partition function Q_p and the field $\eta(\mathbf{r})$, the partition function of the AB/C blend can be rewritten as a functional integral over three fields: the density fields $\phi_\alpha(\mathbf{r})$, the chemical potential fields $\omega_\alpha(\mathbf{r})$, and the Lagrange multiplier field $\eta(\mathbf{r})$,

$$
\begin{aligned}
Z &= \int \mathscr{D}\{\phi_\alpha(\mathbf{r})\} \mathscr{D}\{\omega_\alpha(\mathbf{r})\} \mathscr{D}\{\eta(\mathbf{r})\} \prod_{\mathbf{r}} \exp\left[\sum_\alpha \rho_0 \int d\mathbf{r} \omega_\alpha(\mathbf{r}) \phi_\alpha(\mathbf{r}) - W[\{\phi\}]\right. \\
&\left. -\rho_0 \int d\mathbf{r} \eta(\mathbf{r})(\sum_\alpha \phi_\alpha(\mathbf{r}) - 1)\right] \frac{(z_{01} Q_1 V)^{n_1}}{n_1!} \frac{(z_{02} Q_2 V)^{n_2}}{n_2!}. \quad (2.15)
\end{aligned}
$$

The dependence of the chain conformation has been absorbed into the single-chain partition functions Q_p. This formulation of the partition function is the starting point of our theory.

2.3 Single-chain partition functions

The quantity $Q_p[\{\omega_\alpha\}]$ in the above expression is the partition function for a single chain subjected to the external field $\omega_\alpha(\mathbf{r})$. It is a functional of the field $\omega_\alpha(\mathbf{r})$, and

contains the chain conformation contribution to the total partition function Z. In the following, we discuss the partition function for the diblock copolymer AB and homopolymer C using the path integral formula [31].

The single-chain partition function Q_1 for AB diblock copolymer can be expressed in terms of the chain propagators $Q_\alpha(\mathbf{r}, s|\mathbf{r}')$,

$$Q_1 = \frac{1}{V} \int d\mathbf{r}_1 d\mathbf{r}_2 d\mathbf{r}_3 Q_A(\mathbf{r}_1, N_A|\mathbf{r}_2) Q_B(\mathbf{r}_2, N_B|\mathbf{r}_3), \tag{2.16}$$

where the chain propagators are defined by

$$Q_\alpha(\mathbf{r}, s|\mathbf{r}') = \int_{\mathbf{R}(0)=\mathbf{r}'}^{\mathbf{R}(s)=\mathbf{r}} \mathscr{D}\{\mathbf{R}(s)\} \exp\left[-\int_0^s ds' \left(\frac{3}{2b_\alpha^2} \left[\frac{d\mathbf{R}(s')}{ds'} \right]^2 + \omega_\alpha(\mathbf{R}(s')) \right) \right]. \tag{2.17}$$

The physical meaning of these propagators is that $Q_\alpha(\mathbf{r}, s|\mathbf{r}')$ represents the conditional probability of monomer s at position $\mathbf{r}$, given the monomer 0 is at position $\mathbf{r}'$, in the presence of an external field $\omega_\alpha(\mathbf{r})$.

From the definition (2.17), we can easily check the relation

$$Q_\alpha(\mathbf{r}, s|\mathbf{r}') = \int d\mathbf{r}'' Q_\alpha(\mathbf{r}, s - s''|\mathbf{r}'') Q_\alpha(\mathbf{r}'', s''|\mathbf{r}'). \tag{2.18}$$

This relation is based on the fact the propagator for a sub-chain $[0, s]$ is independent of the position of s''-monomer $(0 < s'' < s)$. Equation of the form (2.18) is referred to as a Chapman-Kolmogorov equation in the theory of stochastic process [32].

The integral form of the Chapman-Kolmogorov equation is difficult to use and sometimes a differential form is preferred. The corresponding differential equation is known as the Fokker-Planck equation in probability theory [32] and the Feynman-Kac formula in quantum mechanics [33]:

$$\frac{\partial}{\partial s} Q_\alpha(\mathbf{r}, s|\mathbf{r}') = \frac{b_\alpha^2}{6} \nabla^2 Q_\alpha(\mathbf{r}, s|\mathbf{r}') - \omega_\alpha(\mathbf{r}) Q_\alpha(\mathbf{r}, s|\mathbf{r}'). \tag{2.19}$$

The initial conditions is $Q_\alpha(\mathbf{r}, 0|\mathbf{r}') = \delta(\mathbf{r} - \mathbf{r}')$. This equation is commonly referred to as a modified diffusion equation in the polymer literature.

In later applications, it is convenient to use the end-integrated propagators, defined by integrating the end position $\mathbf{r}'$ of function $Q_\alpha(\mathbf{r}, s|\mathbf{r}')$

$$q_\alpha(\mathbf{r}, s) = \int d\mathbf{r}' Q_\alpha(\mathbf{r}, s|\mathbf{r}'), \tag{2.20}$$

$$q_\alpha^+(\mathbf{r}, s) = \int d\mathbf{r}' d\mathbf{r}'' Q_\alpha(\mathbf{r}, s|\mathbf{r}') Q_\beta(\mathbf{r}', N_\beta|\mathbf{r}''), \tag{2.21}$$

where $\beta = B$ if $\alpha = A$ and vice versa. These end-integrated propagators satisfy the same differential equation as $Q_\alpha(\mathbf{r}, s|\mathbf{r}')$, but with different initial conditions

$$q_\alpha(\mathbf{r}, 0) = 1, \tag{2.22}$$

$$q_\alpha^+(\mathbf{r}, 0) = \int d\mathbf{r}' Q_\beta(\mathbf{r}, N_\beta|\mathbf{r}') = q_\beta(\mathbf{r}, N_\beta). \tag{2.23}$$

Using the end-integrated propagators, the single-chain partition function Q_1 can be expressed as

$$Q_1 = \frac{1}{V} \int d\mathbf{r} q_A(\mathbf{r}, N_A) = \frac{1}{V} \int d\mathbf{r} q_B(\mathbf{r}, N_B). \tag{2.24}$$

The single-chain partition function Q_2 for C homopolymer can also be expressed in terms of the chain propagators $Q_C(\mathbf{r}, s|\mathbf{r}')$,

$$Q_2 = \frac{1}{V} \int d\mathbf{r}_1 d\mathbf{r}_2 Q_C(\mathbf{r}_1, N_C|\mathbf{r}_2) \tag{2.25}$$

where the definition of the chain propagator $Q_C(\mathbf{r}, s|\mathbf{r}')$ is the same as $Q_A(\mathbf{r}, s|\mathbf{r}')$ and $Q_B(\mathbf{r}, s|\mathbf{r}')$. It also satisfies the same modified diffusion equation (2.19) with the same initial condition.

The end-integrated propagator $q_C(\mathbf{r}, s)$ can also be defined as,

$$q_c(\mathbf{r}, s) = \int d\mathbf{r}' Q_C(\mathbf{r}, s|\mathbf{r}'). \tag{2.26}$$

Comparing to the diblock copolymer, one end-integrated propagator is sufficient for homopolymers.

The single-chain partition function for the homopolymer is written in terms of the propagator,

$$Q_2 = \frac{1}{V} \int \mathrm{d}\mathbf{r} q_C(\mathbf{r}, N_C). \tag{2.27}$$

2.4 Canonical ensemble theory

In canonical ensemble, the number of polymer chains is fixed. We can write the partition function in terms of an "effective Hamiltonian" [22, 34],

$$
\begin{aligned}
Z &= \int \mathscr{D}\{\phi_\alpha\}\mathscr{D}\{\omega_\alpha\} \prod_{\mathbf{r}} \delta(\sum_\alpha \phi_\alpha(\mathbf{r}) - 1) \exp\left[\sum_\alpha \rho_0 \int \mathrm{d}\mathbf{r}\omega_\alpha(\mathbf{r})\phi_\alpha(\mathbf{r}) - W[\{\phi_\alpha\}]\right] \\
&\quad \times \frac{(z_{01}Q_1 V)^{n_1}}{n_1!} \frac{(z_{02}Q_2 V)^{n_2}}{n_2!} \\
&= \int \mathscr{D}\{\phi_\alpha\}\mathscr{D}\{\omega_\alpha\} \prod_{\mathbf{r}} \delta(\sum_\alpha \phi_\alpha(\mathbf{r}) - 1) \exp\left[-H[\{\phi_\alpha\}, \{\omega_\alpha\}]\right], \tag{2.28}
\end{aligned}
$$

where the effective Hamiltonian is given by

$$
\begin{aligned}
H[\{\phi_\alpha\}, \{\omega_\alpha\}] &= W[\{\phi_\alpha\}] - \sum_\alpha \rho_0 \int \mathrm{d}\mathbf{r}\omega_\alpha(\mathbf{r})\phi_\alpha(\mathbf{r}) - \ln\frac{(z_{01}Q_1 V)^{n_1}}{n_1!} - \ln\frac{(z_{02}Q_2 V)^{n_2}}{n_2!} \\
&= \frac{1}{2}\sum_{\alpha\neq\beta}\rho_0\chi_{\alpha\beta}\int \mathrm{d}\mathbf{r}\phi_\alpha(\mathbf{r})\phi_\beta(\mathbf{r}) - \sum_\alpha \rho_0 \int \mathrm{d}\mathbf{r}\omega_\alpha(\mathbf{r})\phi_\alpha(\mathbf{r}) \\
&\quad - \sum_p n_p \ln\frac{z_{0p}eQ_p V}{n_p}, \tag{2.29}
\end{aligned}
$$

where the Stirling formula $n! \approx (n/e)^n$ is used.

We make some simple manipulations to the eqn (2.29). They are (i) using the average concentrations $\bar{\phi}_p = n_p N_p/\rho_0 V$, (ii) using the radius of gyration $R_g = b\sqrt{N/6}$ as the length scale, (iii) redefining the fields by including the factor N, $N\omega_\alpha(\mathbf{r}) \rightarrow \omega_\alpha(\mathbf{r})$. After these manipulations, we arrive at the result,

$$
\begin{aligned}
H[\{\phi_\alpha\}, \{\omega_\alpha\}] &= \frac{\rho_0 R_g^3}{N}\left\{\frac{1}{2}\sum_{\alpha\neq\beta}\chi_{\alpha\beta}N\int \mathrm{d}\mathbf{r}\phi_\alpha(\mathbf{r})\phi_\beta(\mathbf{r}) - \sum_\alpha \int \mathrm{d}\mathbf{r}\omega_\alpha(\mathbf{r})\phi_\alpha(\mathbf{r})\right. \\
&\quad \left. -V\sum_p \frac{\bar{\phi}_p}{\kappa_p}\ln\frac{z_{0p}eN_pQ_p}{\rho_0\bar{\phi}_p}\right\}. \tag{2.30}
\end{aligned}
$$

We can also write this in terms of an effective Hamiltonian density,

$$
\begin{aligned}
h[\{\phi_\alpha\}, \{\omega_\alpha\}] &\equiv \frac{NH[\{\phi_\alpha\}, \{\omega_\alpha\}]}{\rho_0 R_g^3 V} \\
&= \frac{1}{V} \int d\mathbf{r} \left\{ \frac{1}{2} \sum_{\alpha \neq \beta} \chi_{\alpha\beta} N \phi_\alpha(\mathbf{r}) \phi_\beta(\mathbf{r}) - \sum_\alpha \omega_\alpha(\mathbf{r}) \phi_\alpha(\mathbf{r}) \right\} \\
&\quad - \sum_p \frac{\bar\phi_p}{\kappa_p} \ln Q_p + \sum_p \frac{\bar\phi_p}{\kappa_p} \ln(\frac{\bar\phi_p}{e}) + \sum_p \mu_{0p} \bar\phi_p,
\end{aligned}
\tag{2.31}
$$

where $\mu_{0p} \equiv (N/N_p) \ln(\rho_0/z_{0p}N_p)$ are constants which can be neglected.

Following the same procedure, the modified diffusion equation for the propagators can be rewritten in the form,

$$
\frac{\partial}{\partial s} q_\alpha(\mathbf{r}, s) = \sigma_\alpha^2 \nabla^2 q_\alpha(\mathbf{r}, s) - \omega_\alpha(\mathbf{r}) q_\alpha(\mathbf{r}, s).
\tag{2.32}
$$

The equations for $q_\alpha^+(\mathbf{r}, s)$ $(\alpha = A, B)$ and $q_C(\mathbf{r}, s)$ have the same form. The initial conditions are

$$
\begin{aligned}
q_\alpha(\mathbf{r}, 0) &= 1, &(2.33)\\
q_\alpha^+(\mathbf{r}, 0) &= q_\beta(\mathbf{r}, f_\beta), &(2.34)\\
q_C(\mathbf{r}, 0) &= 1. &(2.35)
\end{aligned}
$$

In terms of the propagators, the single-chain partition functions are given by

$$
\begin{aligned}
Q_1 &= \frac{1}{V} \int d\mathbf{r} q_A^+(\mathbf{r}, f_A) = \frac{1}{V} \int d\mathbf{r} q_B^+(\mathbf{r}, f_B), &(2.36)\\
Q_2 &= \frac{1}{V} \int d\mathbf{r} q_C(\mathbf{r}, \kappa_2). &(2.37)
\end{aligned}
$$

The partition function of the system is then written in the form,

$$
Z = \int \mathscr{D}\{\phi_\alpha\} \mathscr{D}\{\omega_\alpha\} \mathscr{D}\{\eta\} \exp\left[-\Omega[\{\phi_\alpha\}, \{\omega_\alpha\}, \{\eta\}] \right],
\tag{2.38}
$$

$$
\Omega[\{\phi_\alpha\}, \{\omega_\alpha\}, \{\eta\}] = H[\{\phi_\alpha\}, \{\omega_\alpha\}] + \rho_0 R_g^3 \int d\mathbf{r} \eta(\mathbf{r}) (\sum_\alpha \phi_\alpha(\mathbf{r}) - 1).
\tag{2.39}
$$

At this point, no approximation has been made except the minor one of Stirling's formula. The thermodynamic properties of a blend AB/C is completely determined if we can evaluate the functional integral (2.38). Unfortunately, except for some very special cases, the integral cannot be carried out exactly. Therefore, we need approximate methods to proceed. The most fruitful method is the mean field approximation, which amounts to replacing the functional integral (2.38) by the value of the integrand at its saddle point. Therefore, this approximation is also referred as saddle-point approximation or steepest descent method. Technically the approximation is obtained by demanding that the functional derivatives of $\Omega[\{\phi_\alpha\}, \{\omega_\alpha\}, \{\eta\}]$ with respect to the fields are zero,

$$\frac{\delta\Omega[\{\phi_\alpha\}, \{\omega_\alpha\}, \{\eta\}]}{\delta\omega_\alpha(\mathbf{r})} = 0, \tag{2.40}$$

$$\frac{\delta\Omega[\{\phi_\alpha\}, \{\omega_\alpha\}, \{\eta\}]}{\delta\phi_\alpha(\mathbf{r})} = 0, \tag{2.41}$$

$$\frac{\delta\Omega[\{\phi_\alpha\}, \{\omega_\alpha\}, \{\eta\}]}{\delta\eta(\mathbf{r})} = 0, \tag{2.42}$$

which leads to the following mean-field equations,

$$\phi_\alpha(\mathbf{r}) = \langle\hat{\phi}_\alpha(\mathbf{r})\rangle \tag{2.43}$$

$$\omega_\alpha(\mathbf{r}) = \sum_{\beta\neq\alpha}\chi_{\alpha\beta}N[\phi_\beta(\mathbf{r}) - \bar{\phi}_\beta(\mathbf{r})] + \eta(\mathbf{r}), \tag{2.44}$$

$$\sum_{\alpha=A,B,C}\phi_\alpha(\mathbf{r}) = 1. \tag{2.45}$$

Eqn (2.43) confirms that $\phi_\alpha(\mathbf{r})$ is equal to $\langle\hat{\phi}_\alpha(\mathbf{r})\rangle$, the thermal average of the microscopic density in a system of non-interacting chains subjected to the external fields $\omega_\alpha(\mathbf{r})$. The dependence on the external fields are through the propagators

$$\phi_\alpha(\mathbf{r}) = \frac{\bar{\phi}_1}{Q_1}\int_0^{f_\alpha} \mathrm{d}s q_\alpha(\mathbf{r}, s) q_\alpha^+(\mathbf{r}, f_\alpha - s) \quad \alpha = A, B, \tag{2.46}$$

$$\phi_C(\mathbf{r}) = \frac{\bar{\phi}_2}{\kappa_2 Q_2}\int_0^{\kappa_2} \mathrm{d}s q_C(\mathbf{r}, s) q_C(\mathbf{r}, \kappa_2 - s). \tag{2.47}$$

Eqn (2.44) relates the mean-field potential to the average monomer density. We also add some constants to the fields to make $\int \mathrm{d}\mathbf{r}\omega_\alpha(\mathbf{r}) = 0$. Those constants are

$$\bar{\phi}_A = \bar{\phi}_1 f_A, \quad \bar{\phi}_B = \bar{\phi}_1 f_B, \quad \bar{\phi}_C = \bar{\phi}_2. \tag{2.48}$$

Eqn (2.45) is simply the incompressible condition.

Within the mean-field approximation, the Helmholtz free energy density is obtained by inserting the mean field solution into expression (2.31),

$$
\begin{aligned}
f_{\mathrm{MF}} &= \frac{1}{V}\int \mathrm{d}\mathbf{r}\left\{\frac{1}{2}\sum_{\alpha\neq\beta}\chi_{\alpha\beta}N\phi_\alpha(\mathbf{r})\phi_\beta(\mathbf{r}) - \sum_\alpha \omega_\alpha(\mathbf{r})\phi_\alpha(\mathbf{r})\right\} \\
&\quad -\sum_p \frac{\bar{\phi}_p}{\kappa_p}\ln Q_p + \sum_p \frac{\bar{\phi}_p}{\kappa_p}\ln(\frac{\bar{\phi}_p}{e}) + \sum_p \mu_{0p}\bar{\phi}_p.
\end{aligned}
\tag{2.49}
$$

2.4.1 Homogeneous Phase

The simplest solution of the mean-field equations is obtained for a homogeneous phase, in which the monomer densities and the mean-field potentials are constant, $\phi_\alpha(\mathbf{r}) = \bar{\phi}_\alpha$ and $\omega_\alpha(\mathbf{r}) = 0$, leading to the trivial solution $q_\alpha(\mathbf{r},s) = q_\alpha^+(\mathbf{r},s) = 1$. The free energy density of a homogeneous phase is therefore given by

$$f_H = \chi_{AB}Nf_Af_B\phi_1^2 + (\chi_{AC}Nf_A + \chi_{BC}Nf_B)\phi_1\phi_2 + \frac{\phi_1}{\kappa_1}\ln\frac{\phi_1}{e} + \frac{\phi_2}{\kappa_2}\ln\frac{\phi_2}{e} + \mu_{01}\phi_1 + \mu_{02}\phi_2. \tag{2.50}$$

It is noticed that this free energy has the standard Flory-Huggins form [35].

2.5 Grand canonical ensemble theory

In the grand canonical ensemble, the numbers of polymer chains vary to maintain chemical equilibrium. The controlling parameters are the chemical potentials μ_1 and μ_2. The grand partition function is defined by,

$$
\begin{aligned}
\varsigma &= \sum_{n_1=0}^{\infty} \sum_{n_2=0}^{\infty} e^{n_1\mu_1 + n_2\mu_2} Z_{n_1,n_2} \\
&= \int \mathscr{D}\{\phi_\alpha\}\mathscr{D}\{\omega_\alpha\} \prod_{\mathbf{r}} \delta(\sum_\alpha \phi_\alpha(\mathbf{r}) - 1) \exp\left[\sum_\alpha \frac{\rho_0}{N} \int d\mathbf{r}\,\omega_\alpha(\mathbf{r})\phi_\alpha(\mathbf{r}) - W[\{\phi_\alpha\}]\right] \\
&\quad \times \sum_{n_1=0}^{\infty} \frac{(z_{01}Q_1 V)^{n_1}}{n_1!} \sum_{n_2=0}^{\infty} \frac{(z_{02}Q_2 V)^{n_2}}{n_2!} \\
&= \int \mathscr{D}\{\phi_\alpha\}\mathscr{D}\{\omega_\alpha\} \prod_{\mathbf{r}} \delta(\sum_\alpha \phi_\alpha(\mathbf{r}) - 1) \exp\left[-H_G[\{\phi_\alpha\},\{\omega_\alpha\}]\right],
\end{aligned}
\tag{2.51}
$$

where H_G is given by,

$$
\begin{aligned}
H_G[\{\phi_\alpha\},\{\omega_\alpha\}] &= \frac{1}{2}\sum_{\alpha\neq\beta} \rho_0 \chi_{\alpha\beta} \int d\mathbf{r}\,\phi_\alpha(\mathbf{r})\phi_\beta(\mathbf{r}) - \sum_\alpha \frac{\rho_0}{N}\int d\mathbf{r}\,\omega_\alpha(\mathbf{r})\phi_\alpha(\mathbf{r}) \\
&\quad - e^{\mu_1} z_{01} Q_1 V - e^{\mu_2} z_{02} Q_2 V.
\end{aligned}
\tag{2.52}
$$

The corresponding energy density is

$$
\begin{aligned}
h_G[\{\phi\},\{\omega\}] &\equiv \frac{N}{\rho R_g^3 V} H_G(\{\phi\},\{\omega\}) \\
&= \frac{1}{V}\int d\mathbf{r}\left\{\frac{1}{2}\sum_{\alpha\neq\beta} \chi_{\alpha\beta} N \phi_\alpha(\mathbf{r})\phi_\beta(\mathbf{r}) - \sum_\alpha \omega_\alpha(\mathbf{r})\phi_\alpha(\mathbf{r})\right\} \\
&\quad - e^{\mu_1 - \mu_{01}} Q_1 - e^{\mu_2 - \kappa_2\mu_{02}} \frac{Q_2}{\kappa_2},
\end{aligned}
\tag{2.53}
$$

where $\mu_{0p} \equiv (1/\kappa_p)\ln(\rho_0/z_{0p}N_p)$ are constants defined before for the canonical ensemble.

The partition function of the system is then written in the form,

$$
\varsigma = \int \mathscr{D}\{\phi_\alpha\}\mathscr{D}\{\omega_\alpha\}\mathscr{D}\{\eta\} \exp\left[-\Omega[\{\phi_\alpha\},\{\omega_\alpha\},\{\eta\}]\right],
\tag{2.54}
$$

$$
\Omega[\{\phi_\alpha\},\{\omega_\alpha\},\{\eta\}] = H_G[\{\phi_\alpha\},\{\omega_\alpha\}] + \rho_0 R_g^3 \int d\mathbf{r}\,\eta(\mathbf{r})(\sum_\alpha \phi_\alpha(\mathbf{r}) - 1).
\tag{2.55}
$$

The mean-field equations are again derived by demanding the functional deriva-tives of Ω to vanish, which leads to the following mean-field equations,

$$\phi_\alpha(\mathbf{r}) = e^{\Delta\tilde{\mu}_1} \int_0^{f_\alpha} \mathrm{d}s q_\alpha(\mathbf{r}, s) q_\alpha^+(\mathbf{r}, f_\alpha - s) \quad \alpha = A, B, \tag{2.56}$$

$$\phi_C(\mathbf{r}) = \frac{e^{\kappa_2 \Delta\tilde{\mu}_2}}{\kappa_2} \int_0^{\kappa_2} \mathrm{d}s q_C(\mathbf{r}, s) q_C^+(\mathbf{r}, \kappa_2 - s), \tag{2.57}$$

$$\omega_\alpha(\mathbf{r}) = \sum_{\beta \neq \alpha} \chi_{\alpha\beta} N \phi_\beta(\mathbf{r}) + \eta(\mathbf{r}), \tag{2.58}$$

$$\sum_{\alpha=A,B,C} \phi_\alpha(\mathbf{r}) = 1. \tag{2.59}$$

The control parameter $\Delta\tilde{\mu}_p = \tilde{\mu}_p - \mu_{0p} = \mu_p/\kappa_p - \mu_{0p}$, is the effective chemical potential per monomer.

Once solutions of the mean-field equations are obtained, the Gibbs free energy density can be computed using the expression,

$$g_{\mathrm{MF}} = \frac{1}{V} \int \mathrm{d}\mathbf{r} \left\{ \frac{1}{2} \sum_{\alpha \neq \beta} \chi_{\alpha\beta} N \phi_\alpha(\mathbf{r}) \phi_\beta(\mathbf{r}) - \sum_\alpha \omega_\alpha(\mathbf{r}) \phi_\alpha(\mathbf{r}) \right\} - e^{\Delta\tilde{\mu}_1} Q_1 - e^{\kappa_2 \Delta\tilde{\mu}_2} \frac{Q_2}{\kappa_2}. \tag{2.60}$$

2.5.1 Homogeneous Phase

For a disordered phase all the concentrations and fields are constants. The prop-agators are easily to obtain in this case,

$$Q_\alpha(\mathbf{r}, s|\mathbf{r}') = e^{-\bar{\omega}_\alpha s} \delta(\mathbf{r} - \mathbf{r}'), \tag{2.61}$$

$$q_\alpha(\mathbf{r}, s) = e^{-\bar{\omega}_\alpha s}, \quad \alpha = A, B, C, \tag{2.62}$$

$$q_\alpha^+(\mathbf{r}, s) = e^{-\bar{\omega}_\alpha s - \bar{\omega}_\beta f_\beta}, \quad \alpha, \beta = A, B, \tag{2.63}$$

$$Q_1 = e^{-\bar{\omega}_A f_A - \bar{\omega}_B f_B}, \tag{2.64}$$

$$Q_2 = e^{-\bar{\omega}_C \kappa_2}. \tag{2.65}$$

Therefore the mean-field equations become,

$$\bar{\phi}_A = e^{\Delta\tilde{\mu}_1} Q_1 f_A = \bar{\phi}_1 f_A, \tag{2.66}$$

$$\bar{\phi}_B = e^{\Delta\tilde{\mu}_1}Q_1 f_B = \bar{\phi}_1 f_B, \tag{2.67}$$

$$\bar{\phi}_C = e^{\kappa_2\Delta\tilde{\mu}_2}Q_2 = \bar{\phi}_2, \tag{2.68}$$

$$\bar{\phi}_1 = e^{\Delta\tilde{\mu}_1 - \bar{\omega}_A f_A - \bar{\omega}_B f_B}, \tag{2.69}$$

$$\bar{\phi}_2 = e^{\kappa_2(\Delta\tilde{\mu}_2 - \bar{\omega}_C)}, \tag{2.70}$$

$$\bar{\omega}_\alpha = \sum_{\beta\neq\alpha}\chi_{\alpha\beta}N\bar{\phi}_\beta + \bar{\eta}, \tag{2.71}$$

$$\sum_\alpha \bar{\phi}_\alpha = \sum_p \bar{\phi}_p = 1. \tag{2.72}$$

The Gibbs free energy density is,

$$g_H = \frac{1}{2}\sum_{\alpha\neq\beta}\chi_{\alpha\beta}N\bar{\phi}_\alpha\bar{\phi}_\beta - \sum_\alpha\bar{\omega}_\alpha\bar{\phi}_\alpha - e^{\Delta\tilde{\mu}_1}Q_1 - e^{\kappa_2\Delta\tilde{\mu}_2}\frac{Q_2}{\kappa_2}. \tag{2.73}$$

2.5.2 Activity

It is useful to note that the densities $\phi_\alpha(\mathbf{r})$ and the free energy are invariant under the transformation,

$$\Delta\tilde{\mu}_p \to \Delta\tilde{\mu}_p + \mu_0 \qquad \omega_\alpha = \omega_\alpha + \mu_0. \tag{2.74}$$

This is easy to understand because it is the energy difference matters rather than the absolute value of the energy. The partition function changes as $Q_p \to e^{-\kappa_p\mu_0}Q_p$, but the combination $e^{\kappa_p\Delta\tilde{\mu}_p}Q_p$ is invariant under the transformation (2.74).

Using this property, we can choose $\mu_0 = -\Delta\tilde{\mu}_1$ to set the factor $e^{\Delta\tilde{\mu}_1}$ to 1. The mean-field equations become,

$$\phi_A(\mathbf{r}) = \int_0^{f_A} ds\, q_A(\mathbf{r}, s)q_A^+(\mathbf{r}, f_A - s) \tag{2.75}$$

$$\phi_B(\mathbf{r}) = \int_0^{f_B} ds\, q_B(\mathbf{r}, s)q_B^+(\mathbf{r}, f_B - s) \tag{2.76}$$

$$\phi_C(\mathbf{r}) = z\int_0^{\kappa_2} ds\, q_C(\mathbf{r}, s)q_C(\mathbf{r}, \kappa_2 - s), \tag{2.77}$$

$$\omega_\alpha(\mathbf{r}) = \sum_{\beta\neq\alpha}\chi_{\alpha\beta}N\phi_\beta(\mathbf{r}) + \eta(\mathbf{r}), \tag{2.78}$$

$$\sum_{\alpha=A,B,C} \phi_\alpha(\mathbf{r}) = 1, \tag{2.79}$$

where $z = \exp(\kappa_2(\Delta\tilde{\mu}_2 - \Delta\tilde{\mu}_1))/\kappa_2$.

The Gibbs free energy density can be computed using the expression,

$$g_{\mathrm{MF}} = \frac{1}{V}\int d\mathbf{r}\left\{\frac{1}{2}\sum_{\alpha\neq\beta}\chi_{\alpha\beta}N\phi_\alpha(\mathbf{r})\phi_\beta(\mathbf{r}) - \sum_\alpha\omega_\alpha(\mathbf{r})\phi_\alpha(\mathbf{r})\right\} - Q_1 - zQ_2. \tag{2.80}$$

This free energy is often used as the starting point for the calculation in grand canonical ensemble.

Chapter 3

Numerical Implementation

The mean-field approximation employed in the self-consistent field theory simplifies the model considerably, but solutions to the mean-field equations are still difficult to obtain due to the nonlinear and non-local nature of the equations. Further approximations exist to derive an analytic expression for the partition function and the chain propagators. Noticeable examples are Leibler's weak segregation theory [17] and Semenov's strong segregation theory [18]. These analytic methods are useful to gain some insights on the system behavior at extreme conditions, but a more generalized method that can be applied to any segregation is desirable. For this purpose, a variety of numerical methods have been developed for the self-consistent field theory. They are powerful tools and capable of giving accurate predictions regarding the complex phase behavior of polymer mixtures.

In this chapter, we discuss the numerical methods used in this thesis. Using the example of AB/C blends, we present the details of procedure to compute the equilibrium structures and phase diagrams of polymer mixtures. In Section 3.1, we present the general procedure to solve the mean-field equations, using an iteration method. Two classes of numerical methods are discussed in detail: the spectral method (Section 3.2) and the finite difference method (Section 3.3). The spectral method is used to calculate the phase diagrams for the AB/C blends, while the finite difference method is employed in the study of micellization in AB/A blends.

3.1 General algorithm

In order to calculate the equilibrium structures of AB/C blends using self-consistent field theory, we have to solve for two sets of unknown fields: the monomer density fields $\{\phi_\alpha(\mathbf{r})\}$ and the chemical potential fields $\{\omega_\alpha(\mathbf{r})\}$. These two fields are closely related and one can be determined with the knowledge of the other one. Therefore, they should be determined in such a way that they do not contradict each other, *i.e.*, the self-consistent condition. In Fig. 3.1 , we show the relation between the density and potential fields.
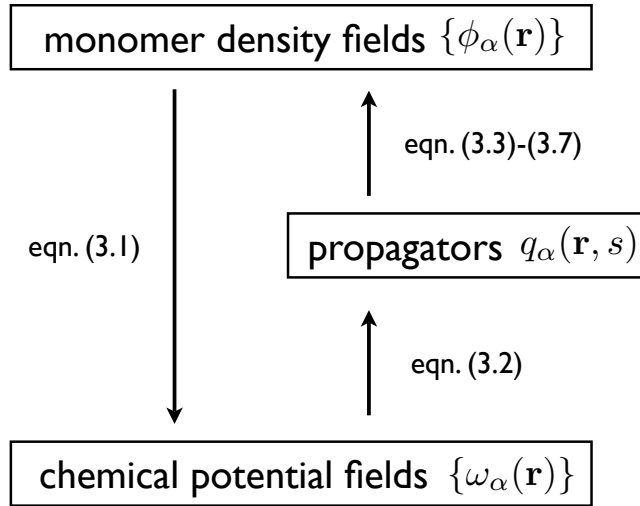
Figure 3.1: A schematic presentation of self-consistent field theory to illustrate the relation between the density fields, the potential fields and the propagators of path integral.

From density fields to potential fields: $\omega_\alpha = \mathscr{F}(\{\phi_\alpha\})$

The potential fields can be evaluated from the densities using

$$\omega_\alpha(\mathbf{r}) = \sum_{\beta \neq \alpha} \chi_{\alpha\beta} N[\phi_\beta(\mathbf{r}) - \bar{\phi}_\beta] + \eta(\mathbf{r}). \tag{3.1}$$

The potential fields include the Flory-Huggins interactions and an Lagrange multiplier field $\eta(\mathbf{r})$ to ensure the incompressibility.

From potential fields to density fields: $\phi_\alpha = \mathscr{G}(\{\omega_\alpha\})$

When the potential fields are known, the densities can be calculated through the end-integrated propagators. For the diblock copolymer AB, the end-integrated propagators $q_\alpha(\mathbf{r}, s)$ and $q_\alpha^+(\mathbf{r}, s)$ ($\alpha = A, B$) are solutions of the modified diffusion equations in the mean field $\omega_\alpha(\mathbf{r})$,

$$\frac{\partial}{\partial s} q_\alpha(\mathbf{r}, s) = \sigma_\alpha^2 \nabla^2 q_\alpha(\mathbf{r}, s) - \omega_\alpha(\mathbf{r}) q_\alpha(\mathbf{r}, s), \tag{3.2}$$

with the initial condition $q_\alpha(\mathbf{r}, 0) = 1$, $q_\alpha^+(\mathbf{r}, 0) = q_\beta(\mathbf{r}, f_\beta)$. For the homopolymer C, one end-integrated propagator $q_C(\mathbf{r}, s)$ is sufficient. It satisfies the same diffusion equation with initial condition $q_C(\mathbf{r}, 0) = 1$.

The density fields then can be calculated from

$$\phi_A(\mathbf{r}) = \frac{\bar{\phi}_1}{Q_1} \int_0^{f_A} \mathrm{d}s\, q_A(\mathbf{r}, s) q_A^+(\mathbf{r}, f_A - s), \tag{3.3}$$

$$\phi_B(\mathbf{r}) = \frac{\bar{\phi}_1}{Q_1} \int_0^{f_B} \mathrm{d}s\, q_B(\mathbf{r}, s) q_B^+(\mathbf{r}, f_B - s), \tag{3.4}$$

$$\phi_C(\mathbf{r}) = \frac{\bar{\phi}_2}{\kappa_2 Q_2} \int_0^{\kappa_2} \mathrm{d}s\, q_C(\mathbf{r}, s) q_C(\mathbf{r}, \kappa_C - s), \tag{3.5}$$

where $\bar{\phi}_A = \bar{\phi}_1 f_A$, $\bar{\phi}_B = \bar{\phi}_1 f_B$, $\bar{\phi}_C = \bar{\phi}_2$. Q_p are single-chain partition functions

$$Q_1 = \frac{1}{V} \int \mathrm{d}\mathbf{r}\, q_A^+(\mathbf{r}, f_A) = \frac{1}{V} \int \mathrm{d}\mathbf{r}\, q_B^+(\mathbf{r}, f_B), \tag{3.6}$$

$$Q_2 = \frac{1}{V} \int \mathrm{d}\mathbf{r}\, q_C(\mathbf{r}, \kappa_2). \tag{3.7}$$

In the numerical implementation of self-consistent field theory, this part of computation is the most time-consuming step due to the non-local and nonlinear nature of the above equations.

Iteration

Formally, we wish to find a solution for the equation

$$\omega_\alpha = \mathscr{F} \cdot \mathscr{G}^{-1}(\{\omega_\alpha\}). \tag{3.8}$$

This is normally done numerically using an iteration method. An iteration method attempts to solve the equation by finding successive approximations to the solution starting from an initial guess. In our case, the following procedure is repeated until the $\{\omega_\alpha\}$ converges:

$$\begin{cases} \omega_\alpha^0 & \leftarrow \quad \text{initial guess}, \\ \omega_\alpha^1 & = \quad \mathscr{F} \cdot \mathscr{G}^{-1}(\{\omega_\alpha^0\}), \\ \omega_\alpha^2 & = \quad \mathscr{F} \cdot \mathscr{G}^{-1}(\{\omega_\alpha^1\}), \\ & \quad \vdots \end{cases} \tag{3.9}$$

Once the iteration ends, the free energy density is given by,

$$\begin{aligned} f & = \frac{1}{V} \int d\mathbf{r} \left\{ \frac{1}{2} \sum_{\alpha \neq \beta} \chi_{\alpha\beta} N \phi_\alpha(\mathbf{r}) \phi_\beta(\mathbf{r}) - \sum_\alpha \omega_\alpha(\mathbf{r}) \phi_\alpha(\mathbf{r}) \right\} \\ & \quad - \sum_p \frac{\bar{\phi}_p}{\kappa_p} \ln Q_p + \sum_p \frac{\bar{\phi}_p}{\kappa_p} \ln(\frac{\bar{\phi}_p}{e}) + \sum_p \mu_{0p} \bar{\phi}_p. \end{aligned} \tag{3.10}$$

3.1.1 General recipe

1. Initialize the potential fields $\{\omega_\alpha(\mathbf{r})\}$. This is done by either using a random number generator or computing from the density profile of a known stable structure.

2. Evaluate the propagators by solving the modified diffusion equation (3.2). Then the density fields $\{\phi_\alpha(\mathbf{r})\}$ can be calculated using eqn. (3.3)-(3.7).

3. Update the new potential fields using eqn. (3.1). If the difference between new and old potential fields is less than the required precession, go to step 4, otherwise return to step 2.

4. Compute the free energy density using eqn. (3.10).

3.2 Spectral method

In the spectral method, the modified diffusion equation is solved in the reciprocal space. If the symmetry of the ordered structure is known, the spectral method is numerically more efficient to compute the equilibrium free energy than any other methods. The key aspect of the spectral method is that the functions of the ordered structures are all periodic functions. Therefore, the density fields $\phi_\alpha(\mathbf{r})$, the potential fields $\omega_\alpha(\mathbf{r})$ and the propagators $q_\alpha(\mathbf{r}, s)$ can all be expanded in a set of smooth basis functions that have the same symmetry of the ordered structure and that are eigenfunctions of the Laplacian operator.

For an ordered structure, the reciprocal lattice vectors $\mathbf{G}$ are completely specified by the space group of that structure. We choose the plane waves $e^{i\mathbf{G}\cdot\mathbf{r}}$ to be the basis functions. Any function $F(\mathbf{r})$ can be expressed in the form

$$F(\mathbf{r}) = \sum_{\mathbf{G}} F(\mathbf{G}) e^{i\mathbf{G}\cdot\mathbf{r}}, \tag{3.11}$$

$$F(\mathbf{G}) = \frac{1}{V} \sum_{\mathbf{G}} F(\mathbf{r}) e^{-i\mathbf{G}\cdot\mathbf{r}}. \tag{3.12}$$

The latter equation is the reverse transformation.

These basic functions satisfy the orthonormal condition

$$\int d\mathbf{r} e^{-i\mathbf{G}'\cdot\mathbf{r}} e^{i\mathbf{G}\cdot\mathbf{r}} = V \delta_{\mathbf{G},\mathbf{G}'}. \tag{3.13}$$

They are also the eigenfunction of the Laplacian operator with eigenvalue $\lambda_{\mathbf{G}} = -|\mathbf{G}|^2$,

$$(\nabla^2 - \lambda_{\mathbf{G}}) e^{i\mathbf{G}\cdot\mathbf{r}} = 0. \tag{3.14}$$

These basis functions can be ordered according to the eigenvalue $|\mathbf{G}|$.

The density and potential fields can be expanded in terms of $e^{i\mathbf{G}\cdot\mathbf{r}}$,

$$\phi_\alpha(\mathbf{r}) = \sum_{\mathbf{G}} \phi_\alpha(\mathbf{G})e^{i\mathbf{G}\cdot\mathbf{r}}, \tag{3.15}$$

$$\omega_\alpha(\mathbf{r}) = \sum_{\mathbf{G}} \omega_\alpha(\mathbf{G})e^{i\mathbf{G}\cdot\mathbf{r}}. \tag{3.16}$$

The ordered structure is then completely specified by the Fourier coefficients $\phi_\alpha(\mathbf{G})$ and $\omega_\alpha(\mathbf{G})$. In Fourier space, the mean-field equations become

$$\phi_A(\mathbf{G}) = \frac{\bar{\phi}_1}{Q_1} \sum_{\mathbf{G}'} \int_0^{f_A} ds\, q_A(\mathbf{G}', s)q_A^+(\mathbf{G} - \mathbf{G}', f_A - s), \tag{3.17}$$

$$\phi_B(\mathbf{G}) = \frac{\bar{\phi}_1}{Q_1} \sum_{\mathbf{G}'} \int_0^{f_B} ds\, q_B(\mathbf{G}', s)q_B^+(\mathbf{G} - \mathbf{G}', f_B - s), \tag{3.18}$$

$$\phi_C(\mathbf{G}) = \frac{\bar{\phi}_2}{\kappa_2 Q_2} \sum_{\mathbf{G}'} \int_0^{\kappa_2} ds\, q_C(\mathbf{G}', s)q_C(\mathbf{G} - \mathbf{G}', \kappa_2 - s), \tag{3.19}$$

$$\omega_\alpha(\mathbf{G}) = \sum_{\beta \neq \alpha} \chi_{\alpha\beta}N[\phi_\beta(\mathbf{G}) - \bar{\phi}_\beta\delta_{\mathbf{G},\mathbf{0}}] + \eta(\mathbf{G}), \tag{3.20}$$

$$\sum_{\alpha=A,B,C} \phi_\alpha(\mathbf{G}) = \delta_{\mathbf{G},\mathbf{0}}. \tag{3.21}$$

The single-chain partition functions Q_p is given by

$$Q_1 = q_A^+(\mathbf{G} = \mathbf{0}, f_A) = q_B^+(\mathbf{G} = \mathbf{0}, f_B), \tag{3.22}$$

$$Q_2 = q_C(\mathbf{G} = \mathbf{0}, \kappa_2). \tag{3.23}$$

The modified diffusion equations for the propagators become

$$\frac{\partial}{\partial s}q_\alpha(\mathbf{G}, s) = -\sum_{\mathbf{G}'} H_\alpha(\mathbf{G}, \mathbf{G}')q_\alpha(\mathbf{G}', s), \tag{3.24}$$

$$\frac{\partial}{\partial s}q_\alpha^+(\mathbf{G}, s) = -\sum_{\mathbf{G}'} H_\alpha(\mathbf{G}, \mathbf{G}')q_\alpha^+(\mathbf{G}', s), \tag{3.25}$$

where the $H_\alpha(\mathbf{G}, \mathbf{G}')$ are defined by

$$H_\alpha(\mathbf{G}, \mathbf{G}') \equiv \sigma_\alpha^2 G^2 \delta_{\mathbf{G},\mathbf{G}'} + \omega_\alpha(\mathbf{G} - \mathbf{G}'). \tag{3.26}$$

The initial conditions for the propagators in the Fourier space are,

$$q_A(\mathbf{G}, 0) = q_B(\mathbf{G}, 0) = q_C(\mathbf{G}, 0) = \delta_{\mathbf{G},\mathbf{0}}, \tag{3.27}$$

$$q_A^+(\mathbf{G}, 0) = q_B(\mathbf{G}, f_B), \tag{3.28}$$

$$q_B^+(\mathbf{G}, 0) = q_A(\mathbf{G}, f_A). \tag{3.29}$$

31

For convenience, we can write $q_\alpha(\mathbf{G}, s)$ into a column vector $\mathbf{q}_\alpha(s)$, and $H_\alpha(\mathbf{G}, \mathbf{G}')$ into a matrix form $\mathbf{H}_\alpha$. We can do that because the reciprocal lattices $\mathbf{G}$ can be ordered. Then the modified diffusion equation can be written in a matrix form:

$$\frac{\partial}{\partial s}\mathbf{q}_\alpha(s) = -\mathbf{H}_\alpha\mathbf{q}_\alpha(s), \tag{3.30}$$

$$\frac{\partial}{\partial s}\mathbf{q}_\alpha^+(s) = -\mathbf{H}_\alpha\mathbf{q}_\alpha^+(s). \tag{3.31}$$

One may immediately notice that these equations have the same form as the time-dependent Schrödinger equation. Thus we can borrow the methods used in quantum mechanics to solve the modified diffusion equation. Formally, the solution at later times s can be obtained by applying the time evolution operator $e^{-s\mathbf{H}_\alpha}$ to the initial states,

$$\mathbf{q}_\alpha(s) = e^{-s\mathbf{H}_\alpha}\mathbf{q}_\alpha(0), \tag{3.32}$$

$$\mathbf{q}_\alpha^+(s) = e^{-s\mathbf{H}_\alpha}\mathbf{q}_\alpha^+(0). \tag{3.33}$$

In order to evaluate the time evolution operator, we need to calculate the eigenvalues and eigenfunctions of the "Hamiltonian" $H_\alpha(\mathbf{G}, \mathbf{G}')$,

$$\sum_{\mathbf{G}'} H_\alpha(\mathbf{G}, \mathbf{G}')\psi_n^\alpha(\mathbf{G}') = \varepsilon_n^\alpha\psi_n^\alpha(\mathbf{G}'). \tag{3.34}$$

Because these operators are Hermitian operators, all the eigenvalues are real and the eigenfunctions form a complete orthonormal set,

$$\sum_{\mathbf{G}} \psi_n^{\alpha*}(\mathbf{G})\psi_m^\alpha(\mathbf{G}) = \delta_{nm}, \tag{3.35}$$

$$\sum_{n} \psi_n^{\alpha*}(\mathbf{G})\psi_n^\alpha(\mathbf{G}') = \delta_{\mathbf{G},\mathbf{G}'}. \tag{3.36}$$

By expanding the propagators in terms of these eigenfunctions, solutions (3.32)-(3.33) can be written explicitly as

$$q_\alpha(\mathbf{G}, s) = \sum_{n} e^{-\varepsilon_n^\alpha s}q_n^\alpha(0)\psi_n^\alpha(\mathbf{G}), \tag{3.37}$$

$$q_\alpha^+(\mathbf{G}, s) = \sum_{n} e^{-\varepsilon_n^\alpha s}q_n^{\alpha+}(0)\psi_n^\alpha(\mathbf{G}), \tag{3.38}$$

where the coefficients $q_n^\alpha(0)$ and $q_n^{\alpha+}(0)$ are determined by the initial conditions,

$$
q_n^\alpha(0) = \psi_n^{\alpha*}(\mathbf{0}), \tag{3.39}
$$

$$
q_n^{\alpha+}(0) = \sum_m e^{-\varepsilon_m^\beta f_\beta}\psi_m^{\beta*}(\mathbf{0})\left[\sum_{\mathbf{G}'}\psi_m^\beta(\mathbf{G}')\psi_n^{\alpha*}(\mathbf{G}')\right]. \tag{3.40}
$$

Using these expressions, the single-chain partition function is given by

$$
Q_1 = \sum_{n,m} e^{-\varepsilon_n^A f_A}\psi_n^A(\mathbf{0})\left[\sum_{\mathbf{G}'}\psi_n^{A*}(\mathbf{G}')\psi_m^B(\mathbf{G}')\right]\psi_m^{B*}(\mathbf{0})e^{-\varepsilon_m^B f_B}, \tag{3.41}
$$

$$
Q_2 = \sum_n e^{-\varepsilon_n^C \kappa_2}\psi_n^{C*}(\mathbf{0})\psi_n^C(\mathbf{G}). \tag{3.42}
$$

The density profiles are

$$
\phi_\alpha(\mathbf{G}) = \frac{\bar{\phi}_1 f_\alpha}{Q_1}\sum_{n,m}\frac{1-e^{-(\varepsilon_m^\alpha-\varepsilon_n^\alpha)f_\alpha}}{(\varepsilon_m^\alpha-\varepsilon_n^\alpha)f_\alpha}e^{-\varepsilon_n^\alpha f_\alpha}\psi_n^{\alpha*}(\mathbf{0})\left[\sum_{\mathbf{G}'}\psi_n^\alpha(\mathbf{G}')\psi_m^\alpha(\mathbf{G}-\mathbf{G}')\right]q_m^{\alpha+}(0) \tag{3.43}
$$

for $\alpha = A, B$, and

$$
\phi_C(\mathbf{G}) = \frac{\bar{\phi}_2}{Q_2}\sum_{n,m}\frac{1-e^{-(\varepsilon_m^C-\varepsilon_n^C)\kappa_2}}{(\varepsilon_m^C-\varepsilon_n^C)\kappa_2}e^{-\varepsilon_n^C \kappa_2}\psi_n^{C*}(\mathbf{0})\left[\sum_{\mathbf{G}'}\psi_n^C(\mathbf{G}')\psi_m^C(\mathbf{G}-\mathbf{G}')\right]\psi_m^{C*}(\mathbf{0}). \tag{3.44}
$$

The accuracy of the spectral method depends on M, the number of basis functions used in expansion (3.15)-(3.16). The advantage of using spectral method lies in its excellent convergence over M. If $q_M(x)$ is the approximation to a continuous function $q(x)$ using a truncated basis of M basis functions, the error $|q(x) - q_M(x)|$ can decay more rapidly than any finite power of $1/M$ as $M \to \infty$ [22]. In practice, certain accuracy can be reached by using a small M.

3.2.1 Restricted spectral method

The most time-consuming part of the spectral method is to solve the eigen-equations for the matrix (3.26). In general, this requires $O(M^3)$ operations for a $M \times M$ matrix, which is a very expensive calculation. For ordered structures, it is

possible to use fewer basis functions by exploiting the symmetry of the structure under investigation. The basic idea is that for an ordered structure, some of the Fourier coefficients are not independent, thus we can reduce the number of basic functions by grouping the ones that are related. This leads to a set of new basis functions that can be written as a linear combination of old plane-wave basis functions

$$f_n(\mathbf{r}) = \frac{1}{\sqrt{N_n}} \sum_{i \in n} S_i^n e^{i\mathbf{G}_i^n \cdot \mathbf{r}}, \tag{3.45}$$

where the wave vectors $\mathbf{G}_i^n$ are related by the point group symmetry operation and satisfy the relation $|\mathbf{G}_i^n|^2 = \lambda_n$, $i.e.$, they are within one star. Here n is used to label the new basis functions. The factors $S_i^n = \pm 1$ according to the space group and N_n is the number of reciprocal lattice vectors belonging to the n-th star. The definition of $f_n(\mathbf{r})$ can be found from ref. [36].

Similar to the previous section, we can expand the density and potential fields in terms of $f_n(\mathbf{r})$,

$$\phi_\alpha(\mathbf{r}) = \sum_n \phi_n^\alpha f_n(\mathbf{r}), \tag{3.46}$$

$$\omega_\alpha(\mathbf{r}) = \sum_n \omega_n^\alpha f_n(\mathbf{r}). \tag{3.47}$$

The mean-field equations can also be written in terms of these coefficients. In particular, the Hamiltonians become symmetric matrices with matrix elements,

$$H_{nm}^\alpha = \sigma_\alpha^2 \lambda_n \delta_{nm} + \sum_l \Gamma_{nml} \omega_l^\alpha, \tag{3.48}$$

where the coefficients Γ_{nml} are defined by integral over the multiplication of three basis functions,

$$\begin{aligned}
\Gamma_{nml} &= \frac{1}{V} \int d\mathbf{r} f_n(\mathbf{r}) f_m(\mathbf{r}) f_l(\mathbf{r}) \\
&= \frac{1}{\sqrt{N_n N_m N_l}} \sum_{i \in n} \sum_{j \in m} \sum_{k \in l} S_i^n S_j^m S_k^l \delta_{\mathbf{G}_i^n + \mathbf{G}_j^m + \mathbf{G}_k^l, \mathbf{0}}.
\end{aligned} \tag{3.49}$$

The eigenvalues and eigenfunctions of the matrices H^α_{nm} are found by solving the equations

$$\sum_m H^\alpha_{nm} \psi^\alpha_{mi} = \varepsilon^\alpha_i \psi^\alpha_{ni}, \tag{3.50}$$

where i labels the eigenvalues and eigenfunctions. The eigenfunctions form a complete orthonormal set,

$$\sum_n \psi^\alpha_{ni} \psi^\alpha_{nj} = \delta_{ij}, \qquad \sum_i \psi^\alpha_{ni} \psi^\alpha_{mi} = \delta_{nm}. \tag{3.51}$$

The end-integrated propagators can be expressed in the form,

$$q^\alpha_n(t) = \sum_i e^{-\varepsilon^\alpha_i t} \psi^\alpha_{1i} \psi^\alpha_{ni}, \tag{3.52}$$

$$q^{\alpha+}_n(t) = \sum_{i,j} e^{-\varepsilon^\alpha_i t} \psi^\alpha_{ni} \left[\sum_m \psi^\alpha_{mi} \psi^\beta_{mj} \right] e^{-\varepsilon^\beta_j f_\beta} \psi^\beta_{1j}. \tag{3.53}$$

The single-chain partition functions and density coefficients can be written as,

$$Q_1 = q^{A+}_1(f_A) = \sum_{i,j} e^{-\varepsilon^A_i f_A} \psi^A_{1i} \left[\sum_m \psi^A_{mi} \psi^B_{mj} \right] e^{-\varepsilon^B_j f_B} \psi^B_{1j}, \tag{3.54}$$

$$Q_2 = q^C_1(\kappa_2) = \sum_i e^{-\varepsilon^C_i \kappa_2} \psi^C_{1i} \psi^C_{1i}, \tag{3.55}$$

$$\phi^\alpha_n = \frac{\bar\phi_1}{Q_1} \int_0^{f_\alpha} ds \sum_{m,l} \Gamma_{nml} q^\alpha_m(s) q^{\alpha+}_l(f_\alpha - s) \qquad \alpha = A, B, \tag{3.56}$$

$$\phi^C_n = \frac{\bar\phi_2}{\kappa_2 Q_2} \int_0^{\kappa_2} ds \sum_{m,l} \Gamma_{nml} q^C_m(s) q^C_l(\kappa_2 - s). \tag{3.57}$$

For AB/C blend, it is useful to construct the following quantities using the eigenvalues and eigenfunctions of H^α_{nm},

$$v^A_i = e^{-\varepsilon^A_i f_A}, \qquad v^B_i = e^{-\varepsilon^B_i f_B}, \qquad v^C_i = e^{-\varepsilon^C_i \kappa_2}, \tag{3.58}$$

$$L^{AB}_{ij} = \sum_n \psi^A_{ni} \psi^B_{nj} = L^{BA}_{ji}, \tag{3.59}$$

$$T^A_i = \sum_j L^{AB}_{ij} v^B_j \psi^B_{1j}, \qquad T^B_i = \sum_j L^{BA}_{ij} v^A_j \psi^A_{1j}, \tag{3.60}$$

$$S^A_{n,ij} = \sum_{m,l} \Gamma_{nml} \psi^A_{mi} \psi^A_{lj}, \qquad S^B_{n,ij} = \sum_{m,l} \Gamma_{nml} \psi^B_{mi} \psi^B_{lj}, \qquad S^C_{n,ij} = \sum_{m,l} \Gamma_{nml} \psi^C_{mi} \psi^C_{lj}, \tag{3.61}$$

$$g_{ij}^A = \frac{\psi_{1i}^A(v_i^A - v_j^A)}{(\varepsilon_j^A - \varepsilon_i^A)f_A}, \qquad g_{ij}^B = \frac{\psi_{1i}^B(v_i^B - v_j^B)}{(\varepsilon_j^B - \varepsilon_i^B)f_B}, \qquad g_{ij}^C = \frac{\psi_{1i}^C(v_i^C - v_j^C)}{(\varepsilon_j^C - \varepsilon_i^C)\kappa_2}. \tag{3.62}$$

Using these quantities, the single-chain partition functions are given by,

$$Q_1 = \sum_i v_i^A \psi_{1i}^A T_i^A = \sum_i v_i^B \psi_{1i}^B T_i^B, \tag{3.63}$$

$$Q_2 = \sum_i v_i^C \psi_{1i}^C \psi_{1i}^C. \tag{3.64}$$

The density coefficients are

$$\phi_n^A = \frac{\bar{\phi}_1 f_A}{Q_1} \sum_{i,j} g_{ij}^A S_{n,ij}^A T_j^A, \tag{3.65}$$

$$\phi_n^B = \frac{\bar{\phi}_1 f_B}{Q_1} \sum_{i,j} g_{ij}^B S_{n,ij}^B T_j^B, \tag{3.66}$$

$$\phi_n^C = \frac{\bar{\phi}_2}{Q_2} \sum_{i,j} g_{ij}^C S_{n,ij}^C \psi_{1j}^C. \tag{3.67}$$

The coefficients of the fields ω_n^α are determined from the self-consistent conditions,

$$\omega_n^\alpha = \sum_{\beta \neq \alpha} \chi_{\alpha\beta} N[\phi_n^\beta - \bar{\phi}_\beta \delta_{n,1}] + \eta_n, \tag{3.68}$$

where the coefficients η_n are to be adjusted so that the system satisfies the incompressibility condition,

$$\phi_n^A + \phi_n^B + \phi_n^C = \delta_{n,1}. \tag{3.69}$$

The free energy density is

$$f = \frac{1}{2} \sum_{\alpha \neq \beta} \sum_n \chi_{\alpha\beta} N \phi_n^\alpha \phi_n^\beta - \sum_\alpha \sum_n \omega_n^\alpha \phi_n^\alpha - \bar{\phi}_1 \ln Q_1 - \frac{\bar{\phi}_2}{\kappa_2} \ln Q_2. \tag{3.70}$$

Notice that the $n = 1$ terms are simply the free energy density of the homogeneous phase, then the mean-field free energy per chain less that of the homogeneous phase is given by

$$\Delta f = \frac{1}{2} \sum_{\alpha \neq \beta} \sum_{n=2} \chi_{\alpha\beta} N \phi_n^\alpha \phi_n^\beta - \sum_\alpha \sum_{n=2} \omega_n^\alpha \phi_n^\alpha - \bar{\phi}_1 \ln Q_1 - \frac{\bar{\phi}_2}{\kappa_2} \ln Q_2. \tag{3.71}$$

3.2.2 Restricted spectral method recipe

1. At a given point of the parameter space $(f_A, \kappa_2, \bar{\phi}_1, \chi_{\alpha\beta}N)$ and for a given phase with a specified space group, determine the reciprocal lattice vectors $\{\mathbf{G}_i^n\}$ and the coefficients S_i^n. Calculate the coefficients Γ_{nml} and λ_n.

2. Choose a lattice period D.

3. Make an initial guess for ϕ_n^α and calculate the initial values of ω_n^α using

$$\omega_n^\alpha = \sum_{\beta \neq \alpha} \chi_{\alpha\beta} N[\phi_n^\beta - \bar{\phi}_\beta \delta_{n,1}] + \eta_n, \tag{3.72}$$

assuming $\eta_n = 0$. Notice that $\phi_1^\alpha = \bar{\phi}_\alpha$, $\omega_1^\alpha = 0$ and they are unchanged during iterations.

4. Compute the matrix elements (3.50). Solve the eigenvalue problem using the LAPACK library [*] ,

$$\sum_m H_{nm}^\alpha \psi_{mi}^\alpha = \varepsilon_i^\alpha \psi_{ni}^\alpha. \tag{3.73}$$

Once we know ε_i^α and ψ_{ni}^α, Q_p and ϕ_n^α can be calculated using eqns. (3.63)-(3.67).

5. Calculate the Lagrange multiplier

$$\eta_n = \frac{\sum_\alpha \omega_n^\alpha X_\alpha}{\sum_\alpha X_\alpha}, \tag{3.74}$$

where

$$
\begin{aligned}
X_A &= \chi_{BC}(\chi_{AB} + \chi_{AC} - \chi_{BC}), & (3.75)\\
X_B &= \chi_{AC}(\chi_{BC} + \chi_{AB} - \chi_{AC}), & (3.76)\\
X_C &= \chi_{AB}(\chi_{AC} + \chi_{BC} - \chi_{AB}). & (3.77)
\end{aligned}
$$

---

[*]http://www.netlib.org/lapack/

Calculate the changes (for $n > 1$),

$$\delta\omega_n^\alpha \quad = \quad \sum_{\beta \neq \alpha} \chi_{\alpha\beta} N \phi_n^\beta + \eta_n - \omega_n^\alpha, \tag{3.78}$$

$$\delta\phi_n \quad = \quad \sum_\alpha \delta\phi_n^\alpha. \tag{3.79}$$

If these changes are smaller than a certain convergence criterion, proceed to next step. Otherwise, calculate new ω_n^α using,

$$\omega_n^{\alpha'} = \omega_n^\alpha + \gamma\delta\omega_n^\alpha - \beta\delta\phi_n, \tag{3.80}$$

where γ and β are small positive numbers ($\beta = \gamma = 0.1$ are reasonable), and return to step 2.

6. Compute the free energy density using eqn. (3.71).

The procedure is then repeated for a different lattice period, D, until the lowest free energy density is obtained.

3.3 Finite difference method

When no spatially periodic structures are expected in the system under study, or there is no prior knowledge of the equilibrium morphologies, a generalized form of the spectral method can be used [37]. On the other hand, for some cases it is advantageous to use the real-space method. The real-space method is easy to understand conceptually, and the implementation is straightforward. A variety of techniques have been developed to solve the self-consistent equations in real space [15, 20, 21, 22, 38, 39, 40].

As the name suggests, we solve the problem in the real space. A computational grid of discrete points is assigned to the volume V, and the monomer density ϕ, the potential field ω, and the propagator $q(x, s)$ are sampled at each grid point. To

demonstrate the numerical method, we focus on a one-dimensional modified diffusion equation

$$\frac{\partial}{\partial s}q(x,s) = \frac{b^2}{6}\nabla_x^2 q(x,s) - \omega(x)q(x,s) \qquad (3.81)$$

with the initial condition $q(x,0) = 1$ and suitable boundary conditions at the edges of some interval $0 \leq x \leq L$. We use m to label the different coordinates. $m = 0, 1, 2$ corresponds to the Cartesian, cylindrical and spherical coordinates, respectively. For the latter two cases, we assume the variables only depends on the radius $r = x$ and there is no angular dependence.

3.3.1 Finite difference method

A standard technique for obtaining a numerical solution of an initial value problem like eqn. (3.81) is to apply the finite difference method. For simplicity we use the equally spaced discretization and use N_x and N_s points in the interval $x \in [0, L]$ and $s \in [0, 1]$, respectively:

$$x_j = j\Delta x, \quad j = 0, 1, \ldots, N_x - 1, \qquad (3.82)$$

$$s_n = n\Delta s, \quad n = 0, 1, \ldots, N_s - 1. \qquad (3.83)$$

The value of the propagator $q(x,s)$ at the grid point (x_j, s_n) will be denoted by

$$q_j^n = q(x_j, s_n). \qquad (3.84)$$

The next step is to introduce approximations for the relevant derivatives. Consider the grid points of $j - 1$, j and $j + 1$, as shown in Fig. 3.3.1. $S_{j,1}$ is the area of the interface separating x_{j-1} and x_j. $S_{j,2}$ is defined similarly. These interfaces are parallel planes for $m = 0$, concentric cylindrical shells for $m = 1$, and concentric spherical shells for $m = 2$.
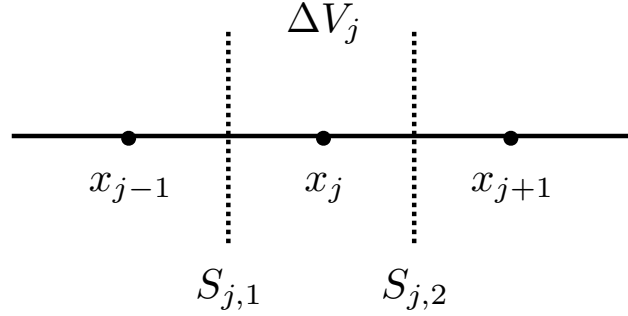
Figure 3.2: The spatial grid for the finite difference method.

The idea is to compute the Laplacian using the integral form of the Gaussian law

$$\int_V \nabla \cdot (\nabla q) \mathrm{d}V = \int_S (\nabla q) \mathrm{d}S, \tag{3.85}$$

where the volume integration is computed over the space in between of interface $S_{j,1}$ and $S_{j,2}$. Writing eqn. (3.85) in discrete form, we have

$$(\nabla^2 q)_j \Delta V_j = (\nabla q)_{S_{j,2}} S_{j,2} - (\nabla q)_{S_{j,1}} S_{j,1}. \tag{3.86}$$

The gradient terms on the right-hand side of eqn. (3.86) are evaluated at the interface,

$$(\nabla q)_{S_{j,1}} = \frac{q_j - q_{j-1}}{\Delta x}, \tag{3.87}$$

$$(\nabla q)_{S_{j,2}} = \frac{q_{j+1} - q_j}{\Delta x}. \tag{3.88}$$

The final form is

$$(\nabla^2 q)_j = \mathbf{L}_x q_j + O(\Delta x^2) \tag{3.89}$$

with

$$\mathbf{L}_x q_j = L_x(j,2) q_{j+1} + L_x(j,1) q_{j-1} - [L_x(j,2) + L_x(j,1)] q_j, \tag{3.90}$$

and

$$L_x(j,1) = \frac{S_{j,1}}{\Delta V_j \Delta x}, \quad L_x(j,2) = \frac{S_{j,2}}{\Delta V_j \Delta x}. \tag{3.91}$$

40

In this expression, $\mathbf{L}_x$ represents the one-dimension discrete form of the Laplacian operator. The discretization is second order accurate in x.

3.3.2 The Crank-Nicolson scheme

We use the Crank-Nicolson scheme [41] to discretize the modified diffusion equation,

$$\frac{q_j^{n+1} - q_j^n}{\Delta s} = \frac{b^2}{6}\mathbf{L}_x \frac{1}{2}(q_j^{n+1} + q_j^n) - \omega_j \frac{1}{2}(q_j^{n+1} + q_j^n). \tag{3.92}$$

This scheme is unconditionally stable for any size of contour step Δs and second order accurate in s.

We use $\mathbf{q}^n$ to denote the a column vector of N_x elements, each one taking the value of q_j^n. Then eqn. (3.92) can be written in matrix form:

$$\left(1 - \frac{b^2 \Delta s}{12}\mathbf{L}_x + \frac{\Delta s}{2}\omega\right)\mathbf{q}^{n+1} = \left(1 + \frac{b^2 \Delta s}{12}\mathbf{L}_x - \frac{\Delta s}{2}\omega\right)\mathbf{q}^n. \tag{3.93}$$

Formally, the solution is

$$\mathbf{q}^{n+1} = \left(1 - \frac{b^2 \Delta s}{12}\mathbf{L}_x + \frac{\Delta s}{2}\omega\right)^{-1}\left(1 + \frac{b^2 \Delta s}{12}\mathbf{L}_x - \frac{\Delta s}{2}\omega\right)\mathbf{q}^n \tag{3.94}$$

Knowing $\mathbf{q}^n$, the propagator at next time step $\mathbf{q}^{n+1}$ can be calculated by two matrix operations: a matrix inversion followed by a multiplication of two matrices. In general, a matrix inversion or multiplication for a $N_x \times N_x$ matrix requires $O(N_x^2)$ operations, which imposes a huge computational cost when N_x becomes large. Fortunately the matrix in (3.94) is tridiagonal and its inverse can be efficiently computed in $O(N_x)$ [41]. We repeat the calculation in (3.94) $N_s - 1$ times starting with $\mathbf{q}^0 = \mathbf{1}$ to obtain $q(x_j, s_n)$. The total number of operation for a one-dimensional system is of order $O(N_x N_s)$. Similar procedure can be used to calculate $q^+(x_j, s_n)$.

3.3.3 Finite difference method recipe

1. Depending on the problem, choose a suitable coordinate.

2. Choose a suitable simulation box $[0, L]$ and reasonable values for the grid spacing Δx and the contour step Δs. The discretization scheme (3.82)-(3.83) should be determined by the problem and the required accuracy.

3. Compute the one-dimensional Laplacian operator $\mathbf{L}_x$ using eqn. (3.90)-(3.91) .

4. All the relevant functions are defined at the grid points:

$$\phi_j = \phi(x_j), \qquad \omega_j = \omega(x_j), \tag{3.95}$$

$$q_j^n = q(x_j, s_n), \qquad (q^+)_j^n = q^+(x_j, s_n). \tag{3.96}$$

Make an initial guess for ω_j, either by using a random number generator or computing from a known stable density profile.

5. Calculate the matrix element

$$\mathscr{U}(\Delta s) = \left(\mathbf{1} - \frac{b^2 \Delta s}{12}\mathbf{L}_x + \frac{\Delta s}{2}\omega\right)^{-1}\left(\mathbf{1} + \frac{b^2 \Delta s}{12}\mathbf{L}_x - \frac{\Delta s}{2}\omega\right) \tag{3.97}$$

6. Repeat the following operation $N_s - 1$ times

$$\mathbf{q}^{n+1} = \mathscr{U}(\Delta s)\mathbf{q}^n, \tag{3.98}$$

with the initial condition $\mathbf{q}^0 = 1$.

7. Once the propagators q_j^n are determined, the monomer densities ϕ_j can be calculated using eqn. (3.3)-(3.7). The free energy density f can be computed by eqn. (3.10). These integrals can be evaluated using simple trapezoidal rule or Simpson's rule [41].

8. If the free energy converges to a stable value, the iteration ends. Otherwise, update the potential fields by using eqn. (3.1) and return to step 5.

3.3.4 ADI (Alternating-Direction Implicit) method

The finite difference method can also be applied to system with two spatial dimensions [41]. Examples are two-dimensional Cartesian coordinate (x, y) and cylindrical coordinate with the rotational symmetry (ρ, z). In this case, the Laplacian operator is of the form $\mathbf{L}_x + \mathbf{L}_y$, where $\mathbf{L}_x$ represents the differencing in x and $\mathbf{L}_y$ that in y. The modified diffusion equation then can be discretized in two half-steps:

$$\frac{q_{i,j}^{n+1/2} - q_{i,j}^n}{\Delta s/2} = \frac{b^2}{6}(\mathbf{L}_x q_{i,j}^{n+1/2} + \mathbf{L}_y q_{i,j}^n) - \omega_{i,j}\frac{1}{2}(q_{i,j}^{n+1/2} + q_{i,j}^n), \qquad (3.99)$$

$$\frac{q_{i,j}^{n+1} - q_{i,j}^{n+1/2}}{\Delta s/2} = \frac{b^2}{6}(\mathbf{L}_x q_{i,j}^{n+1/2} + \mathbf{L}_y q_{i,j}^{n+1}) - \omega_{i,j}\frac{1}{2}(q_{i,j}^{n+1} + q_{i,j}^{n+1/2}). \quad (3.100)$$

Similar to the one-dimension problem, matrix inversion can be used to solve $\mathbf{q}^{n+1}$ from $\mathbf{q}^n$, through a middle step $\mathbf{q}^{n+1/2}$,

$$\mathbf{q}^{n+1/2} = \left(1 - \frac{b^2\Delta s}{12}\mathbf{L}_x + \frac{\Delta s}{4}\omega\right)^{-1}\left(1 + \frac{b^2\Delta s}{12}\mathbf{L}_y - \frac{\Delta s}{4}\omega\right)\mathbf{q}^n, \qquad (3.101)$$

$$\mathbf{q}^{n+1} = \left(1 - \frac{b^2\Delta s}{12}\mathbf{L}_y + \frac{\Delta s}{4}\omega\right)^{-1}\left(1 + \frac{b^2\Delta s}{12}\mathbf{L}_x - \frac{\Delta s}{4}\omega\right)\mathbf{q}^{n+1/2}. \quad (3.102)$$

We use the ADI method to calculate the isolated micelle under confinement.

Chapter 4

Phase Behavior of AB/C Blends

The development of new polymeric materials is driven by increasingly complicated requirements of advanced engineering, as well as by the desire to improve material properties and reduce production cost. Beside synthesizing new types of homopolymers and copolymers, blending different polymers provides another route to obtain new materials [42, 43]. Polymer blends can have combinative and enhanced properties of their components. From a thermodynamic point of view, polymer blends may be miscible, partially miscible, or immiscible. The physical properties of polymer blends vary drastically in these different states. From this perspective, a good understanding of the phase behavior of polymer blends is crucial. Because polymer blends are composed of more than one element, their phase behavior is controlled by a large number of parameters, such as chain lengths, monomer interactions and polymer architectures. Due to the very large parameter space, theoretical study is crucially important to understand the phase behavior and material properties in this complex system.

Polymer blends containing block copolymers are of considerable interest because of their remarkable structural properties [1]. One intriguing feature of block copolymers is that they can self-assemble into periodic structures on the length scale of tens of nanometer. The simplest block copolymer/homopolymer blend consists of diblock copolymers and homopolymers that are chemically identical to one of the blocks of the copolymers (AB/A system). There have been extensive studies on this system, both

in experiment and theory [44, 26, 45, 46, 47, 48, 49]. The phase diagrams of AB/A blends exhibit both macrophase separation and microphase separations. The phase behavior depends on the volume fraction of the homopolymer ϕ_H, and the relative chain length of the homopolymer κ comparing to the copolymer. In general, there are three different cases: (i) $\kappa < 1$. In this case, the chain length of the homopolymers is less than that of the copolymers. The concentration of the short homopolymers is roughly uniform throughout the region of the corresponding block, and the microphase separation exists over a wide range of homopolymer concentration. (ii) $\kappa \sim 1$. The length of the homopolymers is comparable to the copolymers, and the homopolymers will accumulate close to the center of the domain of the corresponding block. The system tends to be microphase separated when the homopolymer concentration is small, and undergoes macrophase separation at large homopolymer concentration. (iii) $\kappa > 1$. The long homopolymers tend to be separated from the copolymers, and the macrophase separation region appears dominantly in the phase diagram. The above argument gives a qualitative description of the influence of the homopolymer length, but a quantitative definition of these regions is still lacking.

More generally, it will be interesting to explore the system in which the homopolymers are chemically distinct from both blocks of the copolymers (AB/C system). Compared to the AB/A blends, one significant change is that the number of interaction parameters required to describe the system increases from one to three (the three Flory-Huggins parameters χ_{AB}, χ_{BC} and χ_{AC}). Although the parameter space of a general AB/C system is too large to be mapped out completely, it is possible to compute some characteristic phase diagrams. These phase diagrams can be viewed as a starting point to understand the complex phase behaviors of the blends, and also to shed some light on possible future experiments.

In our study, we make some simplifications to a general AB/C blend. First we assume the interactions between $\chi_{BC} > 0$ and $\chi_{AC} = 0$, which means the added homopolymer C tends to accumulate in the region where A-block is occupied. This setup resembles the AB/A system, but with the freedom of adjusting the interaction between the homopolymer and the other block, while keeping χ_{AB} constant. Furthermore, we consider only the classical phases: lamellae (LAM), cylinders on a hexagonal lattice (HEX), and spheres on a body-centered cubic lattice (BCC). Complex structures, such as close-packed spheres, perforated lamellae and bi-continuous cubic phases, can also occur for certain parameters [26]. In general they are found only in narrow regions between the classical phases. In this study, we are more interested in the evolution of the ordered structure by varying different parameters, therefore restrict ourselves to the three classical phases. The main interest of this study is about asymmetric diblock copolymers, and we focus on the effect of the homopolymer length and interaction parameters on the phase transition.

Our study can be viewed as an extension of the work of Matsen [45] and Janert and Schick [46]. Matsen examined the AB/A system in the weakly segregated region. One interesting phenomena occurs when blending A homopolymers to diblock copolymers where A is the majority component. The blend starts with hexagonal structure, and changes to lamellar structure when small amount of homopolymer are added, and then switches back to hexagonal structure with more homopolymers added. We will give a detailed analysis of this phenomenon and its origin. Janert and Schick also studied AB/A blends and focused on the effect of the homopolymer chain length. But their blends consist of symmetric diblock copolymers, while our work extends to the asymmetric copolymers.

4.1 Phase diagrams

We solve the self-consistent equations in the grand canonical ensemble using the spectral method. For each blend parameters, we calculate the free energy for different morphologies and the one with lowest free energy is the stable structure. Although we work in the grand-canonical ensemble, we present our results in terms of the canonical variables. For a general AB/C system, there are six parameters $(\kappa, f_A, \phi_H, \chi_{AB}N, \chi_{BC}N, \chi_{AC}N)$ controlling the phase behavior. We set $\chi_{AC}N = 0$ as discussed before, which results a parameter space of five dimensions. We plot our results using two-dimensional phase diagrams, with the abscissa always being the homopolymer concentration ϕ_H. These figures can be viewed as two-dimensional cross-sections of the five-dimensional parameter space.

Figure 4.1 shows a typical phase diagram for the blend with parameters $\chi_{AB}N = 11.0$, $\chi_{BC}N = 12.0$, $\chi_{AC}N = 0$ and $\kappa = 1.0$, plotted in the ϕ_H-f_A plane. This phase diagram is similar to the results from Matsen [45] because the difference between $\chi_{AB}N$ and $\chi_{BC}N$ is small, thus our system resembles the AB/A system. Different phases are labelled as DIS (disordered or homogeneous), LAM (lamellae), HEX (cylinders on a hexagonal lattice), BCC (spheres on a body-centered cubic lattice) and 2-phase (macrophase separation). These short-handed notations are used throughout this thesis.

Depending on the diblock copolymer composition, the blends undergo different morphology transitions when the homopolymer concentration increases. Two different phase sequences exist, distinguished by whether the macrophase separation appears after large amount of homopolymer are added. When A is the minority component, the pure diblock copolymers favor a structure which has curved interfaces to adopt the volume asymmetry between A and B. When small amount of homopolymer is added, the blend exhibits a transition to a structure with less curved interfaces (BCC

Figure 4.1: Phase diagram of AB/C blend with parameters $\chi_{AB}N = 11.0$, $\chi_{BC}N = 12.0$, $\chi_{AC}N = 0$ and $\kappa = 1.0$. The results are plotted in terms of the homopolymer volume fraction ϕ_H and the A-monomer fraction of the diblock f_A. For clarity, only the largest 2-phase region is labeled.

to HEX, or HEX to LAM). When the concentration of homopolymers is increased to certain degree , the homopolymers and copolymers are separated into at a macroscopic scale. Each region is either homopolymer-rich or copolymer-rich. The fraction of copolymer-rich regions shrink when more homopolymers are added into the blends, and eventually the disordered phase is reached again when significant amount of homopolymers are added.

The second scenario happens when A is the majority component of the diblock copolymer. The signature of this case is the disappearance of the 2-phase region in the phase diagram. Also, a reverse of phase transitions seems to occur when the homopolymer concentration is low. For example, at $f_A = 0.55$, the blend starts with HEX structure for pure diblock copolymers. When small amount of homopolymers are added, the blend changes to LAM structure and then switches back to HEX structure. This feature appears as a *bump* of the transition lines in the ϕ_H-f_A phase diagram. When more homopolymers are added, the blend undergoes an unbinding transition where the spacing of the ordered structure increases and eventually diverges at certain homopolymer concentration. Disordered phase is reached after the unbinding transition.

In the following, we will discuss these two cases separately, and focus on the effect of the homopolymer chain length and the monomer-monomer interactions.

4.2 Case I: $f_A < 0.5$

For pure diblock copolymers with $f_A < 0.5$, the A-monomers forms the core of the structure and arranges on a Bravais lattice. When the homopolymers C are added, there are more B-monomers and less A-monomers to interact with C, while C-monomers have a repulsive interaction with B.

We study blends with parameters $\chi_{AB}N = 11.0$, $\chi_{BC}N = 14.0$ and $\chi_{AC}N = 0$, where the $\chi_{BC}N$ value is chosen higher than before in order to enhance the B/C interaction. Fig. 4.2 shows a partial phase diagram near $f_A = 0.457$ (this is the f_A value of LAM-HEX boundary for pure diblock copolymers). The phase boundaries are two lines close to each other. Above the lines is the LAM phase and below is the HEX phase, with the LAM-HEX coexistence in between the lines. Blends with three different κ values are shown here to demonstrate the effect of the homopolymer length. For short homopolymers ($\kappa = 0.5$), the value of f_A at the LAM-HEX boundary decreases as the homopolymer concentration increases. As the homopolymer length becomes comparable to the copolymer, the slope of the phase boundary line become positive. Longer homopolymers has even steeper positive slope, as shown in Fig. 4.2 for $\kappa = 1.5$.
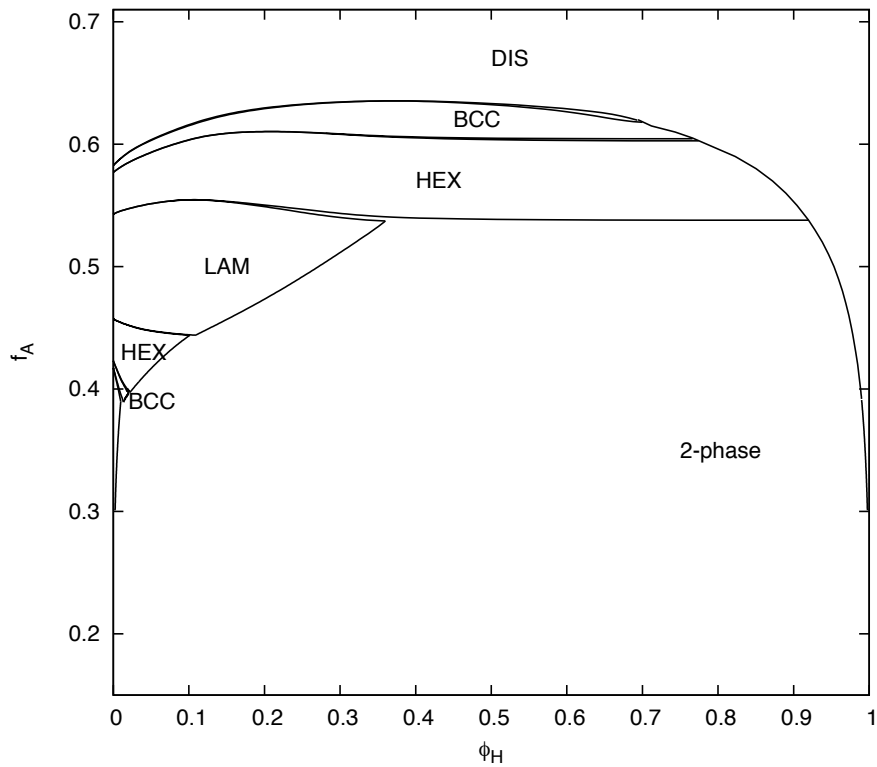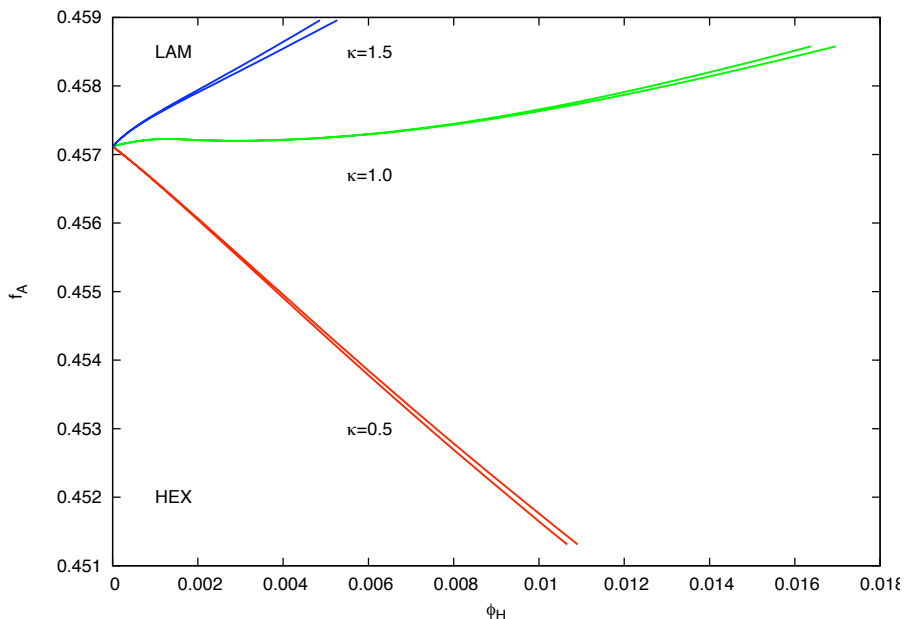

Figure 4.2: Phase diagram of AB/C blend with parameters $\chi_{AB}N = 11.0$, $\chi_{BC}N = 14.0$ and $\chi_{AC}N = 0$ for three different value of $\kappa = 0.5$, 1.0 and 1.5. The results are plotted in ϕ_H-f_A axes.

This phenomena can be explained by the competition between the entropy and energy. Since the A/C repulsive interaction is weaker than the B/C interaction, homopolymers C mostly accumulate in the A-rich region. When the concentration of the homopolymer increases, the homopolymers tend to increase the size of the A-rich region and cause the blend to make a transition to a structure in which A-monomers occupy more space compared to the B-monomers (HEX to LAM for f_A is small). In this way the extra space gained allows homopolymer C to settle, resulting the negative slope of the phase boundary line.

Beside the entropy effect, there is also the energy effect which tends to reduce the interaction energy by minimizing the contact between B and C. This will force the A-rich region where C monomers are mostly accumulated to contract, and counteract the expansion of A-rich region due to the entropy effect.

For short homopolymers, the entropy effect dominates, so the slope of the LAM-HEX boundary is negative. As the length of the homopolymer approaches that of the diblock, the repulsive interaction between B and C becomes stronger and the energy effect becomes relevant. When homopolymers are added, the tendency of the A-rich region to expand in order to accompany more homopolymers starts to compete with its tendency to contract in order to minimize the unfavorable B/C contacts. The energy effect becomes more important for longer homopolymers, thus causes the LAM-HEX boundary line to have a positive slope.

We can also analyze the density profiles and calculate the size of the microstructure to gain some insight of this phenomena. In Figure 4.3, we plot the period of the LAM structure and the relative size of the A-rich region as a function of homopolymer concentration ϕ_H. The parameter for the blends are $\chi_{AB}N = 11.0$, $\chi_{BC}N = 14.0$, $\chi_{AC}N = 0$ and $f_A = 0.46$. In this calculation, the size of the A-rich region is measured along the direction normal to the interface, and defined as twice the distance from

the lamellae center to the point where the second derivative of $\phi_A + \phi_C$ is zero. Here we want to emphasize that the period is calculated by minimizing the free energy for a lamellar structure, and it does not necessarily mean that the LAM phase is stable. We also plot the monomer-density of C for blends with the same parameters and homopolymer concentration $\phi_H = 0.04$, as shown in Figure 4.4. The density profiles are plotted as a function of distance from the center of the A-rich region. Both figures include three different length of the homopolymers $\kappa = 0.5, 1.0, 1.5$.

For the three different lengths of the homopolymers considered here, the period of the LAM phase is a monotonic increasing function of the homopolymer concentration. Although contraction of the period has been observed for LAM phase when very short homopolymers are added [49], for homopolymers whose length is on the same order as that of copolymer, the swelling of the ordered structure is more common. Since the added homopolymer C tends to accumulate inside the A-rich region, we would also expect the the relative size of A-rich region to increase as well. However, as shown in Figure 4.3(b), the relative size of A-rich region actually decreases when small amount of homopolymers are added, and the tendency of decreasing is more distinct for longer homopolymers. This strange behavior can be explained by considering how the homopolymers distribute. As seen in Figure 4.4, the high-weight homopolymers ($\kappa = 1.5$) have a stronger segregation comparing to the short homopolymers ($\kappa = 0.5$). The concentrated C monomers form a well-defined C-rich layer near the middle of A-rich region, thus forming an A-attractive layer. The A monomers tend to gather close to the C-rich layer, resulting in the pulling the A-B boundary close to the C-rich layer.

Another point of view is from the previous discussion about the competition between the entropy and energy effect. Their influences on the size of the microstructure have opposite trends; the entropy effect causes the Δ_A/Δ to expand, whereas the en-
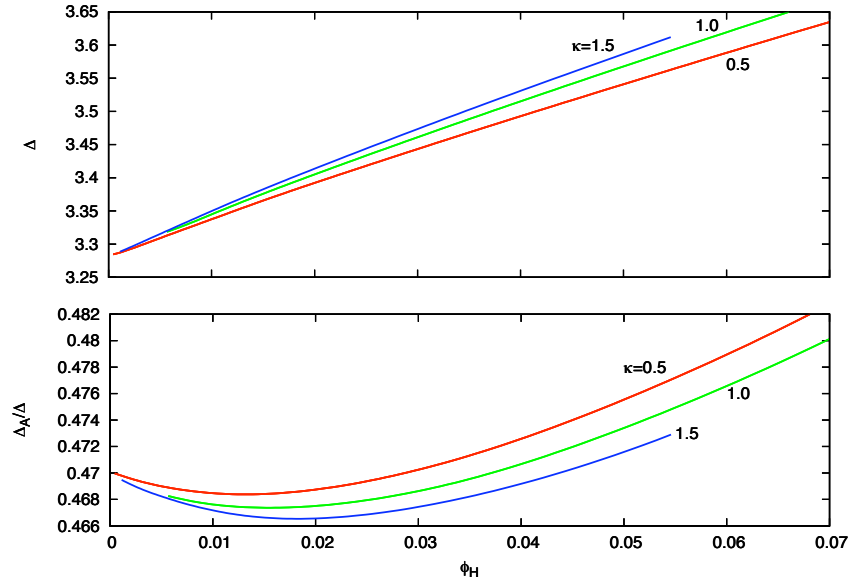
Figure 4.3: Spatial variables of LAM structure for AB/C blend with parameters $\chi_{AB}N = 11.0$, $\chi_{BC}N = 14.0$, $\chi_{AC}N = 0$ and $f_A = 0.46$. (a) Period of the LAM structure Δ, measured in unit of $R_g = Na^2/6$, as a function of the homopolymer concentration ϕ_H. (b) The relative size of A-rich region Δ_A, in unit of Δ, as a function of ϕ_H.
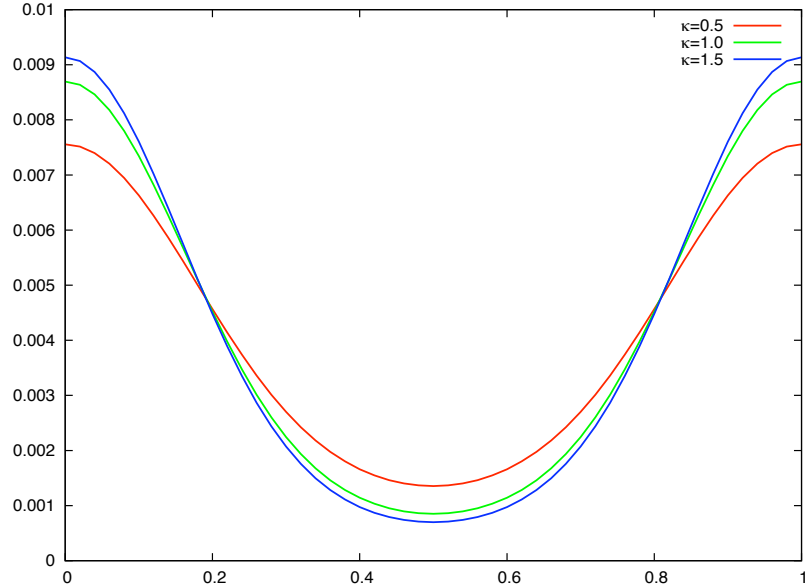
Figure 4.4: C-monomer density profile for AB/C blend with parameters $\chi_{AB}N = 11.0$, $\chi_{BC}N = 14.0$, $\chi_{AC}N = 0$, $f_A = 0.46$ and $\phi_H = 0.04$.

ergy effect tends to decrease Δ_A/Δ. When the homopolymer concentration is low, the energy effect outplays entropy effect, causing Δ_A/Δ to decrease. Longer homopolymers have a stronger energy effect so Δ_A/Δ has a sharper negative slope comparing to the short homopolymers. As we add more homopolymers, the entropy effect eventually prevails, and Δ_A/Δ starts to increase for all three lengths of homopolymers at high homopolymer concentration.

It is easier to demonstrate the effect of the homopolymer length by plotting the phase diagram in ϕ_H-κ axes. Figure 4.5 shows such a phase diagram for blends with parameters $\chi_{AB}N = 11.0$, $\chi_{BC}N = 14.0$, $\chi_{AC}N = 0$ and $f_A = 0.46$.

Figure 4.5: Phase diagram of AB/C blend with parameters $\chi_{AB}N = 11.0$, $\chi_{BC}N = 14.0$, $\chi_{AC}N = 0$ and $f_A = 0.46$. The results are plotted in ϕ_H-κ axes.

There are two regions of κ, each showing different phase behaviors. When $\kappa <$ 0.85, LAM phase is stable until relatively high concentration of homopolymer. The blend then macrophase separates into LAM-DIS coexisted phase. As $\kappa > 0.85$, the blend makes the transition from LAM to HEX at a small value of ϕ_H. Semenov

[44] had argued this scenario as long homopolymers clumping together to form the nucleus for the ordered structure. The blend then undergoes macrophase separation at a higher homopolymer concentration.

Figure 4.6: Phase diagram of AB/C blend with parameters $\chi_{AB}N = 11.0$, $\chi_{AC}N = 0$ and $\kappa = 1.0$. The results are plotted in ϕ_H-$\chi_{BC}N$ axes.

The length of the homopolymer is one of many factors which can influence the energy effect. Others include the three Flory-Huggins parameters and the A-monomer fraction of the diblock f_A. For the interaction parameters, it is the difference between $\chi_{AC}N$ and $\chi_{BC}N$ that matters. Figure 4.6 demonstrates this effect. While keeping $\chi_{AC}N$ constant, we vary $\chi_{BC}N$ from 13 to 15. There are also two ranges of $\chi_{BC}N$ with different phase behaviors, similar to Figure 4.5. This is understandable since in both scenarios, we are changing the interaction between B and C, either by varying the number of C monomers, or changing the Flory-Huggins parameter between B and C.

4.3 Case II: $f_A > 0.5$

For blends in which A-monomers are the majority component, we will focus on the transition bump at the LAM-HEX boundary, as shown in Fig. 4.1 near $f_A = 0.54$. We study the blends with parameters $\chi_{AB}N = 11.0$, $\chi_{BC}N = 12.0$, $\chi_{AC}N = 0$. Fig. 4.7 shows a partial phase diagram around $f_A = 0.54$ for three value of $\kappa = 0.5$, 1.0 and 1.5.
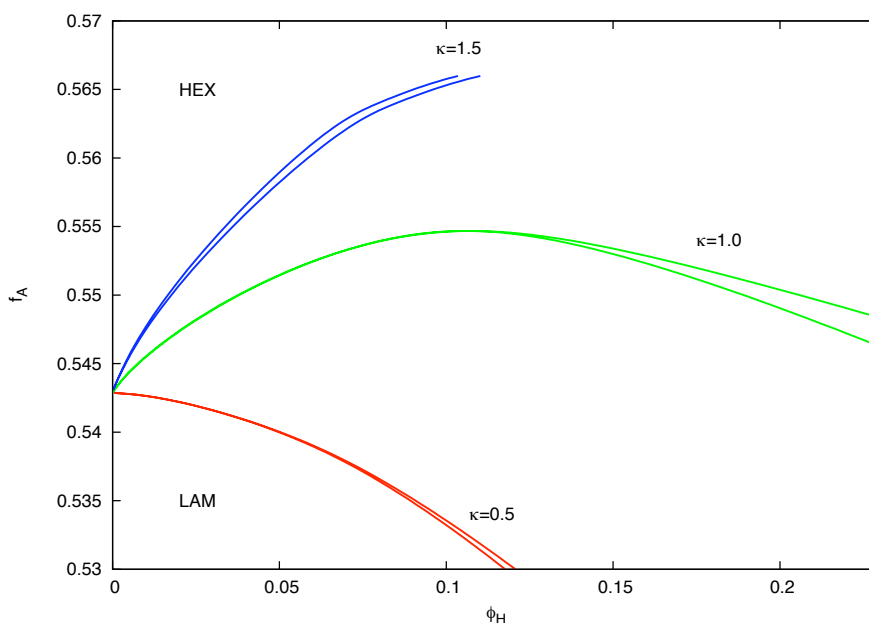
Figure 4.7: Phase diagram of AB/C blend with parameters $\chi_{AB}N = 11.0$, $\chi_{BC}N = 12.0$ and $\chi_{AC}N = 0$ for three different value of $\kappa = 0.5$, 1.0 and 1.5. The results are plotted in terms of ϕ_H and f_A.

Comparing Figure 4.7 and Figure 4.2, we notice that the bump feature in the phase transition lines for $f_A > 0.5$. For short homopolymer ($\kappa = 0.5$), the value of f_A at the LAM-HEX boundary decreases as the homopolymer concentration increases. As the homopolymer length becomes comparable to the copolymer, the slope of the phase boundary is positive initially, and becomes negative after certain value of ϕ_H. For $\kappa = 1.0$, this value is about 0.092. Longer homopolymer has even larger positive

slope, as shown in Fig. 4.7 for $\kappa = 1.5$, but there may not be a bump because the macrophase separation appears before the plunge of the transition line.

We again plot the phase diagram in ϕ_H-κ axes in order to apprehend the effect of the homopolymer length. Figure 4.8 shows such a phase diagram for the blend with parameters $\chi_{AB}N = 11.0$, $\chi_{BC}N = 12.0$, $\chi_{AC}N = 0$ and $f_A = 0.55$. The f_A is chosen to be right above the value of HEX-LAM transition ($f_A = 0.543$) for pure diblock copolymers.
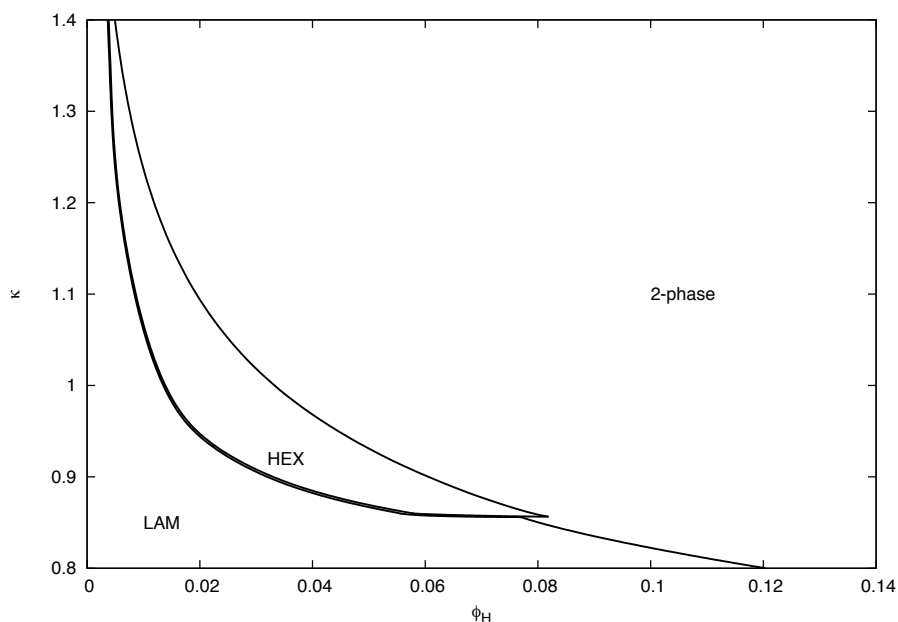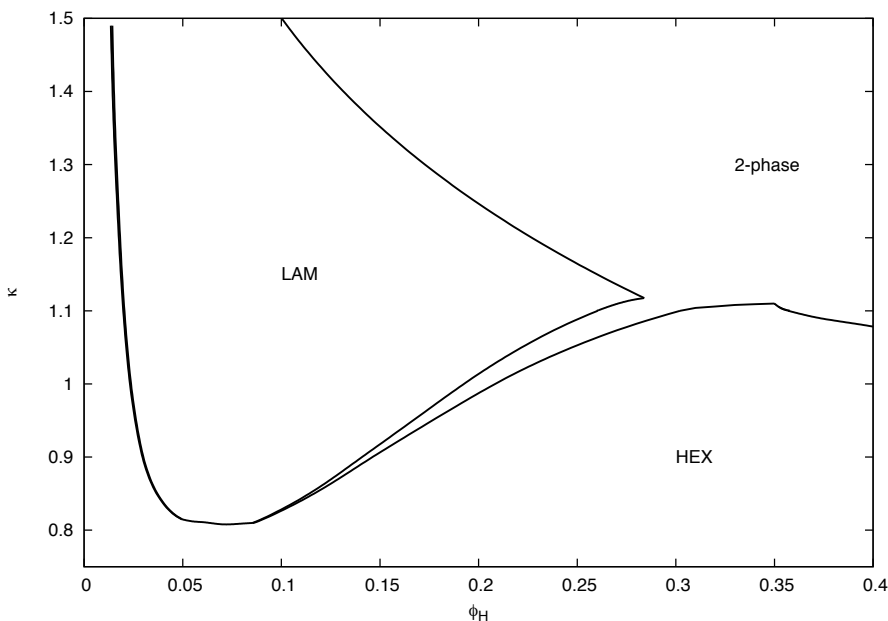

Figure 4.8: Phase diagram of AB/C blend with parameters $\chi_{AB}N = 11.0$, $\chi_{BC}N = 12.0$, $\chi_{AC}N = 0$ and $f_A = 0.55$. The results are plotted in terms of the homopolymer volume fraction ϕ_H and the relative length of the homopolymer κ.

There are three regions of κ, each showing different phase behaviors. When $\kappa < 0.8$, HEX phase is stable until relatively high concentration of homopolymer. The blend then macrophase separates into HEX-DIS coexisted phase. As $0.8 < \kappa < 1.1$, the blend makes the transition from HEX to LAM at a small value of ϕ_H and then reverses the transition at a higher concentration. When more homopolymers are added, the blend also undergoes macrophase separation. This is the region where the

bump appears in ϕ_H-f_A plots. As $\kappa > 1.1$, the blend keeps the lamellar phase after changing from HEX to LAM, and macrophase separates into LAM-DIS coexisted phase when ϕ_H is large.

The reversion of phase transition is a distinct feature for $f_A > 0.5$, in comparison with the phase diagram for $f_A < 0.5$ (Fig. 4.5). The difference is caused by the different value of ϕ_H at which the system undergoes macrophase transition. When small amount of homopolymers is added, the energy effect acts first and the blend makes a transition to decrease the space occupied by the A-rich domain. In the $f_A > 0.5$ case, the blend undergoes transition from HEX to LAM. When more homopolymer is added, there are two ways to distribute the extra homopolymers. One way is for the homopolymers to macrophase separated from the diblock copolymer, which accounts for the appearance of 2-phase region at higher ϕ_H. The other way is to increase the size of A-rich domain, if the entropy gain from increasing A-rich domain is more than enough to compensate both the entropy penalty of reducing the B-rich region and the energy effect. It is easier for blends with $f_A < 0.5$ to take this routine because the ϕ_H value for macrophase separation is low. As for $f_A > 0.5$, it takes large amount of homopolymer to reach the macrophase separation, so the second scenario happens for $f_A > 0.5$ as the blends reverse back to HEX phase as ϕ_H increases.

Figure 4.9 shows the effect of varying interaction parameter $\chi_{BC}N$ for the blend with parameters $\chi_{AB}N = 11.0$, $\chi_{AC}N = 0$ and $\kappa = 1.0$. There are also three ranges of $\chi_{BC}N$ with different phase behaviors, similar to Figure 4.8.

4.4 Summary

In this chapter, we constructed phase diagrams of AB/C blends using self-consistent field theory. Our study has focused on the asymmetric diblock copolymer, especially
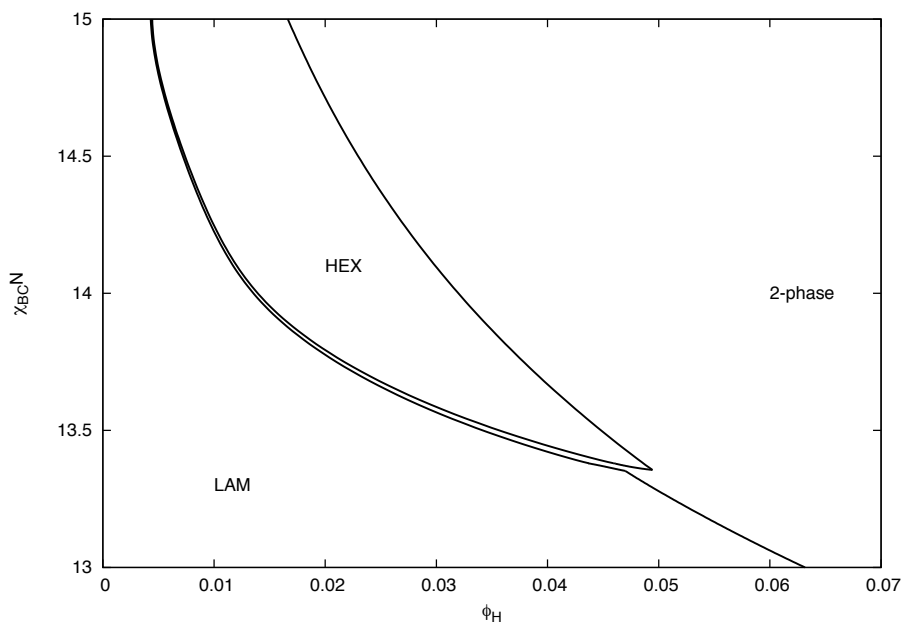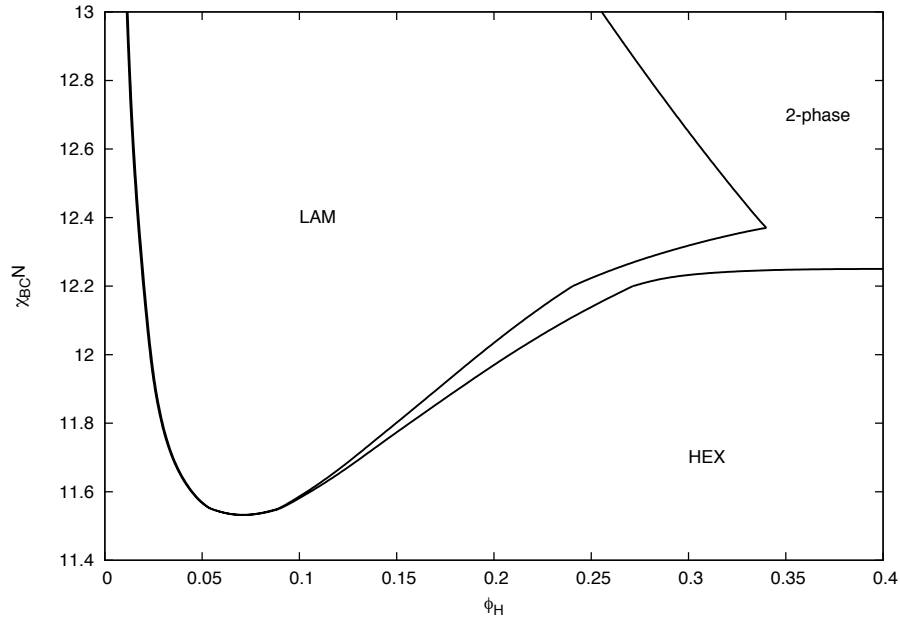
Figure 4.9: Phase diagram of AB/C blend with parameters $\chi_{AB}N = 11.0$, $\chi_{AC}N = 0$ and $\kappa = 1.0$. The results are plotted in terms of the homopolymer volume fraction ϕ_H and the interaction parameter $\chi_{BC}N$.

those close to the LAM-HEX boundary. The influences of the homopolymer concentration, the homopolymer chain length and the interaction parameters, on the phase behavior have been investigated. An interesting reversion of phase transition has been described for $f_A > 0.5$ case. In this study we only consider the classical phases, and more complex structure are expected to appear in a small region between the classical phases, but this should not change the qualitative picture of the phase transition sequence.

Chapter 5

AB/C Blends with Attractive Interaction

One feature of AB/C blends studied in the previous chapter is that there are large regions of macrophase separating in the phase diagram. From engineering point of view, sometimes this is undesirable because most applications rely on the homogeneous property of the material. Therefore, the interactions between the homopolymers and the diblock copolymers have to be controlled carefully.

The phase behavior of AB/C blends can be categorized into three cases, depending on the miscibility of C with respect to the AB diblock copolymers. If the homopolymer C is immiscible with both blocks A and B, the situation is simple: the homopolymers will be separated from diblock copolymers. A more complex case involves AB/C blends where the homopolymers C are immiscible with one block of the diblock copolymers, but interact favorable with the other block [50, 51, 52, 53, 54]. This system is similar to the case of amphiphilic molecules in solution, which is important to understand the self-assembly of surfactants and lipids. A simple example of this class of blends is that the homopolymers are chemically identical to one of the blocks of the copolymers, *i.e.*, an AB/A blend. Binary AB/A blends have been extensively studied theoretically [26, 44, 45, 46] and experimentally [47, 48, 49]. The phase diagrams of AB/A blends show the coexistence of macrophase separation and microphase separation, and the addition of the homopolymers tends to stabilize some complex ordered structures. The previous chapter was devoted to this case.

Another interesting case occurs for blends consisted of C homopolymers that are miscible with both the A and B blocks. The miscible nature of the blends may provide potential applications which rely on homogeneity of the material. Theoretically and practically, the extension to the attractive interactions between compounds may lead to new phenomena and create new materials. In general, miscible blends are characterized by homogeneous phases. However, phase separation can be induced by differential monomer-monomer interactions. An example is found in ternary blends composed of A/B/C homopolymers where all three binary pairs are miscible. A closed-loop immiscible region is found in the phase diagram [55, 56, 57, 58]. In cases that the attractive interaction between A/C is much stronger than that of B/C and A/B, A and C homopolymers tend to be separated from B. On the other hand, macroscopic phase separation of A and B cannot take place for AB/C blends, because A and B are chemically bonded together. Similar to the case of block copolymers, AB/C blends can reduce their free energy through microphase separation. Indeed, the microphase separation of AB/C blends has been observed in experiment of Chen *et al.* [28]. These authors investigated AB/C blends where the interactions between each pair of segments are favorable. Their experiments revealed a phase diagram with a closed microphase separation loop, despite the fact that the C homopolymers have attractive interactions with both blocks of the copolymers.

In this chapter, we present a theoretical study of the phase behavior of diblock copolymer/homopolymer blends. The study focuses on the case where the homopolymers attract to one block much more strongly than to the other block of the diblock copolymers. We use the Gaussian chain model for the polymers, and apply the random phase approximation (RPA) to examine the stability limits of the homogeneous phase, leading to both macrophase and microphase separation transition. While the RPA calculates the stability boundary of the homogeneous phase, we are also inter-

ested in the morphological details inside the microphase separation region. For this purpose, self-consistent field theory is employed. Various representative phase diagrams are constructed to illuminate the general trends in the phase behavior by varying the homopolymer length and monomer-monomer interaction parameters. Comparison with available experiments is given.

5.1 Random phase approximation

The random phase approximation analysis of a polymer blend [59, 17, 60, 61] starts with an external potential field u_α acting on the α monomer. Assuming that the external fields are small, the density response to the external potential, $\delta\phi_\alpha$, can be written in the Fourier space as a linear function of the external potential,

$$\delta\phi_\alpha(q) = -\frac{1}{k_B T} \sum_\beta \tilde{S}_{\alpha\beta}(q) u_\beta(q), \tag{5.1}$$

where $\tilde{S}_{\alpha\beta}(q)$ is the Fourier transform of the density-density correlation between α and β monomers. Here we have used the fact that functions depend on the wave vector $\mathbf{q}$ only through its magnitude $q \equiv |\mathbf{q}|$ because of the isotropic symmetry of a homogeneous phase.

The interaction between the monomers can be taken into account through the mean-field approximation. To this end, the effective potential acting on the α monomer is written in the form,

$$u_\alpha^{\mathrm{eff}}(q) = u_\alpha(q) + k_B T \sum_{\beta \neq \alpha} \chi_{\alpha\beta} \delta\phi_\beta + \eta, \tag{5.2}$$

where the second term accounts for the mean-field interaction between α and β monomers, and η is a potential required to assure the incompressible condition

$$\sum_\alpha \delta\phi_\alpha(q) = 0. \tag{5.3}$$

The random phase approximation assumes that the density response $\delta\phi_\alpha$ is given by the effective potential,

$$\delta\phi_\alpha(q) = -\frac{1}{k_B T}\sum_\beta S_{\alpha\beta}(q)u_\beta^{\text{eff}}(q), \tag{5.4}$$

where $S_{\alpha\beta}(q)$ is the Fourier transform of the density-density correlation when the external potential vanishes.

Equations (5.1)-(5.4) form a set of simultaneous equations for the unknowns $\delta\phi_\alpha$ and η. By solving these equations, the correlation functions $\tilde{S}_{\alpha\beta}$ can be found in terms of $S_{\alpha\beta}$ and $\chi_{\alpha\beta}$. The final results are [61]

$$\tilde{S}_{AA}(q) = \{\bar{S}_{AA}(q) - 2[W_3(q)/S_3(q)]\chi_{BC}\}/F(q) \tag{5.5}$$

$$\tilde{S}_{AB}(q) = \{\bar{S}_{AB}(q) - [W_3(q)/S_3(q)]$$
$$\times(\chi_{AB} - \chi_{BC} - \chi_{AC})\}/F(q) \tag{5.6}$$

$$\tilde{S}_{BB}(q) = \{\bar{S}_{BB}(q) - 2[W_3(q)/S_3(q)]\chi_{AC}\}/F(q) \tag{5.7}$$

where

$$\bar{S}_{\alpha\beta}(q) = S_{\alpha\beta}(q) - t_\alpha(q)t_\beta(q)/S_3(q), \tag{5.8}$$

$$t_\alpha(q) = \sum_\beta S_{\alpha\beta}(q), \tag{5.9}$$

$$S_3(q) = \sum_{\alpha,\beta} S_{\alpha\beta}(q), \tag{5.10}$$

$$W_3(q) = 2S_{AB}(q)S_{BC}(q)S_{AC}(q)$$
$$+S_{AA}(q)S_{BB}(q)S_{CC}(q) - S_{AA}(q)S_{BC}^2(q)$$
$$-S_{BB}(q)S_{AC}^2(q) - S_{CC}(q)S_{AB}^2(q), \tag{5.11}$$

$$F(q) = 2[\bar{S}_{AB}(q)\chi_{AB} + \bar{S}_{BC}(q)\chi_{BC} + \bar{S}_{AC}(q)\chi_{AC}]$$
$$+[W_3(q)/S_3(q)]\{2\chi_{AB}\chi_{BC} + 2\chi_{BC}\chi_{AC}$$
$$+2\chi_{AC}\chi_{AB} - \chi_{AB}^2 - \chi_{BC}^2 - \chi_{AC}^2 + 1\}, \tag{5.12}$$

Here we only express $\tilde{S}_{AA}$, $\tilde{S}_{AB}$ and $\tilde{S}_{BB}$ explicitly because the other $\tilde{S}_{\alpha\beta}$ can be written as combinations of these three due to the incompressibility and the symmetry of $\tilde{S}_{\alpha\beta} = \tilde{S}_{\beta\alpha}$.

The free energy of AB/C blends can be written as a Landau expansion about the homogeneous state in terms of the density fluctuations $\delta\phi_\alpha$,

$$
\begin{aligned}
\frac{F - F_{\mathrm{hom}}}{(\rho_0 V k_B T/N)} \quad &= \frac{1}{2!(2\pi)} \int \tilde{S}_{\alpha\beta}^{-1}(q)\delta\phi_\alpha(q)\delta\phi_\beta(-q)\mathrm{d}q + \cdots, \\
&= \frac{1}{2!(2\pi)} \int \lambda_k(q)|\delta\psi_k(q)|^2\mathrm{d}q + \cdots,
\end{aligned}
\tag{5.13}
$$

where $\tilde{S}_{\alpha\beta}^{-1}(q)$ is the inverse of the correlation function $\tilde{S}_{\alpha\beta}(q)$. Here we have neglected terms with order higher than two, and the second-order term can be further written in a quadratic form, where $\lambda_k(q)$ are eigenvalues of the matrix $\tilde{S}_{\alpha\beta}^{-1}(q)$. The stability of the homogeneous phase depends on the sign of eigenvalues $\lambda_k(q)$. When $\lambda_k(q) > 0$, the contribution of any fluctuations to the free energy is always positive, so the homogeneous phase is stable. When $\lambda_k(q) < 0$, the fluctuations reduce the free energy and the homogeneous phase is unstable.

Normally, the inverse of the correlation function $\tilde{S}_{\alpha\beta}^{-1}(q)$ is a 3×3 matrix for the AB/C blends. The incompressible condition reduces the order of the matrix by one. The spinodal line is determined by the condition that the smaller eigenvalue goes to zero. Typical plots of $\lambda_k(q)$ are shown in Fig. 5.1. In general, one of the eigenvalues $\lambda_1(q)$ is always positive, while the other one $\lambda_2(q)$ approaches zero when $\chi_{AC}N$ changes.

The macrophase separation is characterized by $\lambda_2(q) \to 0$ at $q = 0$. This is shown in Figure 5.1(a) for blends with $\kappa = 1.0$, $f_A = 0.8$, $\phi_H = 0.2$, $\chi_{AB}N = 15$, $\chi_{BC}N = 0$ and different $\chi_{AC}N$ values. The eigenvalue $\lambda_2(q)$ has a minimum at $q = 0$, and the minimum value approaches zero when $\chi_{AC}N$ increases. When $\lambda_2(q)$ becomes negative, any small density fluctuations with $q = 0$ decrease the free energy,

(a) Macrophase separation

(b) Microphase separation
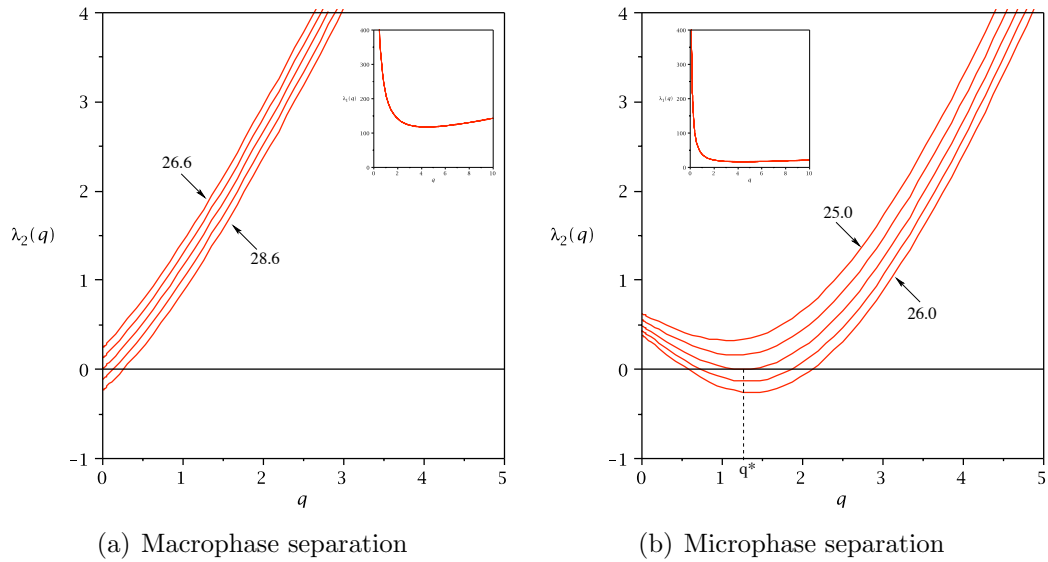
Figure 5.1: Plots of eigenvalues $\lambda_k(q)$ for (a) $\kappa = 1.0$, $f_A = 0.2$, $\phi_H = 0.8$, $\chi_{AB}N = 15$, $\chi_{BC}N = 0$ and a range of $\chi_{AC}N$ values ($26.6 \sim 28.6$), and (b) $\kappa = 1.0$, $f_A = 0.2$, $\phi_H = 0.2$, $\chi_{AB}N = 15$, $\chi_{BC}N = 0$ and a range of $\chi_{AC}N$ values ($25.0 \sim 26.0$). The insets show the positive eigenvalue $\lambda_1(q)$. Variations of $\lambda_2(q)$ with $\chi_{AC}N$ are shown, but they are not visible for $\lambda_1(q)$. The unit of the wave vector q is R_g^{-1}, where $R_g = \sqrt{Nb^2/6}$ is the radius of gyration.

leading to a growth of fluctuations with macroscopic wavelength. This corresponds to a macrophase separation between the diblock-rich phase and homopolymer-rich phase.

On the other hand, the diblock copolymers in the blend introduce the possibility of microphase separation. A microphase transition is characterised by the eigenvalue $\lambda_2(q) \to 0$ at some finite $q^* > 0$. This is shown in Figure 5.1(b) for blends with $\kappa = 1.0$, $f_A = 0.2$, $\phi_H = 0.2$, $\chi_{AB}N = 15$, $\chi_{BC}N = 0$ and different $\chi_{AC}N$ values. The Fourier mode with nonzero wave number q^* becomes unstable upon increasing $\chi_{AC}N$, leading to the formation of ordered structure with length scale of $(q^*/2\pi)^{-1}$. This is in contrast to Figure 5.1(a) where the Fourier mode $q = 0$ is destabilized first.

The six parameters $(\kappa, f_A, \phi_H, \chi_{AB}N, \chi_{BC}N, \chi_{AC}N)$ characterising the AB/C blends lead to a huge phase space. Some restrictions are needed so that the phase behavior can be described. We will keep $\kappa = 1.0$ for the RPA calculation, which means the homopolymer C has the same degree of polymerization as the diblock copolymer AB. Furthermore, we will assume $\chi_{BC}N = 0$, which represents the case where the A/C interaction is much stronger than the B/C interaction.

Fig. 5.2(a) shows a typical phase diagram in the ϕ_H-$\chi_{AC}N$ plane. The parameters are $f_A = 0.2$ and $\chi_{AB}N = 2$. The solid lines and dotted lines represent, respectively, the stability limits for the macrophase separation transition $(\chi_{AC}N)_{\text{macro}}$ and microphase separation transition $(\chi_{AC}N)_{\text{micro}}$.

The blends are disordered around $\chi_{AC}N = 0$ and $\phi_H = 1$, and ordered phases appear at both $\chi_{AC}N > 0$ and $\chi_{AC}N < 0$. In the region where $\chi_{AC}N > 0$, increasing $\chi_{AC}N$ induces an instability to either macrophase separation or microphase separation, depending on the blend composition and copolymer asymmetry. For blends with a minority of homopolymers, microphase separation occurs first when $\chi_{AC}N$ is
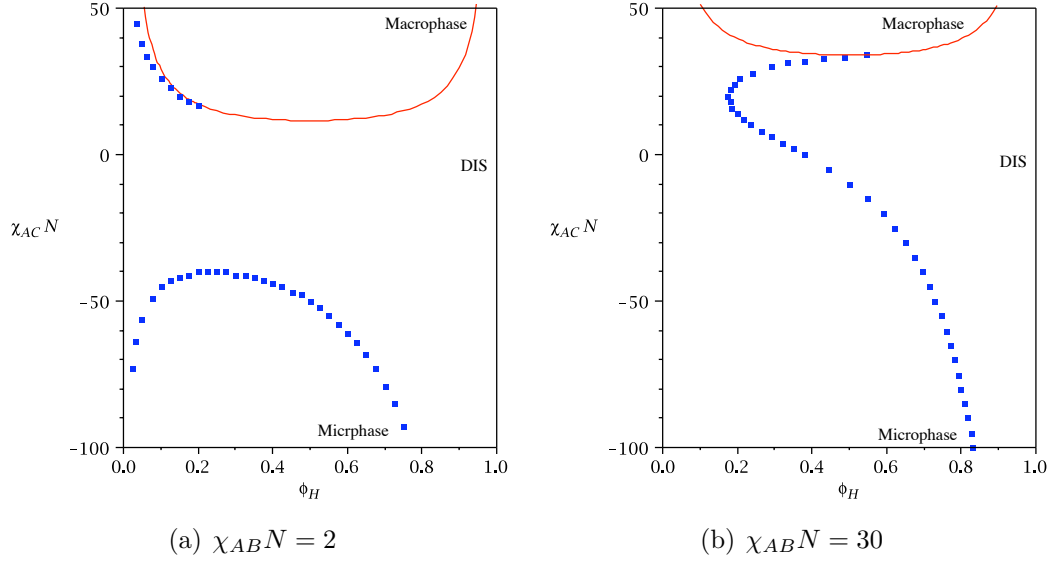
(a) $\chi_{AB}N = 2$ (b) $\chi_{AB}N = 30$

Figure 5.2: Phase diagrams for blends with parameters $\kappa = 1.0$, $f_A = 0.2$, $\chi_{BC}N = 0$ and (a) $\chi_{AB}N = 2$, (b) $\chi_{AB}N = 30$. The solid and dotted lines represent the stability limits for macrophase and microphase separation transition, respectively. Regions of macrophase separation, microphase separation and disordered states are labeled by Macrophase, Microphase and DIS.

increased. However, when the composition of the homopolymers increases to certain value, the blend undergoes macrophase separation when $\chi_{AC}N$ is increased. The critical composition for blends with $f_A = 0.2$ is $\phi_H \approx 0.2$. The shape of the stability lines also suggests that, for small ϕ_H value, both $(\chi_{AC}N)_{\mathrm{macro}}$ and $(\chi_{AC}N)_{\mathrm{micro}}$ decrease with increasing ϕ_H, while $(\chi_{AC}N)_{\mathrm{macro}}$ increases with increasing ϕ_H at large ϕ_H value. The former case suggests that the composition of the diblock copolymer in the blend suppresses the phase transition, which is known as the compatibilizing effect of the block polymers [62].

On the other hand, the microphase separation also occurs in the region where $\chi_{AC}N$ is negative. Since the interaction between the blocks $\chi_{AB}N = 2$, the pure diblock copolymers are in the disordered state. The stability line for the microphase separation approaches $\phi_H = 0$ axis infinitely close when $\chi_{AC}N$ has a large negative value. It is interesting that for a homogeneous diblock copolymer melt, adding a small

amount of homopolymers C which has a strong attractive interaction with one of the blocks will induce the phase separation. Upon increasing ϕ_H, $(\chi_{AC}N)_{\text{micro}}$ increases sharply at first, then decreases after $\phi_H \approx 0.25$.

A similar phase diagram for blends with $\chi_{AB}N = 30$ is shown in Fig. 5.2(b). In this case, the pure diblock copolymers are in the ordered state. This leads to the convergence of the two microphase separation regions at $\chi_{AC}N > 0$ and $\chi_{AC}N < 0$.

Another perspective to understand the phase transition is to plot the phase diagram in the ϕ_H-f_A plane for fixed interaction parameters. Fig. 5.3 shows phase diagrams for blends with $\chi_{AB}N = 2$ and different values of $\chi_{AC}N$. They can be viewed as cross-sections pictures of Fig. 5.2(a) at different values of $\chi_{AC}N$. At $\chi_{AC}N = 30$, because of the strong repelling interaction between A/C, a large region of macrophase separation exists, while a small region of microphase separation occurs near the $\phi_H = 0$ axis. As $\chi_{AC}N$ decreases, the macrophase separation region shrinks and eventually disappears at a negative value of $\chi_{AC}N$. At the same time, a closed-loop microphase separation region appears, as can be seen from Fig. 5.3(c) and 5.3(d). Qualitatively, this closed immiscible loop corresponds to the one observed in experiments [28].

The closed-loop microphase separated region emerges at large negative value of $\chi_{AC}N$, and also seems to expand with decreasing $\chi_{AC}N$. For a fixed copolymer asymmetry f_A, the lowest requirement of the homopolymer composition ϕ_{min} to reach the microphase transition is reduced when $\chi_{AC}N$ decreases. This can be shown in Figure 5.4, which plots the minimum value of ϕ_{min} to reach the close-loop as a function of $\chi_{AC}N$. When $\chi_{AC}N$ decreases, the close-loop of microphase separation appears at $\chi_{AC}N \approx -36$ for $\chi_{AB}N = 2$, and at $\chi_{AC}N \approx -44$ for $\chi_{AB}N = -2$. For the same $\chi_{AC}N$ value, the blend with a lower $\chi_{AB}N$ value requires more copolymer composition to reach the microphase transition.

(a) $\chi_{AC}N = 30$

(b) $\chi_{AC}N = 5$

(c) $\chi_{AC}N = -50$

(d) $\chi_{AC}N = -90$
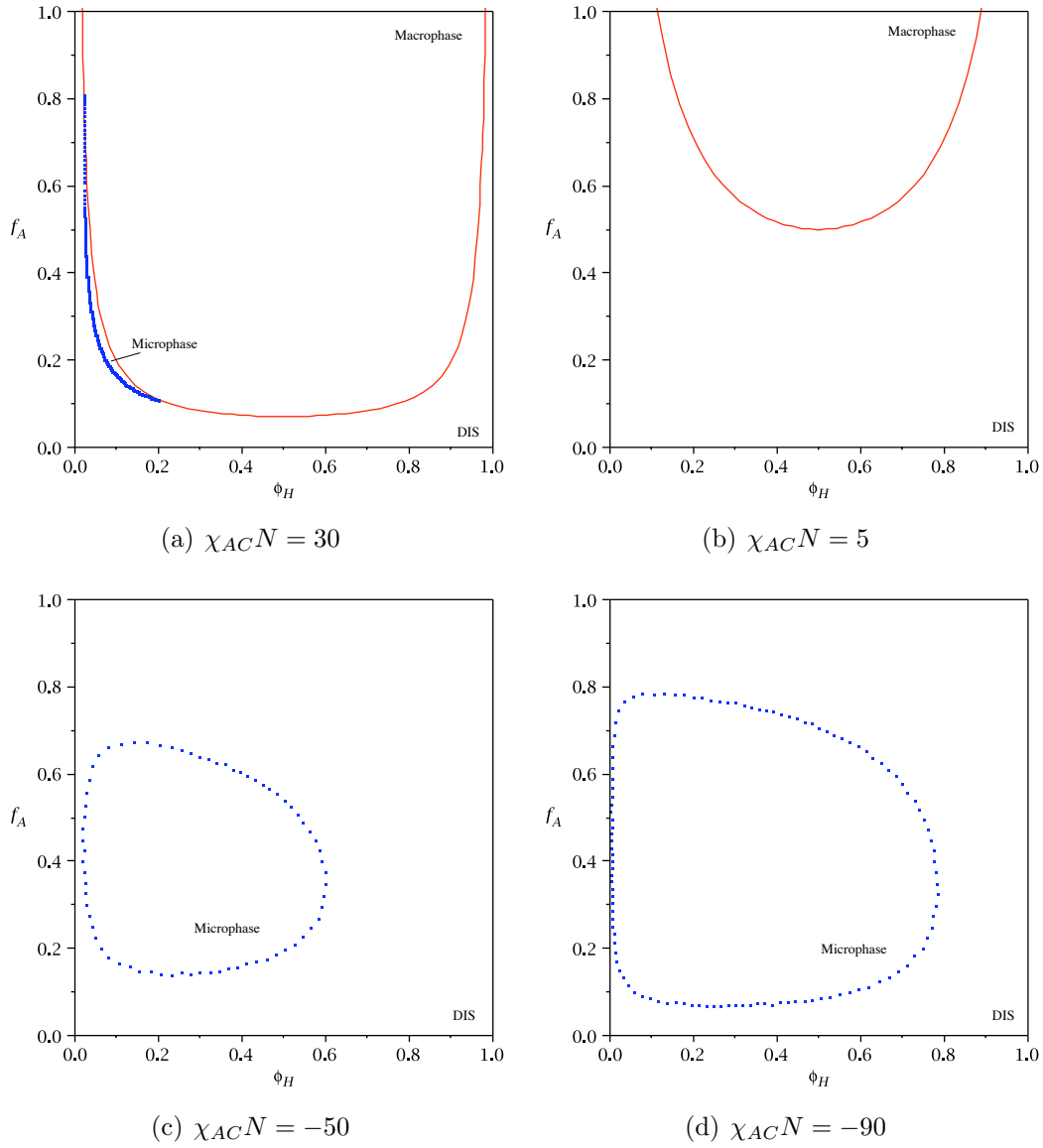
Figure 5.3: Phase diagrams for AB/C blends in ϕ_H-f_A plane. The parameters are $\kappa = 1.0$, $\chi_{AB}N = 2$ and $\chi_{BC}N = 0$. The solid and dotted lines represent the transitions for macrophase and microphase separation, respectively.
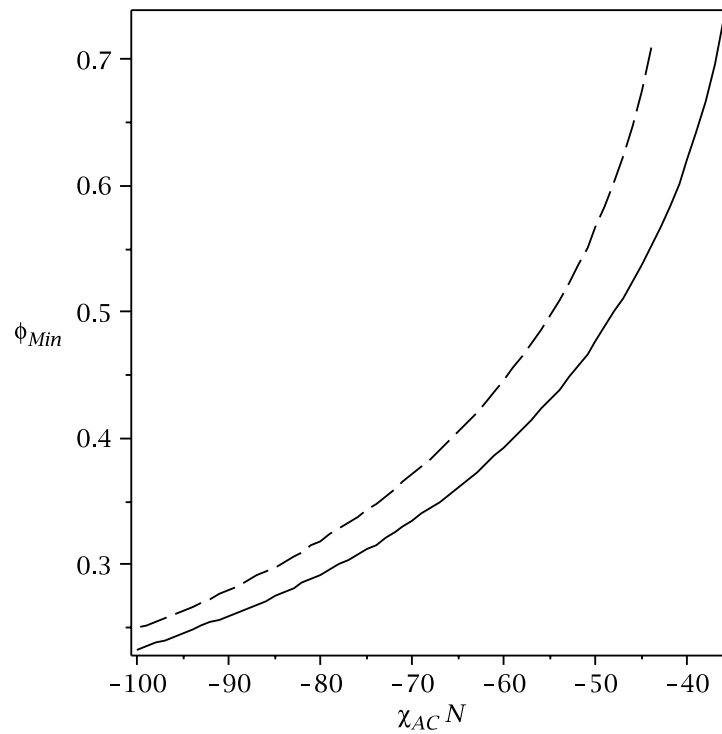
Figure 5.4: The minimum homopolymer composition $\phi_{\min}$ to reach the immiscible close-loop as a function of $\chi_{AC}N$. The parameters are $\alpha = 0.5$, $f = 0.5$ and $\chi_{BC}N = 0$. The solid and dashed lines present the case $\chi_{AB}N = 2$ and $\chi_{AB}N = -2$, respectively.

5.2 Self-consistent field theory

Because of its simplicity, random phase approximation provides a convenient method to calculate the order-disorder transition for various parameter sets, but it is difficult to apply RPA to the order-order transition. On the other hand, self-consistent field theory has been proved a powerful method to determine the microstructures of polymer blends [19, 22, 25, 26, 45, 46]. Therefore, it is desirable to apply self-consistent field theory to the study of the phase behavior of AB/C blends with attractive interactions.

Similar to previous chapter, we consider only the classical phases: lamellae (LAM), cylinders on a hexagonal lattice (HEX), and spheres on a body-centered cubic lattice (BCC). Complex structures, such as close-packed spheres, perforated lamellae and bi-continuous cubic phases, can also occur for certain parameters [26]. These non-classical phases were usually found in narrow regions between the classical phases. In this study, we are more interested in the evolution of the phase diagram by varying different parameters, therefore we restrict ourselves to the three classical phases.

Fig. 5.5(a) shows a phase diagram in the ϕ_H-f_A plane for blends with $\kappa = 1.0$, $\chi_{AB}N = 11$, $\chi_{BC}N = 0$ and $\chi_{AC}N = -30$. In this case, the value of $\chi_{AB}N$ is large enough so the diblock copolymer melt is in an ordered state. The results should converge to the pure diblock results as the homopolymer concentration goes to zero, which is the case as shown in Figure 5.5(a). The phase behavior shown in Figure 5.5(a) is typical for the case where the homopolymers attract strongly to one of the blocks ($\chi_{AC}N = -30$). This attractive interaction drives the C homopolymers to the A-domains, leading to larger regions of ordered phases for mediated homopolymer concentrations. For comparison, a phase diagram for the blends with $\kappa = 1.0$, $\chi_{AB}N = 11$, $\chi_{BC}N = 12$ and $\chi_{AC}N = 0$ is presented in Fig. 5.5(b) (from Chapter

4). Here the parameters are chosen in such a way that the C monomers accumulate inside the A-rich region for both cases.

These two phase diagrams display similar features when the homopolymer concentration is small. In this region, the majority of the blend is diblock copolymers and adding small amount of homopolymers should preserve the morphologies. When the homopolymer concentration becomes large, these two phase diagrams exhibit different phase behavior. For the case shown in Fig. 5.5(b), where the interaction parameter $\chi_{BC}N$ is positive, two possible scenarios of phase behavior appear. When f_A is large, only one disordered phase is stable. The blend tends to undergo unbinding transition where the spacing of the ordered structure increases and eventually diverges at certain homopolymer concentration [26, 45, 46]. When f_A is small, macroscopic phase separation becomes an option. Adding more homopolymers induces a macrophase separation transition, in which the blend separates into copolymer-rich and homopolymer-rich regions. On the other hand, for the case shown in Fig. 5.5(a), where $\chi_{AC}N$ has a large negative value, only one disordered phase is permitted. When the homopolymer concentration is large, the blends exhibit neither the unbinding transition nor the macrophase separation. This behavior is due to the strong attractive interaction between the A and C monomers. As the homopolymer concentration is increased close to unity, both cases reach a disordered phase.

When all three binary pairs are miscible, the AB/C blends exhibit another type of phase behavior. Fig. 5.6 shows a typical phase diagram for this case with $\kappa = 1.0$, $\chi_{AB}N = 2$, $\chi_{BC}N = 0$ and $\chi_{AC}N = -40$. In this case the blends are in a disordered phase at $\phi_H = 0$ and $\phi_H = 1$. Ordered phases occur in a closed-loop region, as indicated by the RPA analysis. Inside the closed-loop, different ordered structures are found. The order-order transitions between these structures are controlled largely by the homopolymer concentration ϕ_H.
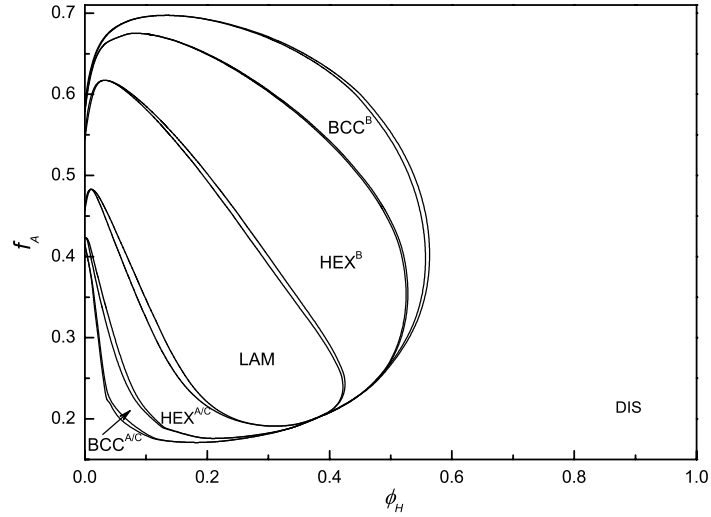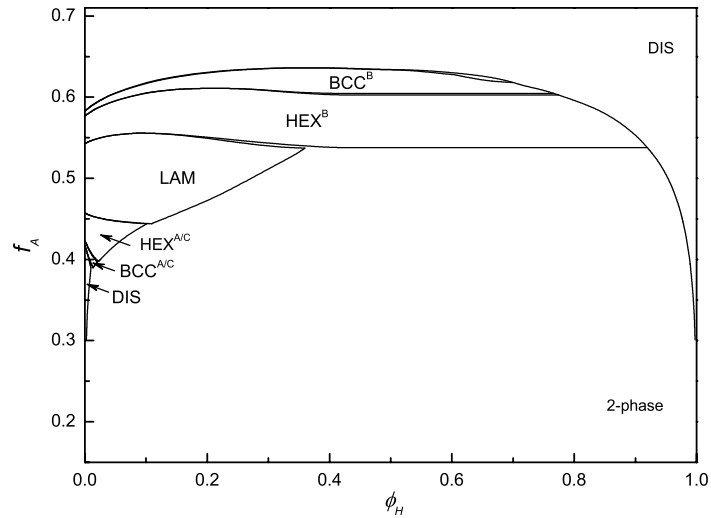
(a) $\chi_{AC}N = -30$

(b) $\chi_{AC}N = 12$

Figure 5.5: Phase diagrams of AB/C blends with parameters $\kappa = 1.0$, $\chi_{AB}N = 11$, $\chi_{BC}N = 0$, and (a) $\chi_{AC}N = -30$, (b) $\chi_{AC}N = 12$. The superscripts of HEX and BCC phase denote the components that form the cylinders and spheres near the lattice centers. There are regions of 2-phase coexistence between the ordered phases.
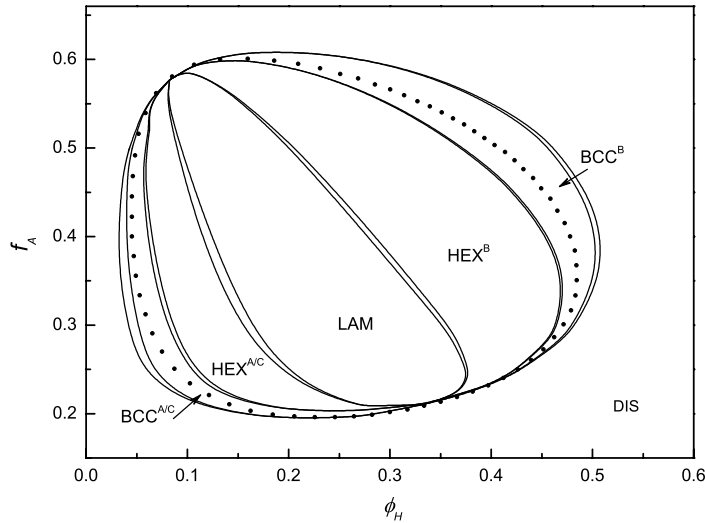
Figure 5.6: Phase diagram of AB/C blends with parameters $\kappa = 1.0$, $\chi_{AB}N = 2$, $\chi_{BC}N = 0$ and $\chi_{AC}N = -40$. The dotted line shows the RPA result.

There are two critical points at which all ordered phases converge on the order-disorder transition boundary. For the parameters used here, one point is located at $(\phi_H = 0.083, f_A = 0.58)$, and the other one at $(\phi_H = 0.33, f_A = 0.21)$. The order-disorder transition is a second-order transition at these two critical points, while the transition is first-order elsewhere. The nature of the order-disorder transition (ODT) can be understood by considering the third-order term in the free energy expansion. A first-order phase transition occurs when a non-zero third-order term is present. In the case of a phase transition from the disordered phase to the BCC phase, the third-order term does not vanish in general. Therefor a first-order ODT is expected. At the critical points, the ODT corresponds to a direct transition from the disordered phase to a lamellar phase. In this case the symmetry of the lamellar phase ensures the vanishing of the third-order term, resulting in a second-order ODT [63].

It is important to point out the limitation of the present theory. The mean-field approach used here approximates the fluctuating potential by a thermal averaged

potential. This assumption becomes inaccurate near the order-disorder transition, where the fluctuations are large. The fluctuations can shift the position of the phase boundary, and may change the second-order ODT into a weakly first-order transition [64, 65].

When the homopolymer concentration is increased, the AB/C blends change from a disordered phase to BCC, HEX and LAM phases. This sequence of phase transition can be understood by examining how homopolymers are distributed in the diblock melt. Since the interaction between A and B are at $\chi_{AB}N = 2$, which is well below the ODT value of 10.5 for symmetric diblocks, the pure diblock copolymers are in a disordered state. When small amount of homopolymers are added to the system, due to their strong attraction to A-blocks, the homopolymers are distributed around the A-blocks, resulting in an effective segregation of the A-B blocks. Ordered phases emerge when this effective segregation becomes strong enough. Another way to picture this effect is to take the homopolymers as the core-forming agents of micelles in a diblock copolymer melt. The appearance of the spherical phase as the homopolymers are added can be regarded as the ordering of these micelles. The key observation here is that the reduction of interaction energy from A-C segregation is sufficient to overcome the entropy loss. At the strong-segregation limit, a similar mechanism for the formation of reverse structures has been discussed by Semenov [44].

At higher homopolymer concentration, the volume of A/C domain increases. The packing requirement of larger A/C domains leads to a change of the interfaces between A/C and B, such that the interfaces are curved more towards the B-domain. This mechanism lead to order-order phase transitions from BCC to HEX, and then from HEX to LAM phases. After the LAM structure, adding more homopolymers induces the phase transition to HEX, and then to BCC, where the HEX and BCC both have

B-blocks as the central components. Eventually, a disordered phase is reached when sufficient amount of homopolymers are added.

In order to explore the effect of the A/C interactions, phase diagrams are constructed for different A/C interactions, either by changing the molecular-weight of C homopolymers or by changing the value of the Flory-Huggins parameter χ_{AC}. Fig. 5.7(a), 5.6 and 5.7(b) show the evolution of the phase diagrams with increasing κ ($\kappa = 0.5$, 1.0 and 1.5). Alternatively, the phase diagrams in Fig. 5.8(a), 5.6 and 5.8(b) demonstrate the progression as $\chi_{AC}N$ decreases ($\chi_{AC}N = -35, -40$ and -45) at fixed κ. It is obvious that the qualitative feature of the phase diagram stays the same in these phase diagrams. The main difference is the size of the closed-loop ordered phase region. Increasing the interaction will increase the area of the parameter space in which the blend is ordered.

Experimentally, several groups had studied blends with attractive interactions [28, 66]. In Ref. [28], Chen *et al.* studies the phase diagrams of PVPh-*b*-PMMA/PVP blends, where all three binary pairs, PVPh/PMMA, PMMA/PVP and PVP/PVPh, are miscible. Their setup closely resembles the blends studied in this work. They found a closed-loop microphase separation region surrounded by disordered phases. The three classical phases were also observed inside the closed-loop. The position of the closed-loop is similar to our theoretical prediction. Furthermore, the transition sequence of ordered phases from their experiments is consistent with our theoretical phase diagrams.

In a slightly different experiment setup [66], Tirumala *et al.* studied a triblock copolymer/homopolymer blend (PEO-PPO-PEO/PAA), where PAA interacts selectively to the end-block PEO. Upon increasing homopolymer concentration, they observed a phase sequence of disordered phase to lamellae, then to cylinders consisted
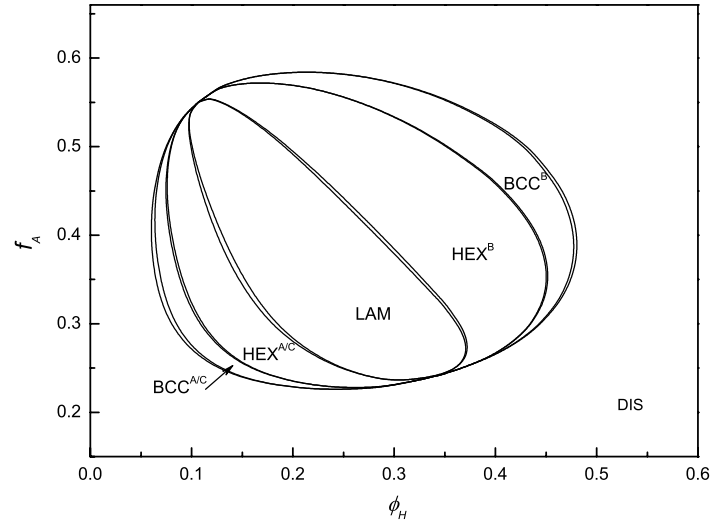
(a) $\kappa = 0.5$
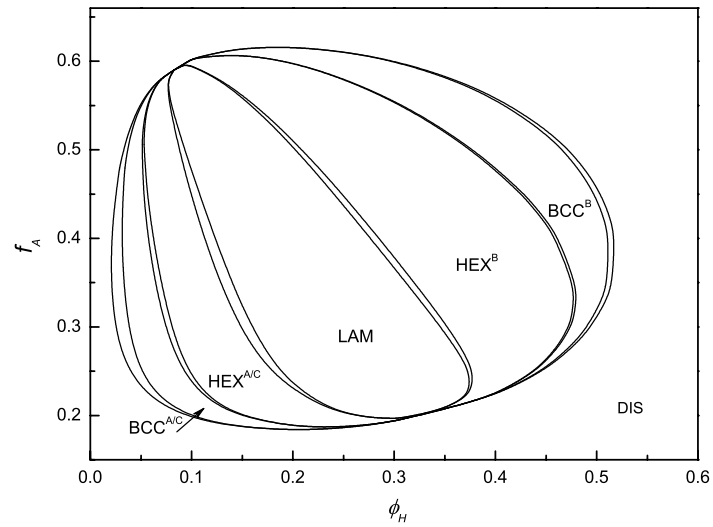
(b) $\kappa = 1.5$

Figure 5.7: Phase diagrams of AB/C blends with parameters $\chi_{AB}N = 2$, $\chi_{BC}N = 0$, $\chi_{AC}N = -40$ and (a) $\kappa = 0.5$, (b) $\kappa = 1.5$.
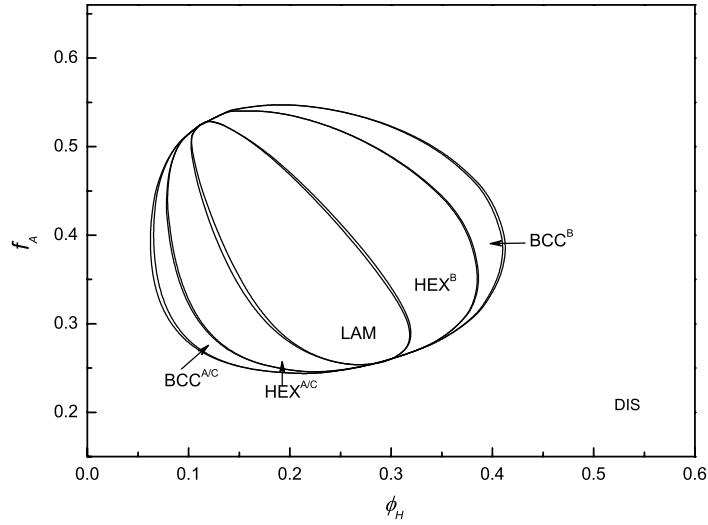
(a) $\chi_{AC}N = -35$
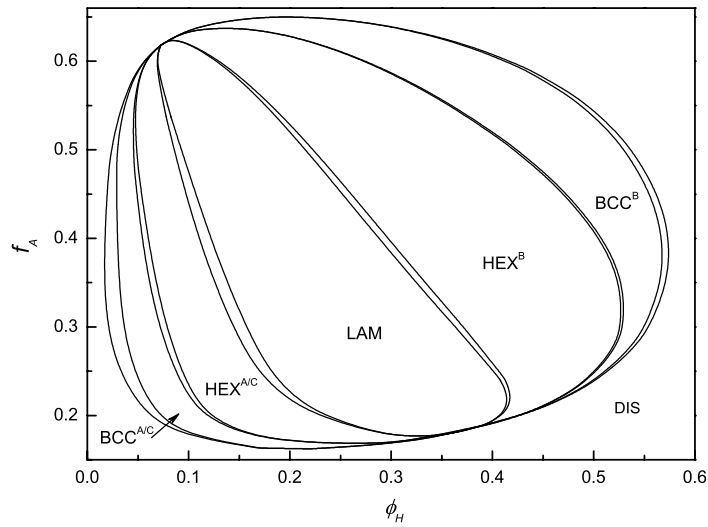
(b) $\chi_{AC}N = -45$

Figure 5.8: Phase diagrams of AB/C blends with parameters $\kappa = 1.0$, $\chi_{AB}N = 2$, $\chi_{BC}N = 0$, and (a) $\chi_{AC}N = -35$, (b) $\chi_{AC}N = -45$.

of PPO, then back to disordered phase. This transition sequence is again consistent with our theoretical predictions.

5.3 Summary

In this chapter, we have investigated the phase behavior of blends composed of AB diblock copolymers and C homopolymers. Two theoretical methods have been employed to construct the phase diagrams. By using the random phase approximation, the stability limits of the homogeneous phase are obtained. The phase diagrams are characterized by the coexistence of macrophase separation and microphase separation. When the interaction between A/C is repulsive, increasing $\chi_{AC}N$ will induce the transition from disordered phase to ordered phase, and the property of the transition depends on the homopolymer concentration. In general, blends with low homopolymer concentration tend to undergo microphase separation transition, whereas macrophase separation occurs at high homopolymer concentration. When the interaction parameter $\chi_{AC}N$ becomes attractive, the macrophase separation disappears while the microphase separation can still occur when the magnitude of $\chi_{AC}N$ is large. The microphase separation is caused by the strong attraction between the homopolymers to one of the blocks of the diblock copolymers. The difference between the A/C and B/C interactions leads to the spatial separation of B monomers from the A/C monomers, but the chemical connections between A and B prevent the macrophase separation. The microphase separation manifests itself in the ϕ_H-f_A phase diagram in a closed-loop region.

The detailed morphologies inside the closed-loop are calculated using self-consistent field theory. The RPA results provide a guidance to explore the parameter space. Three classical ordered phases (LAM, HEX and BCC) are included in the current

study. Along the closed-loop, the microphase separation transition is a first-order phase transition from disordered phase to the microphase with the symmetry of a body-centered cubic lattice except at two critical points. At these two points, the mean-field approach indicates that the blends undergo continuous phase transition from disordered phase to lamellar phase. When the homopolymer concentration is low, the phase sequence upon increasing homopolymer concentration is from BCC to HEX, and from HEX to LAM. At high homopolymer concentration, the phase sequence is reversed.

Another interesting observation of the phase diagram is the reverse morphology where the majority component of the diblock forms the dispersed domains of the ordered structure when small amount of homopolymers are added into the diblock melts. This phenomenon is due to the fact that the attractive interaction of A/C is much stronger than that of B/C.

The closed-loop microphase separation region has been observed in experiment [28], and our theoretical prediction is in qualitatively agreement with the experimental result. Phase diagrams for blends with different homopolymer lengths and Flory-Huggins parameters are also presented. It is observed that varying the interaction changes the size of the closed-loop, while the general features of the phase diagram are preserved.

Chapter 6

Bulk micelles

The linkages between the incompatible segments make the diblock copolymer an ideal model system to study the self-assembly. One interesting example is the micellization of diblock copolymers blended with homopolymers which are chemically identical to one of the blocks (AB/A blends). The covalent bonds between the incompatible blocks lead to the formation of aggregates. Similar phenomenon occurs for other amphiphilic molecules, such as the segregation of the surfactants in water and the bilayer formation of lipids. A good understanding of the micellization in diblock copolymer/homopolymer blends not only is important from the fundamental polymer physics point of view, it may also provide guidance to more complicated biological systems.

Consider a melt of A homopolymers and we gradually add diblock copolymers AB into the system. At very low copolymer concentration, the diblock copolymers stay as isolated chains in the homopolymer matrix, and the physical properties of the blend vary smoothly. As more copolymers are added, the B-blocks of the copolymers tend to cluster together in order to avoid the unfavored contact with the A homopolymers, thus forming micellar aggregates. The copolymer concentration at which the micelles start to emerge is called the critical micelle concentration (cmc) [67]. The physical properties of the blend also experience abrupt changes due to a sharp increase of the micelle number. Various micelle morphologies, including lamellar, cylindrical, and spherical micelles, can be obtained. The preferred morphology is decided by

several factors, such as the copolymer concentration, diblock asymmetry, the copolymer/homopolymer lengths, and the monomer-monomer interaction. Micelles formed by copolymers consist of a core of the B-blocks surrounded by a corona of the A-blocks. The corona may or may not be swollen by the A homopolymers. These aggregates typically have a characteristic size which is much larger than those of a single molecule, but they do not become macroscopic objects. This makes micelles suitable for potential medical applications, particularly in drug delivery [68].

A large number of theories and simulations have been developed over the years in order to model the micelle formation. Several authors have derived an analytic form of the total free energy as a function of the thermodynamic variables, such as the number of copolymers per micelle, the core and corona sizes. Leibler [69] studied the case of long homopolymer chains that do not penetrate into the corona of the micelle. Leibler considered spherical geometry, and the model was extended to cylindrical and lamellar micelles by Shull *et al.* [70]. On the other hand, when homopolymers have a length compatible to that of copolymers, they can swell the corona of the micelles. Leibler *et al.* [71] considered the formation of spherical micelles in this scenario, and later the theory was revised to study the transition between cylindrical and spherical micelles by Mayes *et al.* [72]. These methods clearly illustrate the fundamental physics of the micellization, but in order to make quantitative comparison with the experiments, more elaborate methods are required.

Self-consistent field theory is a powerful theoretical method to model polymer systems, and its molecular-level accuracy can provide detailed information about the micelle structure. Several researches have been conducted to the study of the micellization [73, 74, 75, 76, 77, 78, 79]. Duque [76] employed the theory with an additional constraint that permits the examination of intermediate structures. Chang *et al.* [77] used a pressure difference to stabilize the micelle. Greenall *et al.* [78, 79]

used a method of varying the size of simulation box. These studies have greatly enriched our understanding of the micelle formation. However, there still lacks a thorough investigation of the shape transition by changing various parameters.

In this chapter, we use self-consistent field theory to model an isolated micelle in dilute systems of diblock copolymers AB with homopolymers A. We consider three different micelle morphologies: lamellar, cylindrical and spherical. We focus on the shape transition of the micelle and the roles of the diblock asymmetry, the homopolymer length and the interaction parameter.

6.1 Isolated micelles

Here we introduce the notations for the binary blend of AB/A. Most of them are consistent with previous notations for AB/C blends.

The blend is composed of diblock copolymers with a chain length N, and homopolymers with a chain length κN in a volume of V. The copolymer has a fraction f_A of A-monomers, and $f_B (= 1 - f_A)$ of B-monomers. The volume fraction for A-monomer in the homopolymer, A- and B-monomer in the copolymer are ϕ_{hA}, ϕ_{cA} and ϕ_{cB}, respectively. The copolymer concentration is $\phi_c = \phi_{cA} + \phi_{cB}$. (This should not be confused with concentration of the C-monomer used before, but since we do not have a C component, here the subscript c stands for copolymer). We also assume the blend is incompressible and all monomers have the same volume ρ_0^{-1}. The monomer-monomer interaction is characterized by the standard Flory-Huggins parameter χ. We formulate the theory in the grand-canonical ensemble. The incompressibility permits the choice of setting the chemical potential for homopolymers to be zero, and the controlling parameter is the copolymer chemical potential μ_c, or equivalently, the activity $z_c \equiv \exp(\mu_c)/\kappa$.

The self-consistent field theory discussed in Chapter 2 can be easily implemented in planar, cylindrical and spherical geometry, with the purpose to model micelles of different morphologies. This simplifies the problem to be of one dimension, and the modified diffusion equations can be solved in real space using finite difference method. In our study, it is essential to calculate the free energy accurately. We have used a fine grid, with 200 space points per $\sqrt{N}a$ and 2000 points along the chain. It is also important to set the appropriate starting condition for the iteration, and we choose to set the micelle initially with a tanh density profile. In addition, we have checked the converged solution is independent of the starting radius.

Figure 6.1: Free energy difference ΔG between a cylindrical micelle and the homogeneous phase, plotted as a function of copolymer chemical potential μ_c. The blends have the parameters $f_A = 0.60$, $\kappa = 1.0$ and $\chi N = 20$.

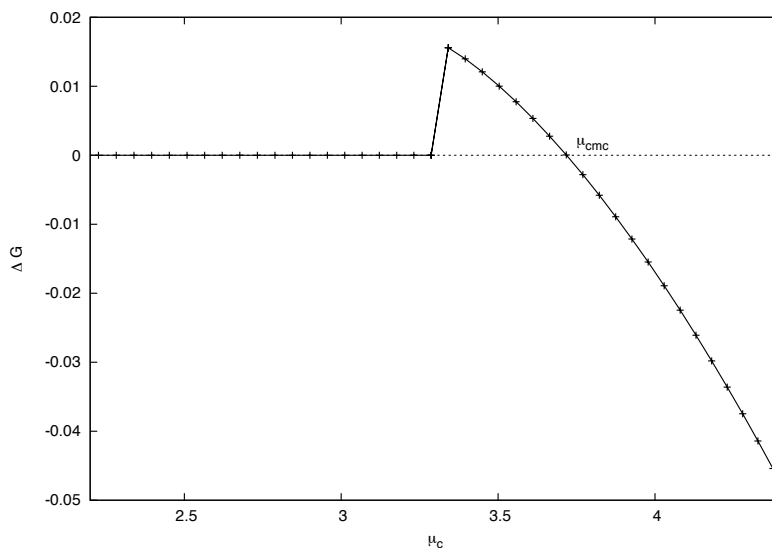The stability of the micelle is determined by its free energy with respect to the homogeneous phase. Fig. 6.1 shows ΔG, the free energy difference between a cylindrical micelle and the homogeneous phase, plotted as a function of copolymer chemical potential μ_c. The parameters for the blends are $f_A = 0.60$, $\kappa = 1.0$ and $\chi N = 20$. When μ_c is small, corresponding to the small copolymer concentration, ΔG remains

around zero. When μ_c approaches μ_{cmc} from below, ΔG increases slightly, and then becomes negative when μ_c is greater than μ_{cmc}. Here we define cmc as the copolymer concentration of the bulk when the excess free energy becomes negative. By using this definition, we have neglected the translational entropy of the micelles. Since we are mostly concerned with the blends of small copolymer concentrations, the density of micelles is small and the interactions between micelles are negligible. Once the μ_{cmc} is found, the critical micelle concentration can be calculated from the bulk relation,

$$\frac{\mu_c}{\kappa} = \frac{\ln \phi_c}{\kappa} - \ln(1 - \phi_c) + f_B \chi N (1 - 2 f_B \phi_c) \tag{6.1}$$
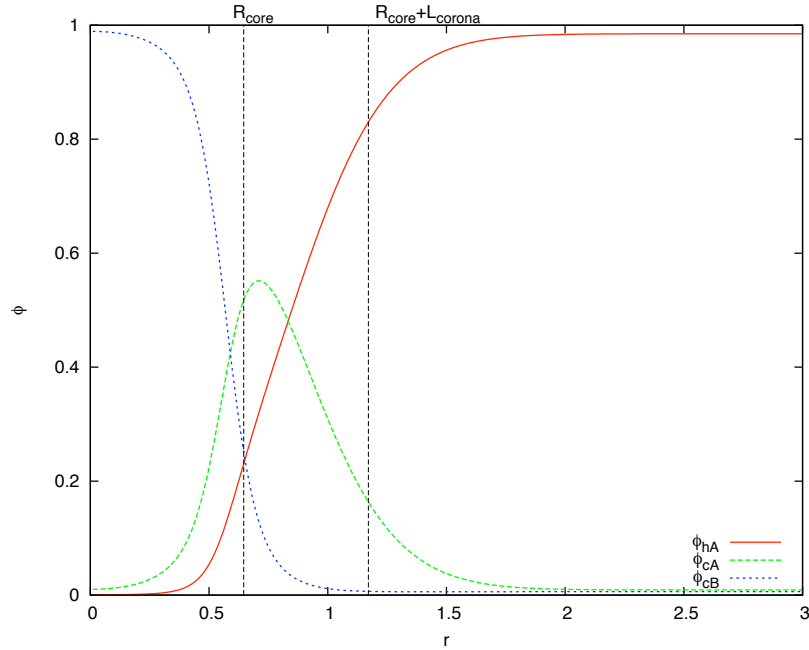
Figure 6.2: Density profiles for an isolate cylindrical micelle. The blend has the parameters $f_A = 0.60$, $\kappa = 1.0$, $\chi N = 20$ and $\mu_c = 3.87$.

One of the advantages of self-consistent field method is that detailed density profiles can be obtained for the isolated micelle. Fig. 6.2 shows the density profiles for the same blend in Fig. 6.1 with $\mu_c = 3.87$. With this knowledge, we are able to compute the geometrical variables of the micelle, such as the core and corona sizes, and the material properties of the micelle, such as the number of copolymer/homopolymer

within the micelle. For the core radius, a simple definition would be the point where $\phi_{cA}(r) = \phi_{cB}(r)$. However, this definition breaks down in the weak segregation region when sufficient amount of homopolymers are present inside the core. We opt to first calculate the radius of gyration of the core. For spherical micelles, it has a form

$$R^2_{\mathrm{g,core}} = \frac{\int r^2(\phi_{cB}(r) - \phi^b_{cB})\mathrm{d}V}{\int (\phi_{cB}(r) - \phi^b_{cB})\mathrm{d}V}, \tag{6.2}$$

where ϕ^b_{cB} is the B-block concentration of copolymers in the bulk phase which has to be removed to isolate the core. The core radius then can be computed from $R_{\mathrm{g,core}}$,

$$R^2_{\mathrm{g,core}} = \frac{3}{5}R^2_{\mathrm{core}}. \tag{6.3}$$

Following a similar procedure, we can compute the radius of gyration of the corona,

$$R^2_{\mathrm{g,corona}} = \frac{\int r^2(\phi_{cA}(r) - \phi^b_{cA})\mathrm{d}V}{\int (\phi_{cA}(r) - \phi^b_{cA})\mathrm{d}V}, \tag{6.4}$$

where ϕ^b_{cA} is the A-block concentration of copolymers in bulk. The corona thickness is related to $R_{\mathrm{g,corona}}$ by

$$R^2_{\mathrm{g,corona}} = \frac{3}{5}\frac{(R_{\mathrm{core}} + L_{\mathrm{corona}})^5 - R^5_{\mathrm{core}}}{(R_{\mathrm{core}} + L_{\mathrm{corona}})^3 - R^3_{\mathrm{core}}}. \tag{6.5}$$

For lamellar and cylindrical micelles, similar forms can be obtained.

In order to better understand the material distribution inside the micelle, we define two more variables for the micelle. The first one is the excess copolymers, defined as

$$\Omega = \frac{1}{V_{\mathrm{micelle}}} \int_0^{R_{\mathrm{micelle}}} (\phi_c(r) - \phi^b_c)\mathrm{d}V, \tag{6.6}$$

where $R_{\mathrm{micelle}} = R_{\mathrm{core}} + L_{\mathrm{corona}}$ and ϕ^b_c is the copolymer concentration in bulk. This variable characterizes the number of copolymers that are segregated. The second one is the penetrating homopolymer which has a form

$$\Theta = \frac{1}{V_{\mathrm{micelle}}} \int_0^{R_{\mathrm{micelle}}} \phi_{hA}(r)\mathrm{d}V. \tag{6.7}$$

This variable describes the number of homopolymers which penetrate inside the micelles, which is a good indication for the degree of swelling.

6.2 Results and Discussions

In general, the critical micelle concentration for certain morphology is a function of the diblock asymmetry f_A, the homopolymer/copolymer length ratio κ, and the interaction parameter χN. The cmc for different morphologies can be obtained from self-consistent field theory, and the preferred micelle geometry is the one with the lowest cmc. Since the chemical potential is a monotonic function of the copolymer concentration in dilution solution, the same result can be obtained by comparing the copolymer chemical potential.

We begin by examining the dependence of f_A, while keeping κ and χN constant. Before we present our results, it is intuitive to repeat the results from the scaling theory [70] for comparison. In Fig. 6.3, the value of $\mu_{\mathrm{cmc}}/(\chi N)^{1/3}$ for different geometries are plotted as functions of copolymer asymmetry f_A. The micelle geometry is expected to be lamellar for $f_A < 0.65$, cylindrical for $0.65 < f_A < 0.87$, and spherical for $f_A > 0.87$. Also, the value of f_A at which the shape transition occurs is independent of χN, due to the coincidence that μ_{cmc} for different geometries have the same prefactor $(\chi N)^{1/3}$.

In the inset of Fig. 6.4, the critical micelle concentrations are plotted as a function of f_A for blends with $\kappa = 1.0$ and $\chi N = 20$. The curves for different geometries are close to each other and it is difficult to distinguish them, but the trend of increasing cmc as f_A is increased can be seen. When f_A is increased while the total length of the copolymer kept constant, the length of B-block is reduced, which effectively reduces the incompatibility between copolymers and homopolymers. At the same time, the
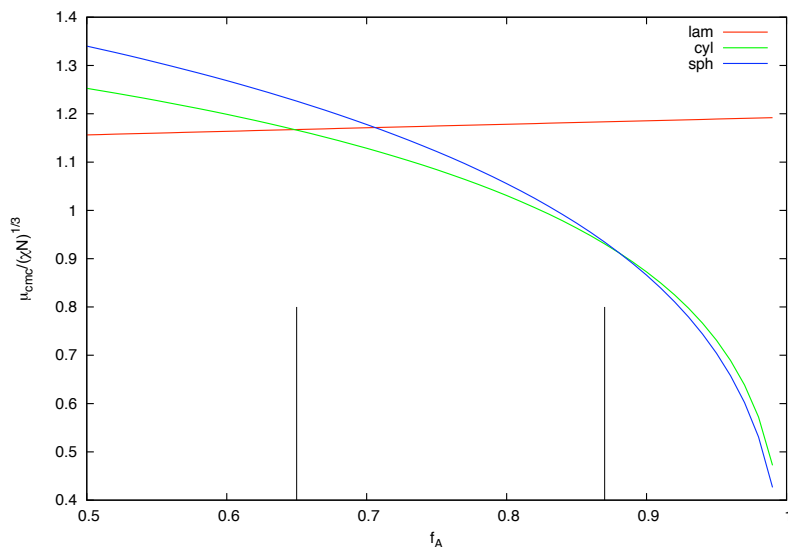
Figure 6.3: Dependence of μ_{cmc} on the copolymer asymmetry f_A as derived from the scaling method. Three morphologies are plotted: lamellar (blue solid line), cylindrical (green, dashed line) and spherical (red dotted line).

length of A-block is increased, which improves the solubility of the copolymers in the homopolymers. Thus a higher copolymer concentration is required for the micelles to form.

The shape transition can be more clearly seen from the chemical potential plot, as shown in Fig. 6.4. μ_{cmc} is a decreasing function of f_A for cylindrical and spherical micelles, except when the copolymer becomes very asymmetric. The μ_{cmc} for bilayers also has a small negative slope, in contrast to the scaling theory. For more symmetric copolymers, the chemical potential is much lower for the lamellar micelles than for the cylindrical and spherical micelles, indicating the bilayer structure is favored. As f_A increases, μ_{cmc} decreases. The slopes of the decrease are different for different geometries, as the curve for spherical micelles decreases most sharply, and that for the lamellar is more flat. The comparison between μ_{cmc} indicates a trend of shape transition: lamellar $\rightarrow$ cylindrical $\rightarrow$ spherical. This tendency can be explained by a simple geometrical argument; as f_A increases, the ratio between the volume of the
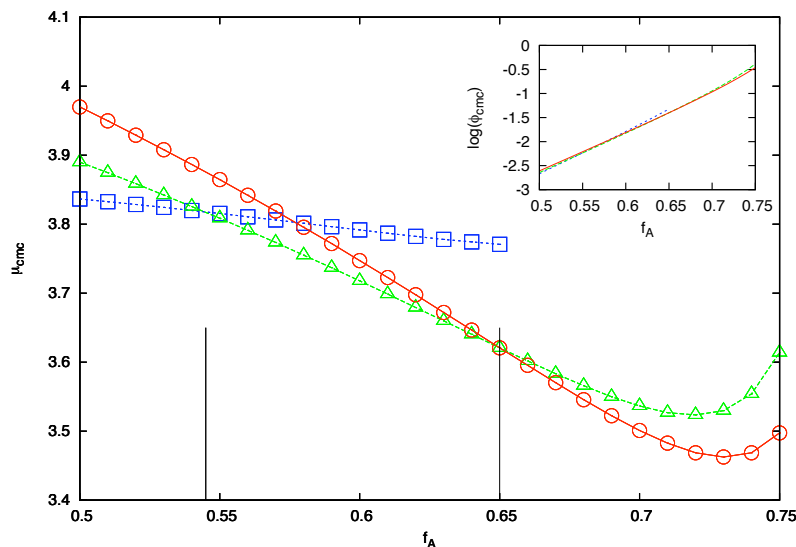
Figure 6.4: Dependence of μ_{cmc} on the copolymer asymmetry f_A for blends with $\chi N = 20$ and $\kappa = 1.0$. The critical micelle concentrations are plotted in the inset. Notation as in Fig. 6.3.

corona (A-block) and core (B-block) becomes larger, causing the interfaces between the A/B blocks to curve more towards the core. For $\kappa = 1.0$ and $\chi N_c = 20$, shape transitions happen at $f_A = 0.54$ and $f_A = 0.65$.

In Fig. 6.5, plots similar to those in Fig. 6.4 are shown except the length ratio of homopolymer/copolymer is changed to $\kappa = 2.0$. In contrast to the scaling results, the transition points move towards more asymmetric copolymers. In this case, they are at $f_A = 0.59$ and $f_A = 0.70$.

In Fig. 6.6, we increase the incompatibility between A/B monomers, $\chi N = 50$, while keeping the homopolymer length the same. The change of χN_c has a pronounced effect on cmc (notice the difference in y-scale of Fig. 6.4 and 6.6 insets). Similar to Fig. 6.5, the transition points also shift to more asymmetric copolymers.

The shape transition of the micelle can also be induced by varying the homopolymer molecular weight. We choose to study the blends with $f_A = 0.70$ and $\chi N = 20$. For such an asymmetric diblock copolymer, the lamellar structure is unstable, so only

Figure 6.5: Dependence of μ_{cmc} and ϕ_{cmc} on the copolymer asymmetry f_A for blends with $\chi N = 20$ and $\kappa = 2.0$. Notation as in Fig. 6.3.

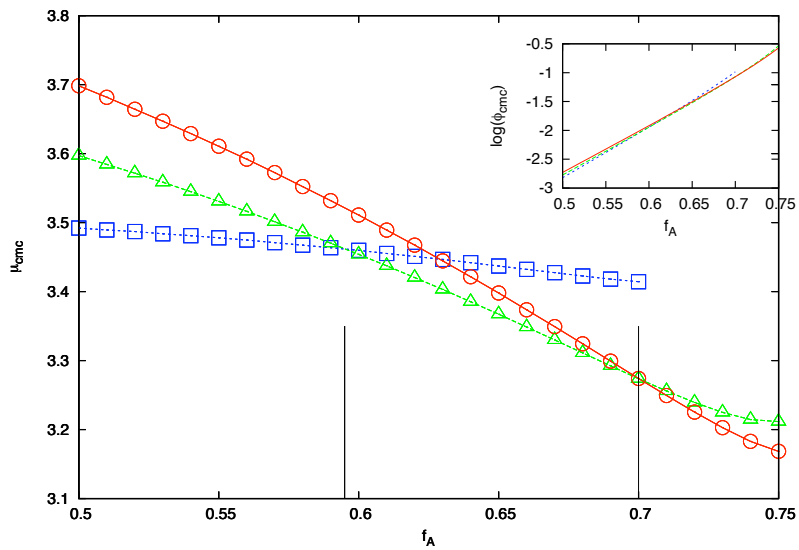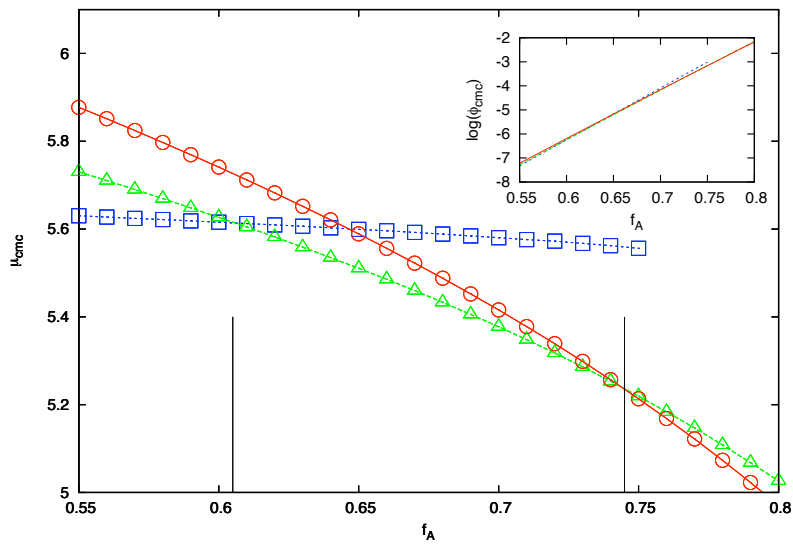Figure 6.6: Dependence of μ_{cmc} and ϕ_{cmc} on the copolymer asymmetry f_A for blends with $\chi N = 50$ and $\kappa = 1.0$. Notation as in Fig. 6.3.

cylindrical and spherical micelles are considered. In Fig. 6.7, the critical micelle concentrations are plotted as functions of κ. Since the difference in cmc between different homopolymer lengths is considerably larger than those between different shapes for a given homopolymer length, we also plot the difference of cmc in the inset to demonstrate the transition point more clearly. The micelle undergoes the transition from spherical to cylindrical at around $\kappa = 2.0$.

To better understand the mechanism of the shape transition, we plot the micelle core radius, the corona thickness, the excess copolymers and the penetrating homopolymers in the micelle. In Fig. 6.8(a), the radius of the core consisted mostly of B-blocks of the copolymers are shown as a function of κ. The copolymer chain configurations in the core are notably different for the two geometries. In the core of the cylindrical micelles, the B chains are only slightly extended from their Gaussian configuration (the unperturbed rms end-to-end distance for the B-block with $f_B = 0.3$ is $0.22\sqrt{N}a$). When the homopolymer length is increased, the B chains are stretched further, but in a more slow manner. This is because more copolymers are segregated into the micelle, as shown in Fig. 6.8(c). This effect counters the increase of core radius and provides some release for the B chains. For the spherical micelle, similar trends of the core radius and excess copolymers are found, but comparing to the cylindrical micelles, B-blocks are severely elongated in the spherical micelle.

The corona of the micelle consists of mostly A-blocks of the copolymer, swollen by A homopolymers. The corona thickness is shown in Fig. 6.8(b). Although the corona thickness appears to be much larger than the length of the unperturbed A-block $(0.34\sqrt{N}a)$, the A-blocks are not strongly stretched due to the presence of A homopolymers. The difference between the two morphologies lies in the degree of swelling, as shown in Fig. 6.8(d). The cylindrical micelle has more homopolymers penetrating into the corona than the spherical micelle. Those homopolymers can help

91
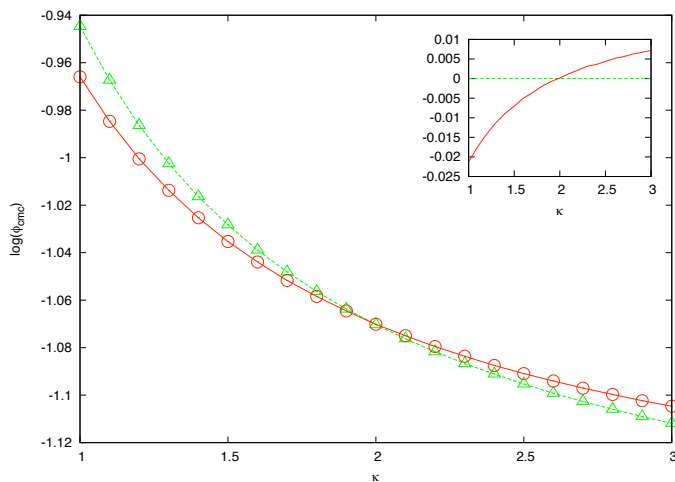
Figure 6.7: Dependence of ϕ_{cmc} on the homopolymer/copolymer length ratio κ for blends with $\chi N = 20$ and $f_A = 0.70$. Two morphologies are plotted: cylindrical (green, dashed line) and spherical (red dotted line). The difference in the cmc of the two morphologies is plotted in the inset for clarity.

Figure 6.8: Micelle properties as a function of κ for blends with $\chi N = 20$ and $f_A = 0.70$. The core radius (a), the corona thickness (b), the excess copolymers (c) and the penetrating homopolymers (d) are plotted. Notation as in Fig. 6.7.

92

to relax the A-blocks in the corona. When κ is increased, the size of the homopolymers becomes bigger comparing to the micelle, and it is more difficult for the homopolymers to penetrate inside the corona. Therefore, the corona length decreases as κ increases.

The deformation of the polymer chain in both the core and the corona are remarkably different for the two geometries. Comparing the spherical micelle, the B-blocks in the core of cylindrical micelle are less stretched, and the A-blocks in the corona is more relaxed. This contrast results in a shape transition from spherical micelle to cylindrical micelle as the homopolymer length is increased, as demonstrated in Fig. 6.7. Similar effect has been discussed in Ref. [72] for the case $\kappa < 1$.

Change in the micelle morphology can also take place by varying the interaction parameter χN. We consider blends with parameters $f_A = 0.7$ and $\kappa = 1.0$. The critical micelle concentrations and some properties of the micelle are plotted in Fig. 6.9 and 6.10. A change of morphology from spherical to cylindrical micelle is exhibited when the χN is increased, similar to the case when κ is increased. However, there are some notable differences. First, the cmc changes more rapidly by varying χN. The value of cmc is reduced by two orders of magnitude when χN changes from 20 to 40, while the cmc has the same order when κ changes from 1 to 2. Varying the homopolymer length is to change the surrounding of the micelle, while changing the interaction parameter directly alters the incompatibility between the A/B blocks of the copolymers, so latter has a much profound effect on the cmc. Second, as shown in Fig. 6.10(b), there appears to be a minimum in the corona thickness when χN is increased. At the weak segregation region when χN is small, the corona is strongly swollen by the A homopolymers. As χN increases, the repelling between A and B monomers pushes A homopolymers away from the corona, subsequently reducing the corona thickness. As χN becomes larger and reaches the strong segregation region, the interfacial energy becomes important. Both the A/B blocks of copolymers have
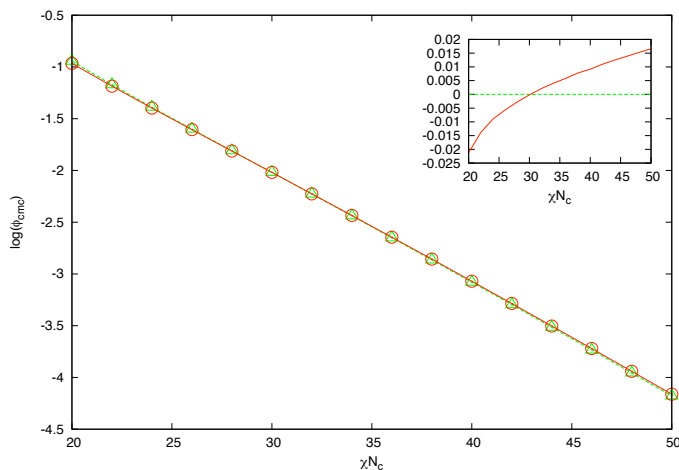
Figure 6.9: Dependence of ϕ_{cmc} on the interaction parameter χN for blends with $\kappa = 1.0$ and $f_A = 0.70$. Two morphologies are plotted: cylindrical (green, dashed line) and spherical (red dotted line). The difference in the cmc of the two morphologies is plotted in the inset for clarity.
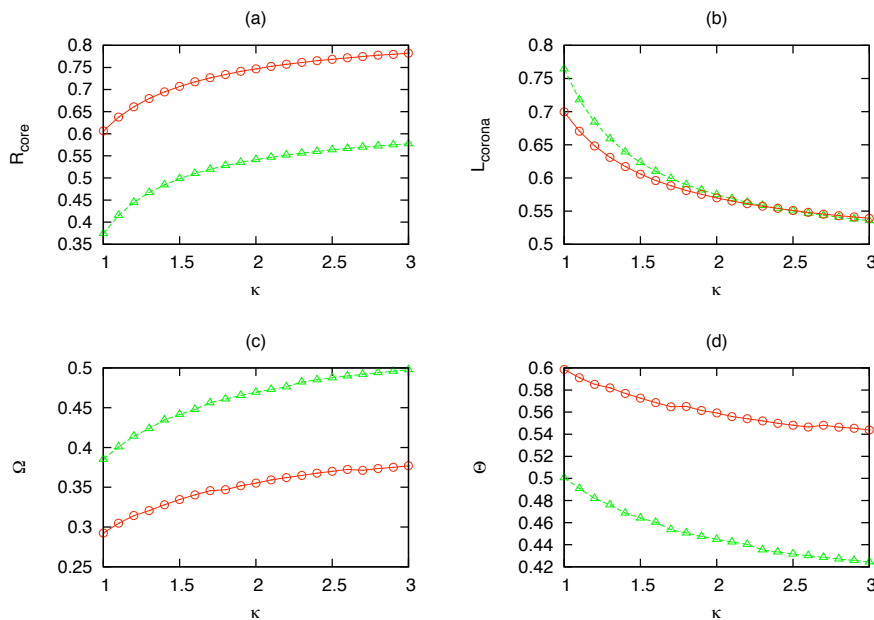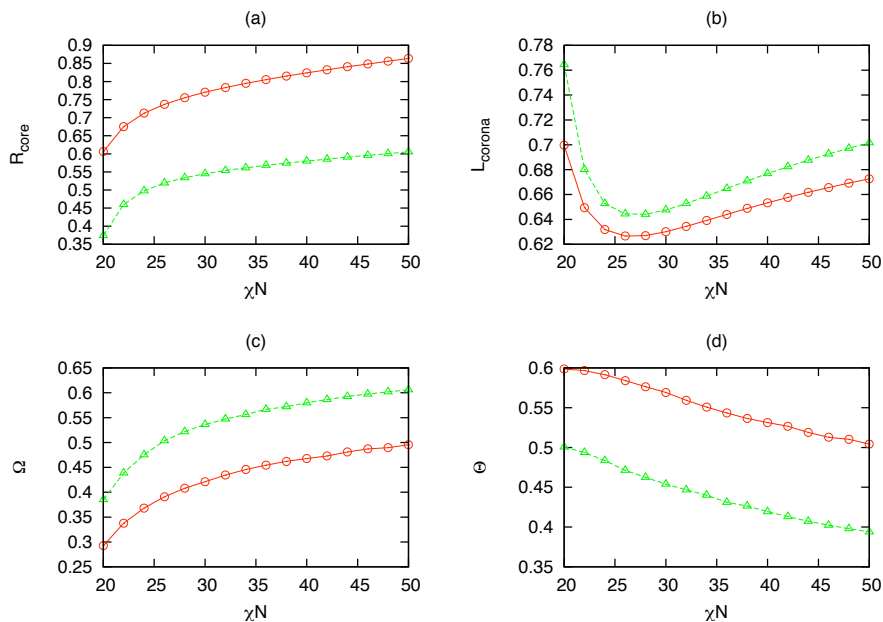

Figure 6.10: Micelle properties as a function of χN for blends with $\kappa = 1.0$ and $f_A = 0.70$. The core radius (a), the corona thickness (b), the excess copolymers (c) and the penetrating homopolymers (d) are plotted. Notation as in Fig. 6.9.

to be stretched in order to reduce the surface per copolymer, therefore the corona thickness starts to increase. This is similar to the case of diblock melts, where the period of the order structure increases as χN increase.

Changes of the micelle morphology in dilute poly(styrene-butadiene)/polystyrene solutions were observed experimentally by Kinning *et al.* [80]. They have examined the case of varying the homopolymer length, and their results are in agreement with the trend shown in Fig. 6.9.

6.3 Summary

In this chapter, we have investigated the shape transition of an isolated micelle formed in the AB/A blends. Self-consistent field theory has been employed to compute the critical micelle concentration for three different morphologies: lamellar, cylindrical and spherical. By comparing the cmc for different shapes, the preferred micelle geometry is determined. Several factors can influence the micelle morphology, and we have explored the diblock asymmetry, the homopolymer/copolymer length ratio and the monomer-monomer interaction. It is found the micelle undergoes a sequence of shape transitions, lamellar $\rightarrow$ cylindrical $\rightarrow$ spherical, when the A-block of the copolymer becomes longer. For asymmetric copolymers with a large A-block, the transition from spherical to cylindrical micelle is expected when the homopolymer length is increased. A similar trend appears when the repulsive interaction between different monomers become stronger. The mechanism of the shape transition can be explained by examining the chain deformation inside the micelle. Valuable information can be obtained from the theory, such as the geometrical dimensions of the micelle, and the distribution of the polymers. These properties are closely related to the controlling parameters. By varying these parameters, micelle with required shape

and size may be obtained for potential applications. Since it is inconceivable and expensive for experimentalists to explore the parameter space by trial-and-error, theoretical study is crucially important to understand the underlying cause and provide guidance for the experiments.

It is important to point out the limitation of the present approach. Since we have neglected the translational entropy of the micelles, the critical micelle concentrations calculated are only valid when the copolymer concentration is small. Also, for lamellar and cylindrical micelles, we only considered the ideal case, while in reality, infinite long cylinders and infinite broad bilayers can not be formed. The ends of the cylinders or the edges of the lamellae will have a contribution to the free energy, so the points of shape transition needed be shifted accordingly. Nevertheless, by comparing the minimum copolymer concentration required for micellization in three geometries under ideal conditions, we have obtained the trends we expect to observe in dilute systems of diblock copolymer with homopolymers. Due to the computational complexity, we only considered the three simplest geometries. Irregular micelle shape may occur under certain conditions, such as under confinement, which is the subject of next chapter.

Chapter 7

Micelles in Thin Film

Polymer thin films are widely used in technology and industry. Applications of polymer thin films include protective surface coatings, birefringent elements in optical devices, and printing circuits in flexible solar cells. Films made by blending different homopolymers/copolymers provide an economical route to obtain new product with enhanced properties. In general, the usage of polymer films requires the surface properties to be homogeneous, but polymer blends tend to phase separate. Copolymers can be used as compatibilizers to induce miscibility in polymer mixtures, but they tends to form aggregates when the concentration exceeds the critical micelle concentration (cmc).

Polymer thin films can also be viewed as polymer blends under planar confinement. For copolymer melts, planar confinement can induce novel morphologies which are not available in bulk system [81, 82, 83]. The phase behavior is determined by the relation between the size of confinement and the natural spacing of the structure. When these two sizes are compatible, bulk structures are preserved; otherwise, new morphologies like perforated lamellae can be formed. Similarly, the confinement can also influence the micelle formation in diblock copolymer/homopolymer blends, and the important factor is the ratio between the micelle dimensions and the size of confinement. When the degree of confinement is small, the micelle reacts by slightly shrinking its size. As the confinement becomes compatible to the micelle size, the micelle formation

becomes unfavorable. This results in an increase of the critical micelle concentration [84, 85] or shape change.

In order to better understand the micelle formation in thin film, we study the micelle shape change in diblock copolymer/homopolymer films. As we have discussed in Chapter 6, micelles can have different morphologies in bulk system: bilayers, cylinders and spheres. Only the planar micelles are commensurate with the thin film geometry, while the other two undergo deformation when the degree of confinement increases. For simplicity, we choose to focus on the spherical micelles in this chapter.

Several parameters control the micelle formation. In the bulk system, the micellization depends primarily on the copolymer architecture and monomer-monomer interactions. In the thin film, the confinement introduces the effect of structure frustration and surface interaction. The degree of structure frustration depends on the relationship between the micelle size and film thickness. If the two are incomparable, the aggregate must deviate from its equilibrium shape to relieve the imposed frustration. Even change of micelle morphology can be induced when the confinement is strong. Beside the geometry confinement, the other important factor in thin film is the surface selectivity. The interaction between monomers and hard surfaces can be neutral or preferential. The selective surface interactions also can cause deviation from the structures observed in the bulk.

In this chapter, we use self-consistent field theory to study the shape of a single micelle formed in the diblock copolymer/homopolymer (AB/A) blends. In Section 7.1, we incorporate the hard-surface effect in the SCFT framework. The deformation of a spherical micelle is discussed in Section 7.2, and the effect of various parameters are elucidated.

7.1 Hard-surface effect

To model the spherical micelles under planar confinement, we adapt a cylindrical coordinate system $(x = r, z)$ which has rotational symmetry with respect to z-axis. The z-axis is perpendicular to the film surfaces, which are located at $z = 0$ and $z = D$. Fig. 7.1 shows a schematic setup of the coordinate system.
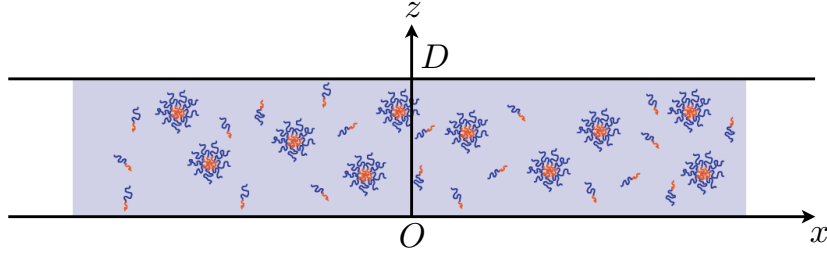

Figure 7.1: Coordinate system for modeling the micelle formation in AB/A films.

In previous chapters, the incompressibility condition is enforced in the self-consistent field theory. The total monomer density $\sum \phi_\alpha(\mathbf{r}) = 1$ everywhere. Under planar confinement, the top and bottom surface are impenetrable, which requires the monomer density to vanish at the surface. A common method to solve this problem is to use a profile $\phi_0(\mathbf{r})$ that is 1 everywhere except close to the surface. Close to the surface, the density varies continuously from 0 to 1 over a short distance of τ. The choice of $\phi_0(\mathbf{r})$ in the surface layer is not important, and we use the one proposed by Meng and Wang [86] to enhance numerical stability,

$$\phi_0(\mathbf{r}) = \begin{cases} \left[\dfrac{\exp[4\tau z/(\tau^2 - z^2)] - 1}{\exp[4\tau z/(\tau^2 - z^2)] + 1}\right]^2 & 0 \leq z \leq \tau \\ 1 & \tau \leq z \leq D - \tau \\ \left[\dfrac{\exp[4\tau(D-z)/(\tau^2 - (D-z)^2)] - 1}{\exp[4\tau(D-z)/(\tau^2 - (D-z)^2)] + 1}\right]^2 & D - \tau \leq z \leq D. \end{cases} \tag{7.1}$$

The incompressibility constraint can be rewritten as

$$\sum_\alpha \phi_\alpha(\mathbf{r}) = \phi_0(z). \tag{7.2}$$

The total density profile near the surface is plotted in Fig. 7.2 for $\tau = 0.15R_g$.
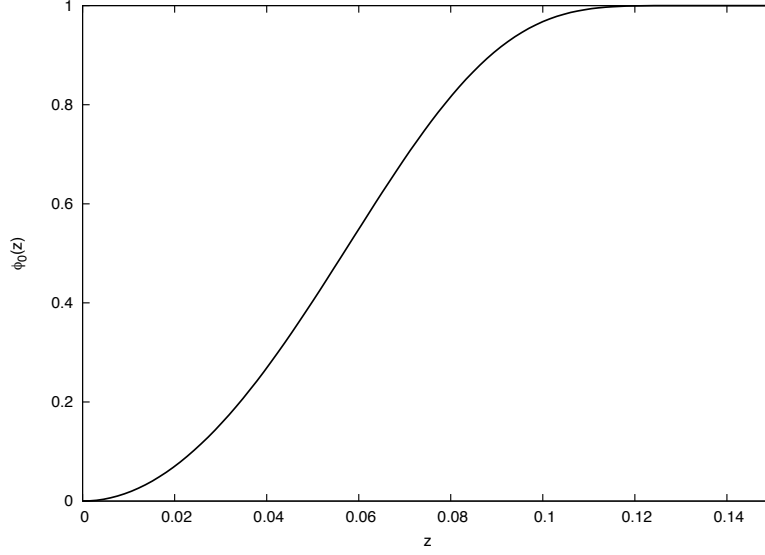
Figure 7.2: Total monomer density near the hard surface for $\tau = 0.15R_g$.

The surface interaction is represented by a surface field $H(\mathbf{r})$. For simplicity, a short-range, linear field is used:

$$H(\mathbf{r}) = \begin{cases} \Gamma_l(1 - z/\tau) & 0 \leq z \leq \tau \\ 0 & \tau \leq z \leq D - \tau \\ \Gamma_u[1 - (D - z)/\tau] & D - \tau \leq z \leq D \end{cases} \tag{7.3}$$

The constant Γ_l and Γ_u are used to characterize the surface selectivity for the lower and upper surfaces, respectively. In our notation, a positive value of Γ corresponds to the attractive interaction to A-monomer (or a repulsive interaction to B-monomer).

The surface interaction adds another term in the field equations

$$\omega_A(\mathbf{r}) = \chi N \phi_B(\mathbf{r}) - H(\mathbf{r}) + \eta(\mathbf{r}), \tag{7.4}$$

$$\omega_B(\mathbf{r}) = \chi N \phi_A(\mathbf{r}) + H(\mathbf{r}) + \eta(\mathbf{r}). \tag{7.5}$$

The surface contribution to the total free energy is

$$f_{\mathbf{s}} = -\frac{1}{V}\left\{\int_{0\leq z\leq\tau}\mathrm{d}V H(\mathbf{r})[\phi_A(\mathbf{r})-\phi_B(\mathbf{r})] + \int_{D-\tau\leq z\leq D}\mathrm{d}V H(\mathbf{r})[\phi_A(\mathbf{r})-\phi_B(\mathbf{r})]\right\}$$
(7.6)

The self-consistent equations are solved in the real-space using the ADI method [41]. In this chapter, we focus on the case that the homopolymer and copolymer have the same length, so $\kappa = 1$. The blends have intermediate segregation at $\chi N = 20$.

7.2 Results and discussion

We present the results using two-dimension color plots. Fig. 7.3 shows the monomer densities for a single spherical micelle under confinement. The three plots correspond to the (a) B-block of the copolymer; (b) A-block of the copolymer and (c) A-homopolymer. The light color corresponds to larger value of concentration.

The parameters are $f_A = 0.7$, $\kappa = 1$, $\phi_c = 0.1$ and $\chi N = 20$. The separation between the surfaces are $4\sqrt{N}b$ which is larger than the natural size of the micelle. The surface selectivity is neutral so $\Lambda_l = \Lambda_u = 0$. The micelle consists of a core of the B-blocks of the copolymer, surrounded by a corona of A-blocks. There are also small amounts of A-homopolymers swelling the corona, as shown in the $\phi_{hA}(\mathbf{r})$ profile.

Far away from the micelle, the concentrations are expected to reach the bulk values. However, due to the presence of the two hard surfaces, the density profile is not homogeneous along the z direction (see Fig. 7.4). Because of the total density is less than 1 near the surface, this effectively reduces the A-B repulsive interaction in the surface layer [45]. Therefore it is energetically favorable for copolymers to accumulate close to the surfaces. Furthermore, the B-block has a stronger tendency to swell the surface layer than the A-block. This is because the surfaces are neutral, so there are no differences between a diblock copolymer chain and a homopolymer chain
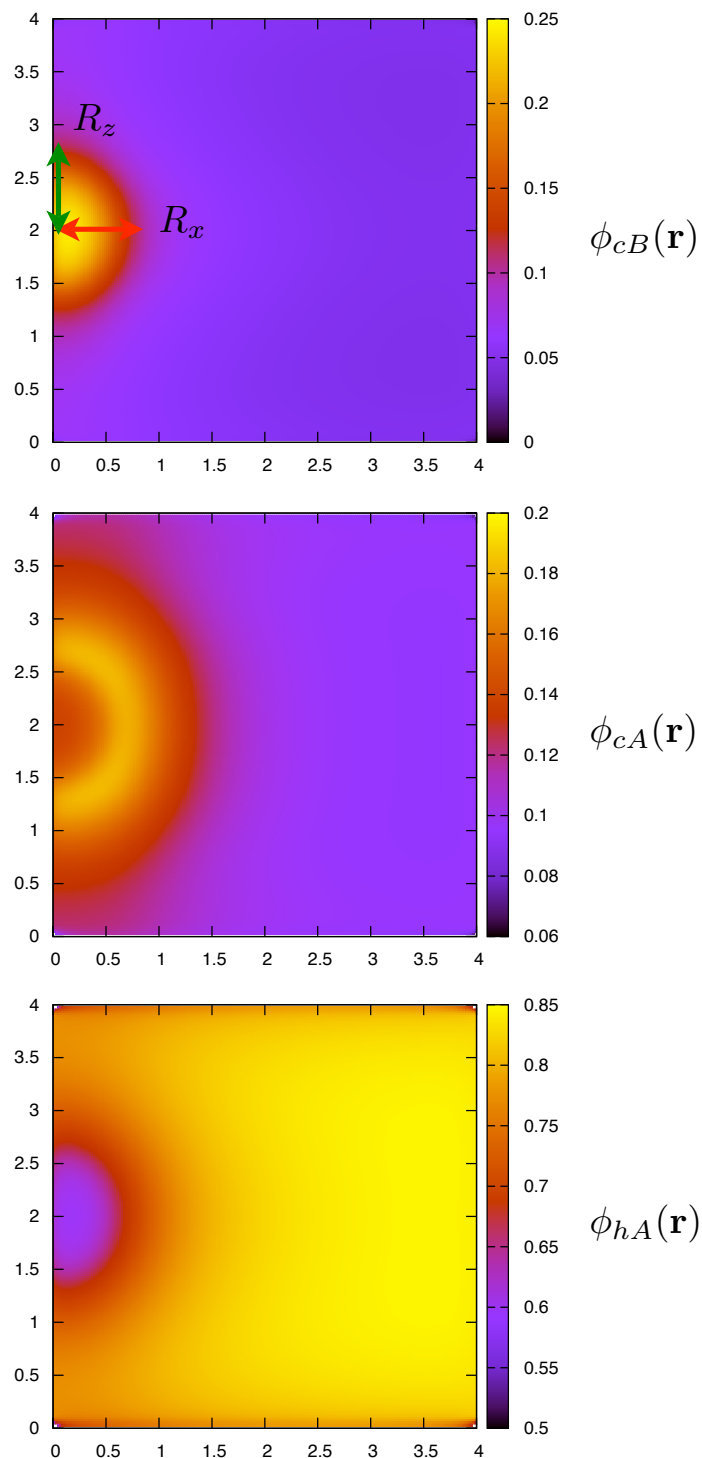
Figure 7.3: Monomer density profiles for a spherical micelle formed in the AB/A films. The length unit is $\sqrt{N}b$.

for the surface. From the entropy point of view, both ends of the copolymer have the equal probability to be found near the surface. This corresponds to an enrichment of the minority-component of the copolymer (B-block for $f_A = 0.7$). This effect is demonstrated in Fig. 7.4.
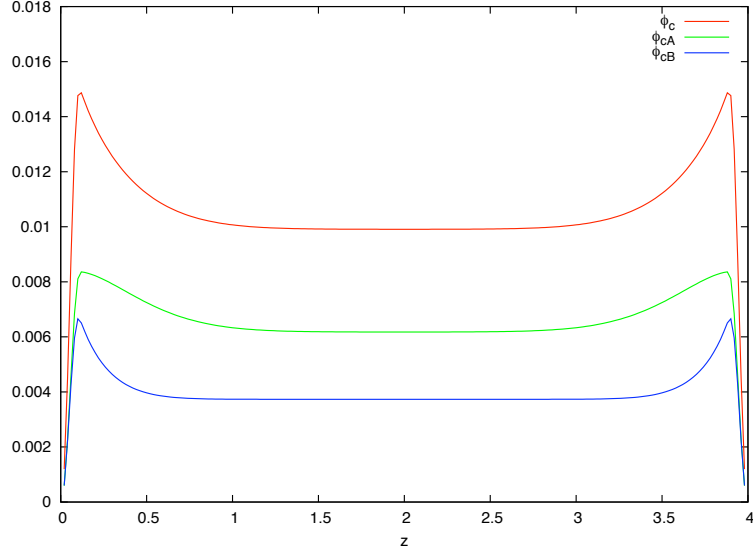
Figure 7.4: Copolymer density away from the micelle ($x = 4\sqrt{N}b$). The parameters are the same as Fig. 7.3.

In order to quantify the confinement effect, we calculate the radii in both x- and z-direction, defined as

$$R_x^2 = \frac{\int dV[\phi_c(\mathbf{r}) - \phi_c'(z)](x - x_0)^2}{\int dV[\phi_c(\mathbf{r}) - \phi_c'(z)]}, \tag{7.7}$$

$$R_z^2 = \frac{\int dV[\phi_c(\mathbf{r}) - \phi_c'(z)](z - z_0)^2}{\int dV[\phi_c(\mathbf{r}) - \phi_c'(z)]}, \tag{7.8}$$

where $(x_0, z_0) = (0, D/2)$ is the micelle center position. $\phi_c'(z)$ is the copolymer density away from the micelles and only depends on z. The removal of $\phi_c'(z)$ is necessary in order to isolate the micelle from the background.

7.2.1 Geometry frustration

In order to understand the effect of confinement, we perform the calculation for films with thickness range from $8.0\sqrt{N}b$ to $1.0\sqrt{N}b$. Both surfaces are neutral ($\Lambda_l = \Lambda_u = 0$). The x- and z-radius are calculated from the density profile. The results are shown in Fig. 7.5(a). To characterize the shape deformation, we define the ellipticity ε as the ratio between the two radii,

$$\varepsilon = \frac{R_x}{R_z}. \tag{7.9}$$

The value of ε is shown in Fig. 7.5(b).

The shape change of an isolated spherical micelle shows two different stages. Initially, when D is large, there are only slight change for both radii as the influence of the surfaces are negligible. When the film thickness becomes comparable to the size of the micelle, the copolymers that forms the micelle start to overlap with the surface layer. This will cause the micelle to contract in the z-direction, as the R_z starts to reduce at about $D = 3.0\sqrt{N}b$. Interestingly, the radius in x-direction is also reduced, which corresponds to the diminishing of the micelle volume. The simulation demonstrates that the confinement reduces the number of copolymer chains per micelle, and it becomes favorable for copolymer to stay as isolated chains instead of forming the micelles. When the film thickness is reduced further, the surface layer starts touch the core of the micelle. Spherical micelles become unstable and undergo a morphology transition to cylindrical micelles with their axes normal to the surface. For the parameters used here, this occurs at about $D = 1.6\sqrt{N}b$. In the inset of Fig. 7.5, the $\phi_{cB}(\mathbf{r})$ profiles are shown for $D = 2.0\sqrt{N}b$ (top) and $D = 1.4\sqrt{N}b$ (bottom).
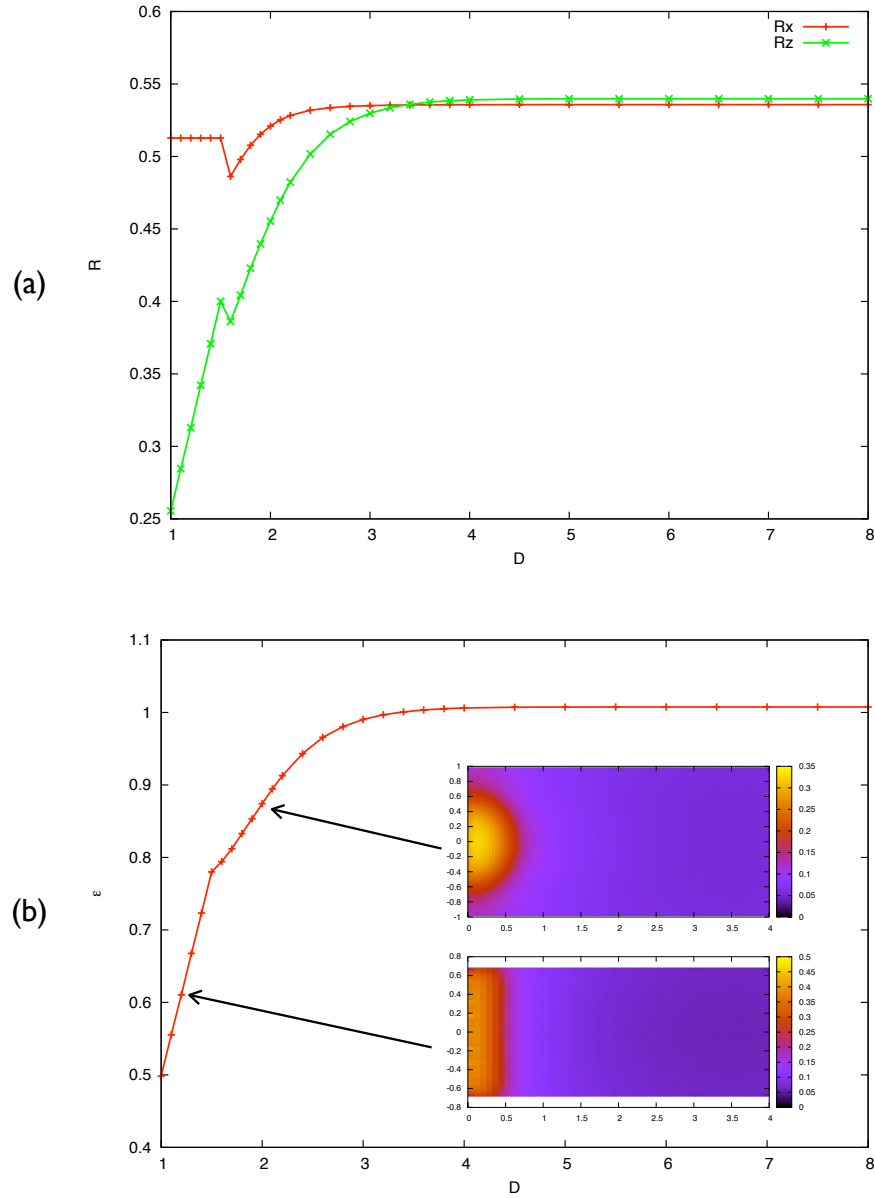
Figure 7.5: (a) x- and z-radius for a spherical micelle under confinement. (b) ellipticity. The insets in (b) are the $\phi_{cB}(\mathbf{r})$ profile for $D = 2.0\sqrt{N}b$ (top) and $D = 1.4\sqrt{N}b$ (bottom).

7.2.2 Surface selectivity

The shape of a micelle can also be tuned by the surface interaction. In Fig. 7.6, the ratio of R_x/R_z is plotted as a function of surface selectivity.
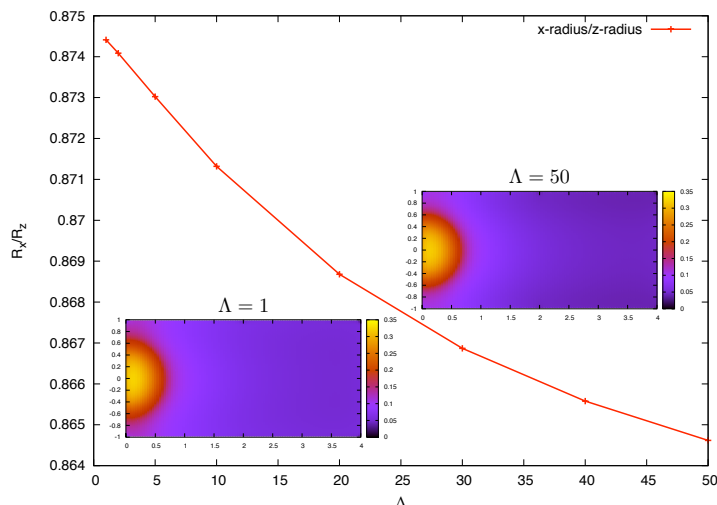
Figure 7.6: The ratio between x- and z-radius as a function of surface selectivity for the symmetric case. The two insets show the density profile of ϕ_{cB} for two different value of selectivity: $\Lambda = 1$ (left) and $\Lambda = 50$ (right).

Here we consider the symmetric case where the two surfaces have the same selectivity $\Lambda_l = \Lambda_u = \Lambda$. Since the positive value of Λ corresponds to attractive interaction to the A-monomer, so equivalently an repulsive interaction to the B-monomer. The ratio reduces as the repulsive interaction to B-monomer becomes stronger. In the inset of Fig. 7.6, the $\phi_{cB}(\mathbf{r})$ profiles are shown for $\Lambda = 1$ (left) and $\Lambda = 50$ (right).

For the asymmetric case, we calculate the density profile for two sets of parameters. Fig. 7.7 shows the results. The lower surface selectivity $\Lambda_l = 0$, while the upper surface $\Lambda_u = 1$ for Fig. 7.7(a) and $\Lambda_u = 50$ for Fig. 7.7(b). It is difficult to tell the difference, so in Fig. 7.7(c) the deference between (b) and (c) are plotted. The

stronger repulsive interaction of the upper surface produce an depletion zone near the top of the film.
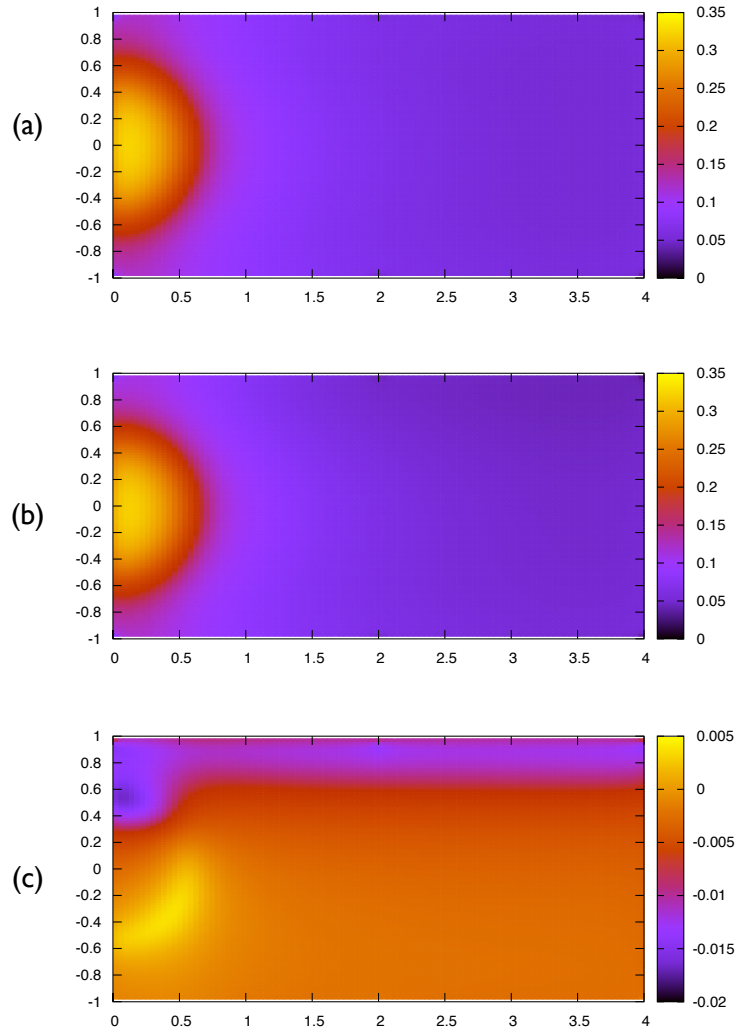
Figure 7.7: The density profile of ϕ_{cB} when the two surface have different selectivity. (a) $\Lambda_l = 0$, $\Lambda_u = 1$; (b) $\Lambda_l = 0$, $\Lambda_u = 50$; (c) the difference.

7.3 Summary

In this chapter, we consider the micelle formation under planar confinement. The density profiles of a spherical micelle formed in AB/A blends are computed using

self-consistent field theory. The shape of the micelle becomes anisotropic under planar confinement. Deviation from the spherical geometry is noticeable when the film thickness is comparable to the size of the micelle. Morphology transition can also happen when the confinement is strong. We consider the effect of film thickness and surface selectivity. The results reveal that the spherical symmetry is destroyed by the film geometry whereas the top-down symmetry is broken by the surface selectivity.

Chapter 8

Summary and Perspective

In this chapter, we summarize key results for various topics examined in this thesis and discuss some questions and problems which may be worth investigating in the future.

8.1 Key results

In this thesis, we have used self-consistent field theory to study the phase behavior of diblock copolymer/homopolymer blends. We approached this system from two different angles. Chapter 4 and 5 focused on the equilibrium structures of AB/C blends. The key question addressed here is the morphology transition induced by adding homopolymers to diblock copolymers. In general, homopolymers can either separate from diblock copolymers, or accumulate to like blocks. In the former case, macrophase separation occurs, while in the later situation, blends may undergo order-order transition. Depending on the interaction between homopolymers and diblock copolymers, two model systems have been studied in detail. The first one involves homopolymers that have a repulsive interaction to diblock copolymers. We found an interesting feature in the phase diagram that there exists a bump of the phase boundary line when A is the majority-component. In the second case, we consider homopolymers that have an attractive interaction to one of the blocks of diblock copolymers. A closed-loop of microphase separation region forms when the interac-

tion becomes strong. For both cases, we have considered the effect of homopolymer concentration, homopolymer chain length, and monomer-monomer interactions.

The second angle is to study the micelle formation in AB/A blends, and chapter 6 and 7 are devoted to this subject. When small amounts of diblock copolymers are blended with homopolymers, the copolymers can segregate and self-assemble into lamellar, cylindrical and spherical micelles. The critical micelle concentration for each geometry is determined using self-consistent field theory. In general, micelles undergo transition lamellar $\rightarrow$ cylindrical $\rightarrow$ spherical when the A-block becomes longer. Various factors can influence the micelle morphology, and we have considered the effect of varying copolymer block asymmetry, homopolymer molecular weight and monomer-monomer interactions. When blends are confined between two flat surfaces, the shape of the micelle may differ from that of the bulk micelle. We have studied the shape variation of an isolated spherical micelle under planar confinement and the dependence on the film thickness and surface selectivity. The results reveal that the spherical symmetry is destroyed by the film geometry whereas the top-down symmetry is broken by the surface selectivity.

8.2 Perspective

Diblock copolymer/homopolymer blends

Compared to neat AB diblock copolymers, the addition of C homopolymers increases the controlling parameters from $(f_A, \chi N)$ to $(f_A, \kappa, \phi_H, \chi_{AB}N, \chi_{BC}N, \chi_{AC}N)$. The increase of freedom can be seen as a blessing in the sense that now we have more ways to control and manipulate material properties. It can also be viewed as a curse because interesting phenomena may be determined by several parameters and it is difficult to isolate the key factor. Since it is inconceivable and expensive for

experimentalists to explore the parameter space by trial-and-error, theories and simulations are important to study the phase diagram systematically and identify the predominant parameters for polymer blends.

In this thesis, we have used the Flory-Huggins type of interaction. The microscopic feature of the system is incorporated in the three pairs of interaction parameters (χ_{AB}, χ_{BC}, χ_{AC}). We assume these Flory-Huggins parameters can vary independently. In reality, the situation is not as simple. Once the chemical components are chosen, these interaction parameters are correlated and can be viewed as functions of temperature. This effectively reduces the parameter space to four-dimension. Various factors can contribute to the relation between the pair interactions and their dependence on temperature. In order to make quantitative comparison between experiments and theory prediction, we need to establish a microscopic theory for the χ-parameters. This, even just for binary blends, still remains a formidable task [87], and requires further investigation.

Although we only consider the classical morphologies in this thesis, the phase diagram of AB/C blend can be much richer than the AB melts due to the emergence of the complex structures. For the special case of AB/A blends, a bewildering variety of morphologies are predicted to be stable [26, 27, 45, 88], but the parameters have to be controlled carefully in order to observe these structures in experiments. Replacing the A-homopolymer with another chemically distinct C-homopolymer allows more freedom to navigate the parameter space. Theoretic study and simulations can help to identify the region in phase diagram where the complex morphologies exist.

AB/C blends with attractive interaction

Some applications of polymer blends require the material properties to be homogeneous. But it is difficult to generate blends in disordered phase because the long-chain polymers tend to phase-separate. The use of C-homopolymer with attractive interaction provides one way to solve this problem. Interesting ordered structures can also be induced by the attractive interactions [89]. The closed-loop phase diagram obtained in this thesis can be seen as a starting point to understand AB/C blends with attractive interactions.

The study of AB/C blends shows a first-order phase transition from BCC phase to the disordered phase along the closed-loop phase boundary except at two critical points. At these two points, the blends undergo a continuous phase transition from disordered phase to lamellar phase according to the mean-field theory. It is well-known that fluctuations become important near critical points and may affect the phase behavior qualitatively [64, 65]. So it would be useful to conduct the stability analysis near the order-disorder transition.

In experiments, the hydrogen-bonding provides a promising candidate to realize the attractive interaction. Recently, several groups have studied the polymer blends involving hydrogen-bonding [28, 66, 90, 91, 92, 93, 94, 95, 96, 97, 98]. Comparison between the experiments and simulations can be used to test several assumptions in the theory. One central question is the validity of use of a negative Flory-Huggins parameter to model the hydrogen bonding. Further research would be required to construct a microscopic model for the attractive interaction.

Bulk micelles

We consider an isolated micelle in our calculation of critical micelle concentration, so the results are only valid when the copolymer concentration is small. When the

micelle concentration become large, the model needs to incorporate the translational entropy of the micelles. The interactions between micelles also become important at high micelle concentration. Essentially this is a many-body problem and may be difficult to study. As a first attempt, the interaction between two micelles may be easier to tackle [99].

For the lamellar and cylindrical micelles, we only considered the ideal case. While in reality, bilayers always have an edge and cylindrical micelles terminate with two endcaps. The ends of the cylinders and the edges of the lamellae will have contributions to the free energy, so they should also be taken into consideration. Once we consider the edge effect, the lamellar and the cylindrical micelles become finite, and the distribution of micelles with different sizes would require further study.

Another interesting phenomenon is the surface micelle [74, 100]. This can be viewed as an intermediate case between the bulk micelles and micelles under planar confinement. Under equilibrium conditions, block copolymers in general will adsorb to the surface to form a laterally homogeneous layer. However, for very asymmetric diblock copolymers, formation of laterally heterogeneous surface micelles is possible. It will be valuable to systematically analyze the surface micelle morphologies and their dependence on the polymer conformation.

Micelles under confinement

The study of the micelle formation between two planar surfaces brings together two important concepts in physics: the self-assembly and the geometrical confinement. Effect of confinement on ordered structures have been thoroughly studied [101, 102], but the effect on micelle formation is not fully understood. One issue is the effect of

confinement on critical micelle concentration. Similar to the study for bulk micelles, a comprehensive study on the cmc for confined system will be valuable.

The diblock micelles are significantly more stable than the ones made by surfactants of low-molecular weight. This offers opportunities to utilize spherical micelles for drug delivery. Under real biological situation, the micelles would be required to pass through various confined surroundings, such as the capillary vessels. We only consider the planar confinement in this thesis. Further examination on the cylindrical confinement would be interesting and provide insights on how micelles behave in physiological environments.

Bibliography

[1] I. Hamley, *The Physics of Block Copolymers* (Oxford University Press, Oxford, 1998).

[2] F. K. Bates and G. H. Fredrickson, Physics Today **52**, 33 (1999).

[3] D. A. Hajduk *et al.*, Macromolecules **27**, 4063 (1994).

[4] M. F. Schulz, F. S. Bates, K. Almdal, and K. Mortensen, Phys. Rev. Lett. **73**, 86 (1994).

[5] I. W. Hamley *et al.*, Macromolecules **26**, 5959 (1993).

[6] C. A. Tyler and D. C. Morse, Phys. Rev. Lett. **94**, 208302 (2005).

[7] M. Takenaka *et al.*, Macromolecules **40**, 4399 (2007).

[8] M. I. Kim *et al.*, Macromolecules **41**, 7667 (2008).

[9] M. Matsen, J. Phys.: Condens. Matter **14**, R21 (2002).

[10] S. Edwards, Proc. Phys. Soc. **85**, 613 (1965).

[11] E. Helfand, J. Chem. Phys. **62**, 999 (1975).

[12] E. Helfand, Macromolecules **8**, 552 (1975).

[13] K. M. Hong and J. Noolandi, Macromolecules **14**, 727 (1981).

[14] K. Shull, Macromolecules **25**, 2122 (1992).

[15] J. D. Vavasour and M. D. Whitmore, Macromolecules **25**, 5477 (1992).

[16] M. Banaszak and M. D. Whitmore, Macromolecules **25**, 3406 (1992).

[17] L. Leibler, Macromolecules **13**, 1602 (1980).

[18] A. N. Semenov, Sov. Phys. -JETP **61**, 733 (1985).

[19] M. Matsen and M. Schick, Phys. Rev. Lett. **72**, 2660 (1994).

[20] F. Drolet and G. Fredrickson, Phys. Rev. Lett. **83**, 4317 (1999).

[21] G. Tzeremes, K. Rasmussen, T. Lookman, and A. Saxena, Phys. Rev. E. **65**, 041806 (2002).

[22] G. H. Fredrickson, *The Equilibrium Theory of Inhomogeneous Polymers* (Clarendon Press, Oxford, 2006).

[23] F. Schmid, J. Phys.: Condens. Matter **10**, 8105 (1998).

[24] G. H. Fredrickson, V. Ganesan, and F. Drolet, Macromolecules **35**, 16 (2002).

[25] A.-C. Shi, in *Developments in Block Copolymer Science and Technology*, edited by I. Hamley (John Wiley & Sons, New York, 2004), Chap. 8.

[26] M. Matsen, Phys. Rev. Lett. **74**, 4225 (1995).

[27] F. Martinez-Veracoechea and F. Escobedo, Macromolecules **42**, 1775 (2009).

[28] W.-C. Chen, S.-W. Kuo, U.-S. Jeng, and F.-C. Chang, Macromolecules **41**, 1401 (2008).

[29] M. Doi and S. Edwards, *The Theory of Polymer Dynamics* (Clarendon Press, Oxford, 1994).

[30] D. Chandler, *Introduction to Modern Statistical Mechanics* (Oxford University Press, Oxford, 1987).

[31] H. Kleinert, *Path Integrals in Quantum Mechanics, Statistics, Polymer Physics and Finance Markets*, 4th ed. (World Scientific Publishing, Singapore, 2006).

[32] N. van Kampen, *Stochastic Processes in Physics and Chemistry*, 3rd ed. (Elsevier, Amsterdam, 2007).

[33] R. Feynman and A. Hibbs, *Quantum Mechanics and Path Integrals* (McGraw-Hill, New York, 1965).

[34] A. Zee, *Quantum Field Theory in a Nutshell* (Princeton University Press, Princeton, 2003).

[35] M. Doi, *Introduction to Polymer Physics* (Clarendon Press, Oxford, 1996).

[36] *International Tables of X-Ray Crystallography*, edited by N. Henry and K. Lonsdale (Kynoch Press, Birmingham, UK, 1965).

[37] Z. Guo *et al.*, Phys. Rev. Lett. **101**, 028301 (2008).

[38] J.-L. Barrat, G. H. Fredrickson, and S. W. Sides, J. Phys. Chem. B **109**, 6694 (2005).

[39] E. Helfand and Z. R. Wasserman, Macromolecules **9**, 879 (1976).

[40] Y. Bohbot-Raviv and Z.-G. Wang, Phys. Rev. Lett. **85**, 3428 (2000).

[41] W. H. Press, S. A. Teukolsky, W. T. Vetterling, and B. P. Flannery, *Numerical Recipes*, 3rd ed. (Cambridge University Press, New York, 2007).

[42] *Polymer Blends*, edited by D. Paul and S. Newman (Academic Press, New York, 1978).

[43] L. Utracki, *Polymer Alloys and Blends: Thermodynamics and Rheology* (Hanser Pub, New York, 1989).

[44] A. Semenov, Macromolecules **26**, 2273 (1993).

[45] M. Matsen, Macromolecules **28**, 5765 (1995).

[46] P. Janert and M. Schick, Macromolecules **31**, 1109 (1998).

[47] T. Hashimoto, H. Tanaka, and H. Hasegawa, Macromolecules **23**, 4378 (1990).

[48] H. Tanaka, H. Hasegawa, and T. Hashimoto, Macromolecules **24**, 240 (1991).

[49] K. Winey, E. Thomas, and L. Fetters, Macromolecules **24**, 6182 (1991).

[50] M. Jiang and H. Xie, Prog. Polym. Sci. **16**, 977 (1991).

[51] M. Jiang, T. Huang, and J. Xie, Macromol. Chem. Phys. **196**, 787 (1995).

[52] B. Lowenhaupt, A. Steurer, G. Hellmann, and Y. Gallot, Macromolecules **27**, 908 (1994).

[53] J. Zhao, E. Pearce, and T. Kwei, Macromolecules **30**, 7119 (1997).

[54] Y. Han, E. Pearce, and T. Kwei, Macromolecules **33**, 1321 (2000).

[55] L. Zeman and D. Patterson, Macromolecules **5**, 513 (1972).

[56] W. Jo, Y. Kwon, and I. Kwon, Macromolecules **24**, 4708 (1991).

[57] C. Manestrel *et al.*, Macromolecules **25**, 1701 (1992).

[58] S.-W. Kuo, C.-L. Lin, and F.-C. Chang, Macromolecules **35**, 278 (2002).

[59] P.-G. de Gennes, *Scaling Concepts in Polymer Physics* (Cornell University Press, Ithaca, 1979).

[60] K. Mori, H. Tanaka, and T. Hashimoto, Macromolecules **20**, 381 (1987).

[61] Y. Ijichi and T. Hashimoto, Polym. Commun. **29**, 135 (1988).

[62] H. Tanaka and T. Hashimoto, Polym. Commun. **29**, 212 (1988).

[63] R. Wang *et al.*, Macromolecules **42**, 2275 (2009).

[64] G. H. Fredrickson and E. Helfand, J. Chem. Phys. **87**, 697 (1987).

[65] L. Kielhorn and M. Muthukumar, J. Chem. Phys. **107**, 5588 (1997).

[66] V. Tirumala *et al.*, Macromolecules **41**, 7978 (2008).

[67] S. A. Safran, *Statistical Thermodynamics of Surfaces, Interfaces, and Membranes* (Addison-Wesley, New York, 1994).

[68] Y. Kim, P. Dalhaimer, D. Christian, and D. Discher, Nanotechnology **16**, S484 (2005).

[69] L. Leibler, Makromol. Chem., Macromol. Symp. **16**, 1 (1988).

[70] K. R. Shull, E. J. Kramer, G. Hadziioannou, and W. Tang, Macromolecules **23**, 4780 (1990).

[71] L. Leibler, H. Orland, and J. C. Wheeler, J. Chem. Phys. **79**, 3550 (1983).

[72] A. M. Mayes and M. O. de la Cruz, Macromolecules **21**, 2543 (1988).

[73] P. Linse, Macromolecules **26**, 4437 (1993).

[74] K. R. Shull, Macromolecules **26**, 2346 (1993).

[75] F. Leermakers, C. Wijmans, and G. Fleer, Macromolecules **28**, 3434 (1995).

[76] D. Duque, J. Chem. Phys. **119**, 5701 (2003).

[77] K. Chang and D. C. Morse, Macromolecules **39**, 7746 (2006).

[78] M. J. Greenall, D. M. A. Buzza, and T. C. B. McLeish, Macromolecules **42**, 5873 (2009).

[79] M. J. Greenall, D. M. A. Buzza, and T. C. B. McLeish, J. Chem. Phys. **131**, 034904 (2009).

[80] D. J. Kinning, K. I. Winey, and E. L. Thomas, Macromolecules **21**, 3502 (1988).

[81] Q. Wang, P. Nealey, and J. de Pablo, Macromolecules **34**, 3458 (2001).

[82] Y. Yin *et al.*, ChemPhysChem **5**, 540 (2004).

[83] P. Chen, H. Liang, and A.-C. Shi, Macromolecules **40**, 7329 (2007).

[84] S. Zhu *et al.*, Nature **400**, 49 (1999).

[85] X. Zhang, G. Chen, and W. Wang, J. Chem. Phys. **127**, 034506 (2007).

[86] D. Meng and Q. Wang, J. Chem. Phys. **126**, 234902 (2007).

[87] K. Foreman and K. Freed, Adv. Chem. Phys. **103**, 335 (1998).

[88] F. J. Martinez-Veracoechea and F. A. Escobedo, Macromolecules **42**, 9058 (2009).

[89] A. Jain and U. Wiesner, Macromolecules **37**, 5665 (2004).

[90] H.-F. Lee *et al.*, Macromolecules **39**, 5458 (2006).

[91] W.-C. Chen *et al.*, Macromolecules **42**, 3580 (2009).

[92] S.-C. Chen *et al.*, Macromolecules **43**, 1083 (2010).

[93] W.-C. Chen, S.-W. Kuo, and F.-C. Chang, Polymer **51**, 4176 (2010).

[94] V. R. Tirumala *et al.*, Adv. Mater. **20**, 16031608 (2008).

[95] K. Dobrosielska, S. Wakao, A. Takano, and Y. Matsushita, Macromolecules **41**, 7695 (2008).

[96] K. Dobrosielska *et al.*, Macromolecules **42**, 7098 (2009).

[97] N. Hameed, J. Liu, and Q. Guo, Macromolecules **41**, 7596 (2008).

[98] N. Hameed, N. V. Salim, and Q. Guo, J. Chem. Phys. **131**, 214905 (2009).

[99] R. B. Thompson and M. W. Matsen, J. Chem. Phys. **112**, 6863 (2000).

[100] A. Cavallo, M. Muller, and K. Binder, Macromolecules **41**, 4937 (2008).

[101] B. Yu *et al.*, Phys. Rev. Lett. **96**, 138306 (2006).

[102] P. Chen, H. Liang, and A.-C. Shi, Macromolecules **41**, 8938 (2008).